LOW-FREQUENCY 1/F NOISE: LOW TEMPERATURE MEASUREMENTS AND EFFECT ON SUPERCONDUCTING QUBIT DEPHASING

BY

TREVIS A. CRANE

B.A., University of Arkansas at Little Rock, 1998
M.S., University of Illinois, 2000

DISSERTATION

Submitted in partial fulfillment of the requirements
for the degree of Doctor of Philosophy in Physics
in the Graduate College of the
University of Illinois at Urbana-Champaign, 2005

Urbana, Illinois

Abstract

Low-frequency noise caused by critical-current fluctuations in Josephson junctions can lead to substantial, measurement-induced dephasing in superconducting qubits. The purpose of this work is to measure this noise as a function of temperature and to simulate its effect on the measurement dynamics associated with superconducting qubits. In Nb trilayer junctions we measure the noise power at 1 Hz down to 10 mK and verify a T^2 dependence for $T > 1$ K, below which we observe a flattening of the noise magnitude versus temperature. In Al trilayer junctions we measure the critical-current noise power at 1 Hz from 10 mK to 1.4 K and find no dependence on temperature over this range. Possible reasons for the deviation from a T^2 dependence are explored, including heating and sample quality. Simulations of the effect of $1/f$ noise are performed to examine the consequence of using different qubit sampling methods on expected dephasing times. Using the two sampling methods, we can probe the spectral nature and possible source of the dominant noise in a qubit.

To the Group, my foundation,
and Corinna, my life.

Acknowledgments

My research would not have possible without the assistance of a number of people. First and foremost is my advisor, the Big D. Dale's support and friendship were absolutely necessary and very much appreciated. Secondly, I need to thank the members of the DVH group, both past and present. Of particular note are William Neils, Tony Bonetti, and Brian Yanoff. And of past DVH group members who have been of particular help after they left Champaign, I must mention Kevin Osborn for supplying samples while at NIST-Boulder.

I would like also to thank Tony Banks for considerable assistance in the fabrication of my samples. John Martinis, John Clarke and their people deserve my thanks for samples in addition to numerous discussions concerning my research.

Further thanks should go to Mark Jackson at Oxford Instruments for the considerable assistance he provided in getting our TLM dilution refrigerator up and running. His help was very useful in learning many of the finer points of running the fridge.

This work was supported by the National Science Foundation under grant number EIA-01-21565 and the Department of Energy, Basic Energy Sciences Division grant number DEFG02-91ER45939.

Table of Contents

List of Figures

1 Introduction

Superconducting Josephson junctions are used in numerous applications and most recently are being used as the fundamental element of superconducting quantum bits (qubits). Knowledge of Josephson junction noise characteristics is essential to their effective use in any application. The purpose of this research is to determine and characterize the low-frequency ($1/f$), critical-current noise present in Josephson junctions as a function of temperature. In addition, we simulated the effect of $1/f$ noise on dephasing of superconducting qubits incorporating Josephson junctions.

Chapter 2 will develop the superconductivity theory necessary to understand Josephson junctions and their behavior when incorporated into qubits. This information can be found in one or both of the standard texts on superconductivity: Tinkham [54] and Waldram [65]. This chapter is intended to familiarize the reader with the standard conventions concerning superconductivity used throughout the rest of this thesis.

Chapter 3 will introduce the physics associated with low-frequency ($1/f$) noise in electronic systems. Some time will be spent examining past theories and how they relate to $1/f$ noise in Josephson junctions. $1/f$ noise is a near-ubiquitous phenomenon in physical systems, and this chapter will develop the motivation behind the research outlined in this dissertation. In addition, a survey of previous work done measuring $1/f$ noise in Josephson junctions will be presented.

In the next chapter we examine the use of Josephson junctions in super-

conducting qubits. The concept of using a two-state system for the purpose of quantum computing will be developed, and some of the dynamics of dissipation in a two-state system [28] will be touched on. There are several considerations when using Josephson junctions to make qubits, but perhaps the most important is that of decoherence in the qubit due to coupling to environmental degrees of freedom. Finally, since the performance of Josephson junctions in qubits prompted the question of $1/f$ noise in Josephson junctions as a possible cause of decoherence, the effect $1/f$ noise in Josephson junctions has on qubits will be explored as well.

Chapter 5 will present the results of numerous simulations performed calculating the effect of measurement-induced dephasing in qubits due to low-frequency noise in Josephson junctions. We will present two distinct qubit sampling strategies that give markedly different results. Further, the different sampling methods can be used as a diagnostic of the dominant noise properties of a superconducting qubit system. Extending the concept of noise-diagnostics, we will investigate the relationship between dephasing and the noise exponent, α, of noise characterized by a $1/f^{\alpha}$ power spectrum.

In Chapter 6 we will begin discussing the particulars of the experimental work done for this project. Starting with sample fabrication, the samples measured for this work range in architecture from the submicron size scale, requiring advanced electron-beam lithographic techniques, to the relatively enormous junctions made with either niobium or aluminum trilayer and patterned with standard photolithographic procedures.

Chapter 7 addresses our experimental setup. We detail the dilution refrigerator used, as well as lead filtering, and sample box construction. Next the measurement circuit is described. We will discuss two different ways of measuring the noise of a Josephson junction with a SQUID. Both techniques

possess different characteristics that need to be examined. Finally, we account for noise sources present in the experimental setup that will lead to noise other than the desired signal and examine whether or not these other noise sources will be negligible or of serious concern.

At long last we arrive at Chapter 8 in which the results of our measurements will be discussed. We performed numerous measurements of several Josephson junctions of different sizes and architecture. The results will be analyzed, and possible explanations will be presented that address the outcome of the measurements. Further attention will be devoted to the discussion of heating as a source of the measured noise.

In the Conclusions, the measured noise levels will be compared with the those predicted by the empirical formula developed by Van Harlingen *et al.* [57]. Questions remaining concerning the data will be explored, and future directions for the work will be suggested.

2 Superconductivity

This chapter contains a synopsis of the areas of superconductivity that are relevant to this research. In particular, the tools necessary for the explanation of Josephson junctions and their behavior in loops and qubits are developed. Beginning with the phenomenological approach to superconductivity and moving on to the microscopic theory of superconductivity, the physics behind the Josephson effect is explored. This chapter concludes by examining the properties exhibited by Josephson junctions when incorporated in multiply-connected geometries.

In 1956 Cooper [6] presented the idea that even a weak attraction between electrons would lead to the pairing of electrons. This implies that given any attraction, the electrons will condense until some equilibrium is reached. The theory [2] extending this to the many-electron system was worked out by Bardeen, Cooper, and Schrieffer (BCS). The BCS theory was a watershed event in the field of superconductivity and physics more generally, finally codifying in brilliant simplicity the nature of the superconducting ground state. With this in hand they proceeded to use their new theory to accurately calculate numerous properties of superconductors, illustrating its value. The BCS theory is remarkable in its insight and understanding of superconductivity; however, it can also be cumbersome to use and is not well suited to calculating device properties.

Of particular note, however, is the presence of an energy gap in the density of states that is explained by BCS. At energies below the superconducting

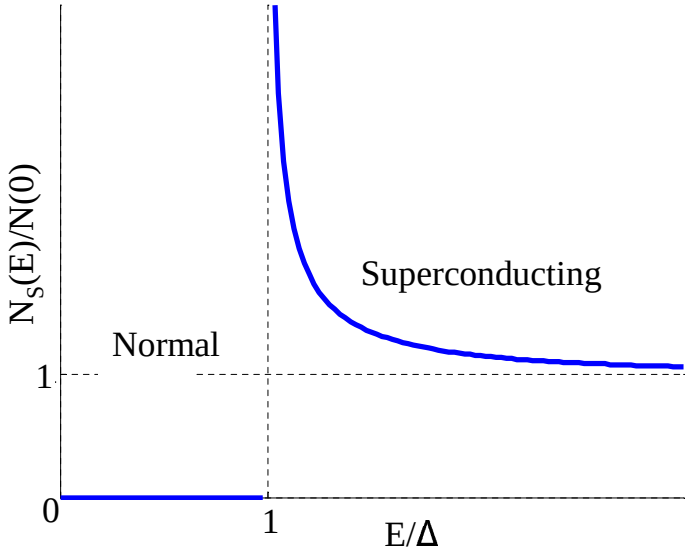

Figure 2.1 *Density of states in a superconductor compared with that of a normal metal, with reference to the Fermi energy. All the states below the gap energy in the normal metal are forced above the gap energy in the superconductor. The horizontal dashed line represents the density of states for a normal metal.*

gap energy Δ, no stationary states for electrons exist and are pushed up to energies above the gap (Fig. 2.1).

This leads to remarkable tunneling properties [50]. For example, when tunneling from a superconductor into a normal metal, the current-voltage characteristic substantially deviates from the expected Ohmic relationship expected in normal-normal interfaces. This deviation is a direct result of the functional form of the density of states in a superconductor. The expression for current flowing through a superconductor-normal interface is

$$\begin{aligned} I_{ns} &= A|T|^2 N_1(0) \int_{-\infty}^{\infty} N_{2s}(E)[f(E) - f(E+eV)]dE \\ &= \frac{G_{nn}}{e} \int_{-\infty}^{\infty} \frac{N_{2s}(E)}{N_2(0)}[f(E) - f(E+eV)]dE \end{aligned} \tag{2.1}$$

where $N_i(0, E)$ is the density of states for a normal metal or superconductor, respectively, A is the area, and $G_{nn} \equiv A|T|^2 N_1(0) N_2(0) e$ is the normal-

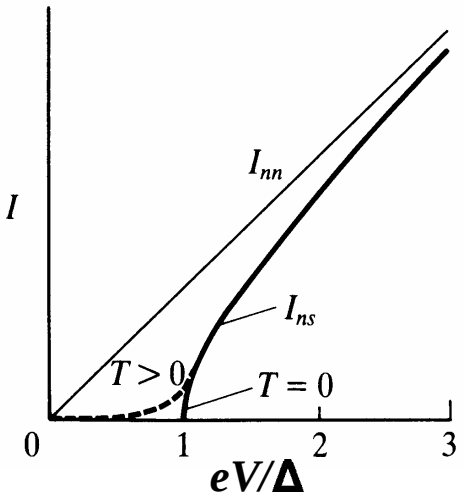

Figure 2.2 *Current voltage characteristic of a normal metal-superconductor tunnel junction[54]. Solid curves refer to $T = 0$, while the dashed curve is for $T > 0$.*

state conductance of a normal-metal to normal-metal interface. An exact evaluation to Eq. (2.1) must be done numerically; however, it is simple to sketch the solution qualitatively, since for bias voltages below $e|V| \geq \Delta$ there will be no tunneling current because the chemical potential difference must provide enough energy to create excitations in the superconductor. This behavior is illustrated in Fig. 2.2. For applied voltages greater than the gap voltage, the excitation energy is sufficient to break Cooper pairs, resulting in a resistance comparable to R_n. However, for voltages below the gap voltage, only thermally excited quasiparticles can tunnel, giving a high resistance. This becomes important later on when discussing the dynamics of Josephson junctions.

2.1 Ginzburg-Landau

For our purposes, the full microscopic treatment of BCS is not necessary. While BCS theory works out in detail the microscopic picture of supercon-

ductivity, it is the phenomenological theory of Ginzburg-Landau [13] (GL) that often is used to calculate the behavior of currents and fields in superconductors and devices. The basic premise of this theory is that the superconducting state can be viewed in terms of a single wave function consisting of a magnitude and phase, in short a complex order parameter, $\Psi(\mathbf{r}) = |\Psi|e^{i\phi}$. This they assumed to be related to the density of charge carriers by which the nondissipative supercurrent is carried, n_s, by the relation, $|\Psi|^2 \sim n_s$, which they assumed would not be dependent on phase. In essence, this wave function describes the center of mass motion of all the pairs of electrons that have condensed into the superconducting state, i.e. the Cooper pairs.

GL theory is at heart an argument based upon the energies at play in the system. In the absence of fields and currents, the free-energy density difference between the normal and superconducting states can be expressed by a series expansion in $|\Psi^2|$ or n_s, in which only the first two terms are retained

$$f_s - f_n = \alpha|\Psi|^2 + \frac{\beta}{2}|\Psi|^4. \tag{2.2}$$

For this form to give rise to superconductivity below the critical temperature, there must exist a stable minimum of $f_s - f_n$ that is below $f_s - f_n = 0$. In order for this to be the case, $\alpha < 0$ must hold true for $T < T_c$ (see Fig. 2.3). Conversely, in order for the superconducting state to become thermodynamically unstable for $T > T_c$, $\alpha > 0$ must hold there. For $\alpha > 0$, there is no value of Ψ other than zero for which the energy difference is a minimum. For $\alpha < 0$ ($T < T_c$), the minima occur at

$$|\Psi|^2 = |\Psi_\infty|^2 \equiv -\frac{\alpha}{\beta}, \tag{2.3}$$

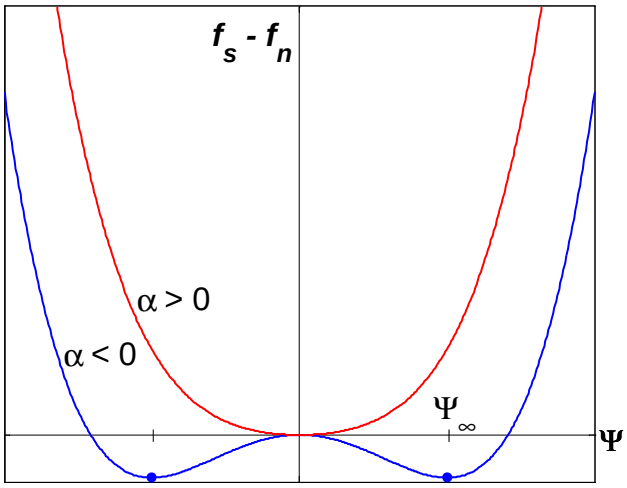

Figure 2.3 *Ginzburg-Landau free energy as a function of* Ψ *for* $\alpha > 0$ $(T > T_c)$ *and for* $\alpha < 0$ $(T < T_c)$ *[54]. Heavy dots indicate equilibrium positions.*

where the notation $|\Psi_\infty|$ is used to denote the value of the wavefunction infinitely deep inside the bulk superconductor where no fields or surface currents affect it. Equation (2.2) changes when magnetic fields or currents are present:

$$f_s - f_n = \alpha|\Psi|^2 + \frac{\beta}{2}|\Psi|^4 + \frac{1}{2m^*}\left|\left(\frac{\hbar}{i}\nabla - \frac{e^*}{c}\mathbf{A}\right)\right|^2 + \frac{h^2}{8\pi}. \tag{2.4}$$

The new terms describe the free-energy density difference's dependence on fields, gradients in the order parameter, and supercurrents. If $f_s - f_n > 0$, the superconducting state is energetically allowed, indicating that the energy gained by the electrons condensing into Cooper pairs with oppositely matched $\mathbf{k}$ vectors sufficiently exceeds the energy requirements associated with the expulsion of any magnetic field present as well as the energy costs of maintaining gradients in the wavefunction. That it costs energy for gradients (either in magnitude or phase) in the wavefunction to exist is a strong hint at the existence of the Josephson effect.

The standard approach of using GL theory to solve for the wavefunction

in a superconductor consists of minimizing the total free energy of the system, Eq. (2.4). In the absence of fields, gradients, and currents this leads to the condition that $\Psi = \Psi_\infty$ everywhere. However, when fields, gradients, or currents are present then $\Psi(\vec{r}) = |\Psi(\mathbf{r})|e^{i\phi(\mathbf{r})}$ adjusts itself to minimize the total free energy of the system which is given by the volume integral of Eq. (2.4). This problem, solved by standard variational methods, leads to the GL differential equations:

$$\alpha\Psi + \beta|\Psi|^2\Psi + \frac{1}{2m^*}\left(\frac{\hbar}{i}\nabla - \frac{e^*}{c}\mathbf{A}\right)^2\Psi = 0. \tag{2.5}$$

and

$$\mathbf{J} = \frac{c}{4\pi}\nabla \times \mathbf{h} = \frac{e^*\hbar}{2m^*i}\left(\Psi^*\nabla\Psi - \Psi\nabla\Psi^*\right) - \frac{e^{*2}}{m^*c}\Psi^*\Psi\mathbf{A} \tag{2.6}$$

or

$$\mathbf{J} = \frac{e^*}{m^*}|\Psi|^2\left(\hbar\nabla\phi - \frac{e^*}{c}\mathbf{A}\right) = e^*|\Psi|^2\mathbf{v}_s. \tag{2.7}$$

2.2 Josephson Effect

2.2.1 Josephson Equations

The Josephson effect is a result of Cooper pairs tunneling through a thin barrier or weak link between two bulk superconductors. Originally worked out for a superconductor-insulator-superconductor (SIS) geometry [19], the Josephson effect has been shown to exist for several other configurations as well. While our research deals entirely with SIS junctions, it is worth looking at the case in which the two superconducting electrodes are connected

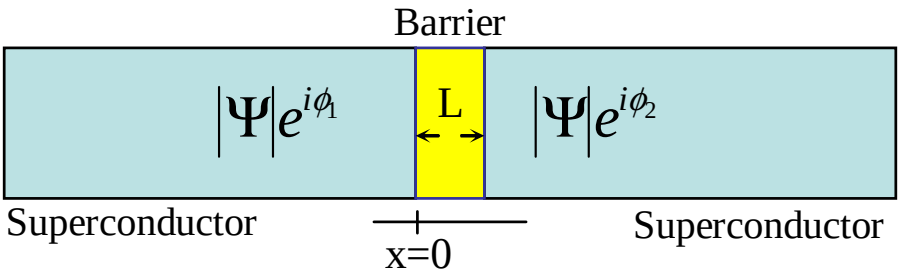

Figure 2.4 *Schematic of a Josephson junction. The barrier could be an insulator, normal metal, constriction, or other similar weak link.*

by a short metallic weak link of the same superconductor. Insofar as the Josephson effect is a general property of weak links of almost any variety, this treatment of a special case using the GL equations holds even for other types of junctions and is a simple, intuitive extension of the Ginzburg-Landau theory. Taking the first of the GL equations, Eq. (2.5), we can make the substitution $f = \Psi/\Psi_\infty$, where $\Psi_\infty \equiv -\alpha/\beta > 0$, assume there is no field present, and we get (in one dimension)

$$\xi(T)^2 \frac{d^2 f}{dx^2} + f - f^3 = 0, \tag{2.8}$$

where

$$\xi(T)^2 \equiv \frac{\hbar^2}{2m^*|\alpha(T)|} \propto \frac{1}{1 - T/T_c} \tag{2.9}$$

is the characteristic length-scale of the wavefunction, known as the coherence length. If we make the assumption that the length of the barrier is much less than a coherence length, $L \ll \xi$, we can easily solve Eq. (2.8) for f in the barrier. In accordance with Fig. 2.4, we further assume that the magnitude of Ψ in each superconducting electrode is the same, while the phase is different. Without loss of generality we can further assume $\phi_1 = 0$ and $\phi_2 = \Delta\varphi$ ($\Delta\varphi = \phi_2 - \phi_1$). Appropriate boundary conditions therefore

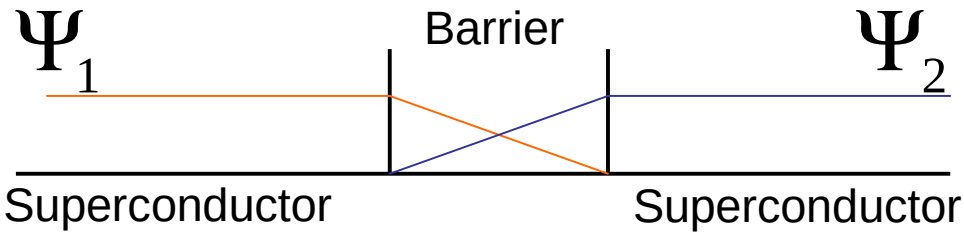

Figure 2.5 *Spread of the wavefunction from the left and right superconducting banks into the barrier*

suggest that $f = 1$ for $x = 0$ (where x is measured from one side of the weak link), and $f = e^{i\Delta\varphi}$ at $x = L$. Provided $L \ll \xi$, the first term of Eq. (2.8) dominates, since it is larger than the other two terms by a factor that scales as $(\xi/L)^2$ for any nonzero $\Delta\varphi$. In this limit, the problem reduces to Laplace's equation $d^2f/dx^2 = 0$, which has a simple linear solution. Applying the boundary conditions we arrive at the solution for f:

$$f = (1 - x/L) + (x/L)e^{i\Delta\varphi}. \tag{2.10}$$

Because of our assumption that the length of the barrier is considerably less than the coherence length, we arrive at a linear decay of the order parameter from the left superconducting bank with zero phase and from the right with a phase of $\Delta\varphi$. This shows that the integral of the gradient of the phase across a junction is simply the difference of the phase on either side of the junction.

If we insert Eq. (2.10) into Eq. (2.6) we arrive at the first of the Josephson equations:

$$I_s = I_c \sin \Delta\varphi, \tag{2.11}$$

where

$$I_c = \left(2e\hbar\Psi_\infty^2/m^*\right)(A/L)\,, \tag{2.12}$$

and A is the cross-sectional area of the junction. This treatment does not arrive at the second Josephson equation:

$$\frac{d(\Delta\varphi)}{dt} = \frac{2e}{\hbar}V, \tag{2.13}$$

although it does give some physical intuition to Eq. (2.11). Furthermore, from the dependence of I_c on (A/L) in Eq. (2.12) it is clear that the critical current scales with the junction dimensions exactly as the inverse of the Ohmic normal state resistance of the barrier.

To treat the case in which the barrier is an insulator, the fact that the electrons are condensed into Cooper pairs is necessary to explain the possibility of tunneling from one superconductor to the other. The important results are Eqs. (2.11, 2.13). For the case of a normal-metal barrier, the important length-scale is the normal-metal coherence length $\xi_N = (\hbar v_F e/6\pi k_B T)$, the characteristic distance over which the wavefunction decays in the normal-metal barrier.

Using Eqs. (2.11, 2.13), the coupling energy stored in a Josephson junction as a function of the phase across the junction can be worked out. By integrating the work done by a current source to change the phase, $\int I_s V dt = \int I_s\,(\hbar/2e)\,d\,(\Delta\varphi)$, we find

$$F = const. - E_J\cos(\Delta\varphi)\,,\ \text{where } E_J \equiv (\hbar I_C/2e)\,. \tag{2.14}$$

This result shows clearly that for the case of a standard Josephson junction,

the energy is a minimum when the two phases are equal, $\Delta\varphi = 0$. That the energy is dependent on the phase difference across the junction brings to mind the relationship expressed by GL in Eq. (2.4), in which the *gradients* in the phase of a bulk superconductor cost energy. Thus the magnitude of the critical current, which is proportional to the maximum Josephson energy, is a measure of how strongly the phases of the two superconducting electrodes are coupled. As one would expect, this depends on how thick and of what material the barrier is made. For the Josephson effect to be observed at all, the critical current must be sufficiently large that the reduction in energy due to Josephson coupling is not washed out by the thermal energy of the environment, $k_B T$, i.e. $I_C > 2ek_BT/\hbar$. If this does not hold, then thermal fluctuations in $\Delta\varphi$ will wash out the phase dependence of the supercurrent. To understand this effect it helps to explore the resistively-shunted junction (RSJ) model (see Section 2.2.3).

Thus far, we have treated the junction in the absence of magnetic fields. We dropped the term in $\mathbf{A}$ from Eq. (2.5) when we derived the first Josephson equation, Eq. (2.11). However, when magnetic fields are present, they must be taken into account. If we let that term remain in the equation, the outcome is the same, except for one important difference. The phase across the junction is no longer just the difference of the two quantum mechanical phases of the order parameters of the two superconducting electrodes, $\Delta\varphi = \phi_2 - \phi_2$. It becomes the gauge-invariant phase, which incorporates the effects of a magnetic field:

$$\phi = \Delta\varphi - \frac{2\pi}{\Phi_0}\int_1^2 \mathbf{A}\cdot d\mathbf{l}, \tag{2.15}$$

where $\Phi_0 = h/2e$ is the flux quantum. See Fig. 2.6(b) for a diagram showing

the path of the integral. The new term in Eq. (2.15) accounts for the effect of a magnetic field on the phase difference between the two superconducting electrodes. This leads to the final version of the Josephson equations:

$$\begin{aligned} I_s &= I_c \sin\phi, \\ V &= \frac{2e}{\hbar}\frac{d\phi}{dt}. \end{aligned} \tag{2.16}$$

2.2.2 Multiply-Connected Josephson Junction

In the circumstance where a Josephson junction is incorporated in a superconducting loop (a multiply-connected system), the effect of flux quantization needs to be introduced and explored. We will first consider the case in which a junction is not present in the loop, leaving us with only a loop of superconducting material to consider.

Taking a step back, it is important to remember that for a quantum mechanical particle of mass m and charge Q, the canonical momentum operator is $-i\hbar\nabla = m\mathbf{v}+Q\mathbf{A}$. Using the Schrödinger equation of motion for a particle of mass m_e and charge $-e$, we can write the supercurrent density as:

$$\Lambda\mathbf{J}_s = -\left(\frac{\hbar}{2e}\nabla\varphi + \mathbf{A}\right), \tag{2.17}$$

where we have introduced the London parameter, $\Lambda = m_e/n_s e^2$, where n_s is the superfluid density. Consider now, taking the line integral of Eq. (2.17) around a full loop (see Fig. 2.6(a)). The line integral of $-\nabla\varphi = (2e/\hbar)(\mathbf{A} + \Lambda\mathbf{J}_s)$ is the total change in the phase, φ, of the GL wavefunction, $\Psi e^{i\varphi}$ around the loop, and this value must be an integer multiple of 2π. Therefore,

$$\oint (\mathbf{A} + \Lambda\mathbf{J}_s)\cdot d\mathbf{l} = \frac{\hbar}{2e}2\pi n, \tag{2.18}$$

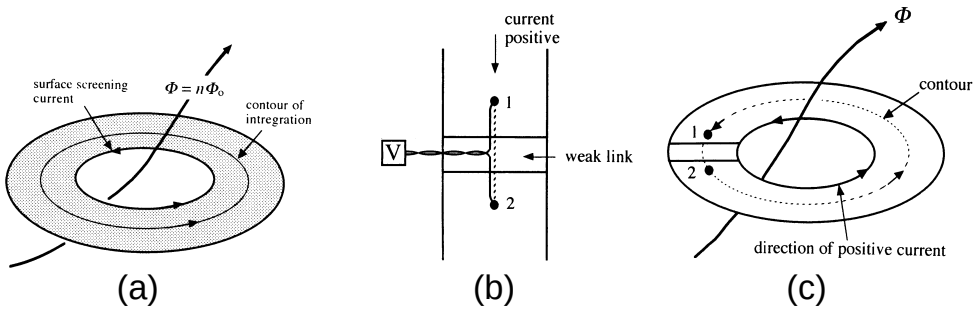

Figure 2.6 *(a) Quantization of flux in a multiply connected ring of superconducting material. (b) Path of line integral for Eq. (2.15) in the definition of φ, the gauge-invariant phase. (c) A single weak link (Josephson junction) in a superconducting loop. Illustrations from [65]*

where n is an integer. When dealing with superconducting lines large on the scale of the penetration depth, we can take the integral deep inside the material where $\mathbf{J}_s = 0$, and thus the left hand side of Eq. (2.18) reduces to $\oint \mathbf{A} \cdot d\mathbf{l}$ which is just the flux that is enclosed by the loop, Φ_t. This gives us the flux quantization condition

$$\Phi_t = \Phi_0 n. \tag{2.19}$$

We can extend this treatment to include the case when a Josephson junction is in the loop. As before, we want to integrate along a line deep in the bulk superconductor (see Fig. 2.6(c)). This allows us to drop the $\mathbf{J}$ term and write

$$\Phi_t = \oint \mathbf{A} \cdot d\mathbf{l} = \frac{\Phi_0}{2\pi} \int_{sc} \nabla\varphi \cdot d\mathbf{l} + \int_{jj} \mathbf{A} \cdot d\mathbf{l}, \tag{2.20}$$

where the subscript sc indicates an integral in the superconducting leads and jj indicates an integral in the weak link. To the second part of Eq. (2.20) we add and subtract the quantum mechanical phase difference across the

junction, $\Delta\varphi$, giving

$$\frac{2\pi}{\Phi_0}\Phi_t = \left(\int_{sc} \nabla\varphi \cdot d\mathbf{l} + \Delta\varphi\right) - \left(\Delta\varphi - \frac{2\pi}{\Phi_0}\int_{jj} \mathbf{A} \cdot d\mathbf{l}\right). \tag{2.21}$$

The first term of Eq. (2.21) is simply the total phase drop around the whole loop. Because of the single-valued nature of the wavefunction, this must be zero (modulo 2π). The second term is the gauge-invariant phase difference given by Eq. (2.15). Therefore, we end up with the following relation:

$$\phi = -\frac{2\pi\Phi_t}{\Phi_0}, \tag{2.22}$$

which implies that flux no longer need be quantized, but the phase difference across the weak link is proportional to the enclosed field and changes by 2π for a change of one flux quantum in the ring. Therefore, at any given time, there is a supercurrent flowing through the ring that is given by Eq. (2.22) and the first Josephson equation in Eq. (2.16):

$$I_{loop} = -I_c \sin\left(\frac{2\pi\Phi_t}{\Phi_0}\right). \tag{2.23}$$

In this expression, note that $\Phi_t = \Phi_x + \Phi_s$, where Φ_x is the externally applied flux while $\Phi_s = LI_s = LI_{loop}$ is the flux due to the screening current flowing through the loop. Another way to write this condition is

$$\Phi_x = \Phi_t + LI_c \sin\left(2\pi\Phi_t/\Phi_0\right). \tag{2.24}$$

As long as the total enclosed flux is an integer multiple of flux quanta, no current flows around the loop. However, for any other value of the total flux, a supercurrent will flow around the loop in order to satisfy the phase

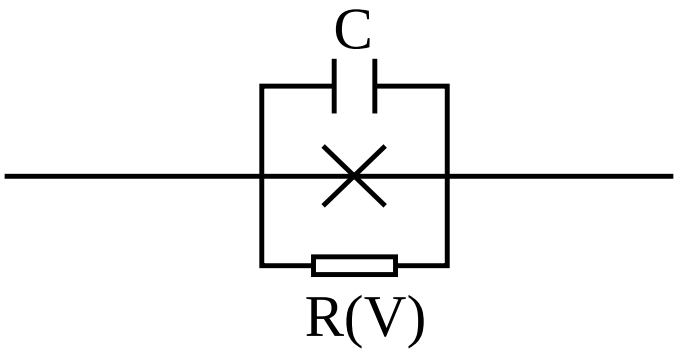

Figure 2.7 *Schematic of the RSJ model of a Josephson junction. The* ***X*** *represents an ideal Josephson junction.*

constraint, provided the inductance of the loop is large enough. If L is small, there will be no circulating current at $\Phi_t \approx 1/2\Phi_0$.

2.2.3 RSJ Model

The resistively shunted junction (RSJ) and the resistively and capacitively shunted junction (RCSJ) models more fully describe the behavior of Josephson junctions. The RSJ approach to a Josephson junction models the junction as the parallel combination of an ideal Josephson junction with a resistor and capacitor. The capacitor in the model accounts for the capacitance that is due to charge buildup on either side of the Josephson junction barrier, while the resistor's presence accounts for the subgap quasiparticle conduction. For junctions close to T_c, R is well approximated by R_n, the normal state resistance. However, for a high quality SIS junction at low temperatures, R rises exponentially as $R_n e^{\Delta/k_B T}$ (for $V < V_{gap} \equiv 2\Delta/e$). The dominant exponential behavior arises from the freezing-out of quasiparticles at low temperatures but not the singular nature of the density of states at the gap edge.

Based upon the circuit diagram of Fig. 2.7, we can write down an equation for the time dependence of the phase by equating the total bias current to

the current through the three parallel channels:

$$I = I_{c0} \sin\phi + \frac{V}{R} + C\frac{dV}{dt}. \tag{2.25}$$

In this expression the factor I_{c0} is introduced to differentiate from I_c, which will denote the observable critical current. Using Eq. (2.16) to eliminate V in favor of the phase, ϕ, we get a second-order differential equation:

$$\frac{I}{I_{c0}} = \sin\phi + Q^{-1}\frac{d\phi}{d\tau} + \frac{d^2\phi}{d\tau^2}, \tag{2.26}$$

where we have introduced the dimensionless parameter $\tau = \omega_p t$, in which

$$\omega_p = \left(\frac{2eI_{c0}}{\hbar C}\right)^{1/2} \tag{2.27}$$

is referred to as the plasma or small-oscillation frequency of the junction. We can also define a dimensionless factor,

$$\beta_c = 2\pi I_c R^2 C/\Phi_0, \tag{2.28}$$

which is a measure of the damping present in the junction. We can simplify this relation by expressing β_c in terms of ω_p, $\beta_c^{1/2} = \omega_p RC$.

The equation of motion given in Eq. (2.26) is identical to that for a particle in a potential known as the "tilted-washboard" potential (see Fig. 2.8):

$$U(\phi) = -E_J \cos\phi - \left(\frac{\hbar I}{2e}\right)\phi. \tag{2.29}$$

In this model, the phase across the Josephson junction could be thought of as the position of particle with mass $(\hbar/2e)^2 C$.

Looking at the picture of the washboard potential, it becomes obvious

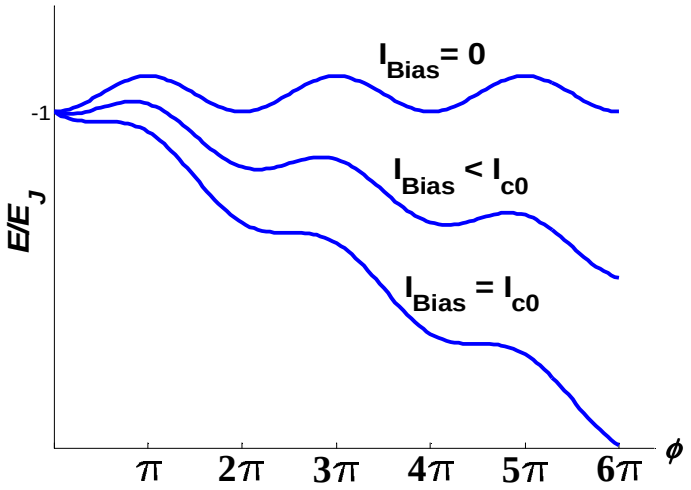

Figure 2.8 *Tilted-washboard potential for three different values of bias current. The minima are periodic in ϕ, and for $I_{bias} > I_{c0}$ there are no local minima.*

what several of the previously-defined parameters mean. The plasma frequency is the frequency of oscillation of the phase/particle in the limit of small oscillations about a local minimum for which the potential is best approximated as a harmonic oscillator. The meaning of the critical current and our use of I_{c0} is evident. When the bias current equals the fluctuation-free critical current, I_{c0}, the local minima of the tilted-washboard become horizontal inflection points. After this condition is reached there is no stable equilibrium point, and the phase will continually advance, resulting in a finite voltage across the junction.

Given particular values for R and C, the motion of the phase/particle in the washboard potential will either be overdamped or underdamped. These two circumstances lead respectively to non-hysteretic or hysteretic current-voltage characteristics. We use β_c as the parameter that determines the damping of the Josephson junction. If $\beta_c < 1$ then the junction is overdamped, and this leads to a simple expression for the voltage as a function

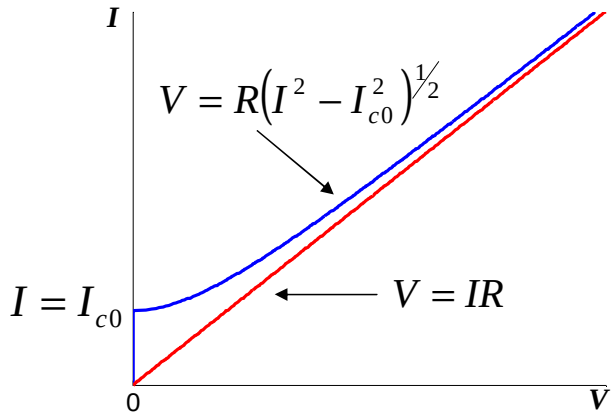

Figure 2.9 *I-V curve for an overdamped ($\beta_c < 1$) Josephson junction. At large bias currents it approaches Ohmic behavior, with $R \cong R_n$.*

of the bias current:

$$V = R\left(I^2 - I_{c0}^2\right)^{1/2}. \tag{2.30}$$

Shown in Figure 2.9, the voltage smoothly interpolates from $V = 0$ for $I < I_{c0}$ to $V = IR$ for $I \gg I_{c0}$. This circumstance corresponds to either heavy damping of the phase particle in the washboard potential (low R in Fig. 2.7) or to a very low mass and inertia of the particle (small C in Fig. 2.7). Because the capacitance is determined by the area and thickness of the junction, the usual way to select for the level of damping in a Josephson junction is by adding an additional shunt resistor in parallel with the junction in order to decrease the resistance of the junction.

When $\beta_c > 1$ the junction is underdamped and will exhibit hysteretic behavior in the $I - V$ curve. In this case, either C or R is large, again corresponding to a high "mass" or very little damping. As I is increased from zero, V remains zero until I reaches I_{c0}, at which time V jumps discontinuously from zero to $V_{gap} = 2\Delta/e$. After this abrupt switch, the phase starts "running," and increases at a rate of $2eV/\hbar$. As I is increased further,

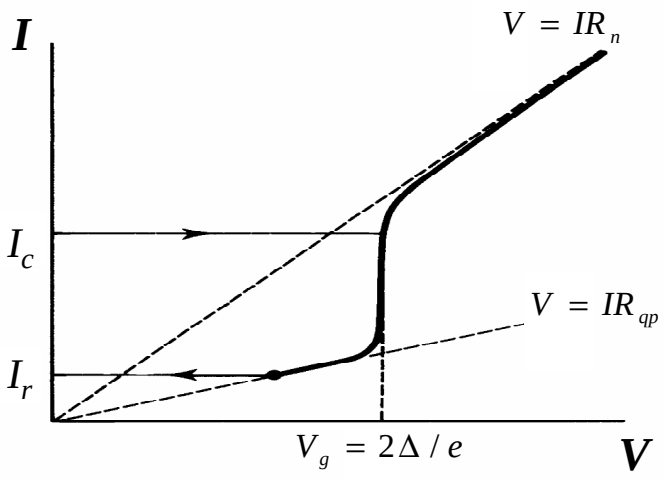

Figure 2.10 *$I-V$ curve of an underdamped Josephson junction. From [54]*

the voltage across the junction approaches the Ohmic value of $V = IR_n$. If we now reduce I below I_{c0}, the voltage does not jump back to zero at I_{c0}. Instead, it does not go back to the zero voltage state until a "retrapping" current is reached at $I \approx 4I_{c0}/\beta^{1/2}$. In the particle in a washboard potential analogy, this reflects the ability of the inertia of the particle (under very light damping) to carry it over the barrier, which would not happen for larger damping.

2.2.4 Thermal Fluctuations

Mathematically, thermal fluctuations can be accounted for by adding a Johnson noise current to the bias current expression in Eq. (2.25) [1], or by considering the effects of thermal fluctuations on a particle resting in the washboard potential [54]. For the underdamped case, thermal fluctuations lead to a decrease in the observed critical current. Simply put, if the phase particle is sitting in one of the local minima of the tilted washboard potential, then for a constant bias current and in the absence of thermal fluctuations

and macroscopic quantum tunneling, it will remain there indefinitely. However, for a constant bias current but this time with thermal fluctuations, the phase particle's energy receives kicks from thermal energy. This added energy has a small probability, $\sim \exp(-\Delta U(I)/k_B T)$, per attempt to bump the particle over the barrier. The attempt frequency for a particle in the tilted-washboard potential is the small oscillation frequency of the phase particle at the minimum of the tilted washboard potential. We can write ω_A, the attempt frequency as

$$\omega_A = \omega_p \left[1 - (I/I_{c0})^2\right]^{1/4}. \tag{2.31}$$

Unless I is negligibly different than I_{c0}, the difference between ω_A and ω_p is slight, although it may also depend on damping in some regimes. Because the junction is underdamped, once the particle has gone over the barrier the phase will continue to evolve, and the junction will then be in the finite voltage state. Because this is a stochastic process it leads to a distribution of values for I_c, the value of the bias current at which a junction will switch to the finite-voltage state. The mean of this distribution will necessarily be less than I_{c0}. Although numerical calculations are required for quantitative results (see [12], for example), the mean value of I_c can be approximated by

$$\langle I_c \rangle = I_{c0} \left\{ 1 - \left[\left(\frac{k_B T}{2E_J} \right) \ln \left(\frac{\omega_p \Delta t}{2\pi} \right) \right]^{2/3} \right\}, \tag{2.32}$$

where Δt is the time spent sweeping the current through the region close to the mean of the distribution.

When a thermal Johnson noise current is added to Eq. (2.25), the $I - V$ curve of an overdamped junction is fundamentally altered [1] from the form

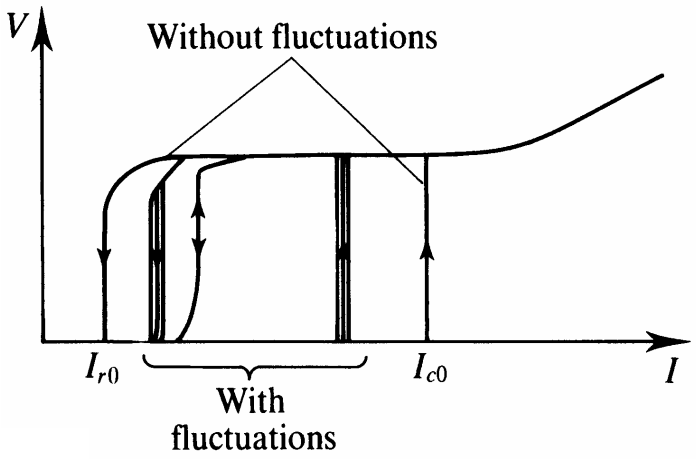

Figure 2.11 *Sketch of the effect of thermal fluctuations in reducing and eventually eliminating hysteresis in underdamped Josephson junctions. From Ref. [54].*

given by Eq. (2.30). In particular, there is a finite resistance below I_c. In the washboard potential model the phase actually "diffuses" over the barrier, as opposed to a single escape event. This occurs because the heavy damping of the junction brings the phase particle back to an equilibrium in the next minimum before it can diffuse to the next barrier, so it has no chance to run away, as it does in an underdamped junction. This results in a rounding of the $I-V$ characteristics of a Josephson junction, as shown by Ambegaokar and Halperin [1] in 1969. The voltage across the junction can be expressed as a function of the dimensionless parameters

$$\gamma = \frac{\hbar I_c(T)}{e k_B T} \text{ and } i = \frac{I}{I_c}. \tag{2.33}$$

The first of these parameters indicates how rounded the $I-V$ is: the higher γ is, the less rounding there is. In short, the mean voltage across an overdamped junction in the presence of thermal fluctuations is

$$\langle V \rangle = \frac{2}{\gamma} R I_c \frac{\exp(\pi\gamma i) - 1}{\exp(\pi\gamma i)} T_1^{-1}, \tag{2.34}$$

where $T_1 = \int_0^{2\pi} \exp\left(-\frac{\gamma}{2}\alpha\varphi\right) I_0\left(\gamma \sin\frac{\varphi}{2}\right) d\varphi$, in which I_0 is a modified Bessel function. At high temperatures, $\gamma \to 0$ and $V \to IR_N$, while when the temperature goes to zero, $\gamma \to 0$ and the zero noise case is reproduced and the form given by Eq. (2.30) is recovered: $V = R\,(I^2 - I_c^2)^{1/2}$. The $I - V$ characteristics and differential resistance curves are calculated and plotted for several values of γ in Fig. 2.12.

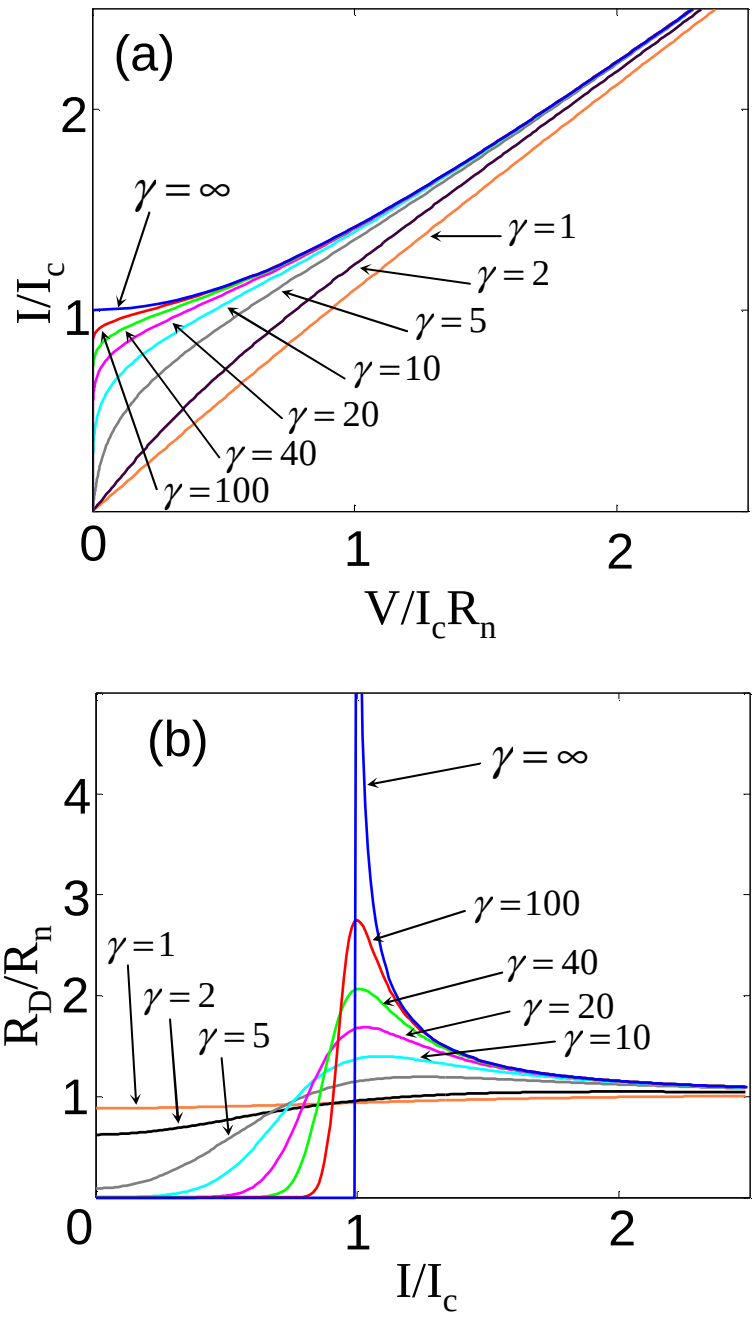

Figure 2.12 *(a) $I-V$ characteristic of a Josephson junction for different values of $\gamma = \hbar I_c(T)/ek_BT$. (b) Differential resistance ($R_D = dV/dI$) for several values of γ.*

3 1/f Noise

In this chapter we will look at the phenomenon of $1/f$ noise in general, touching on the more important theoretical attempts to explain it. We will also review attempts by other research groups to measure $1/f$ noise in Josephson junctions or SQUIDs.

Because of the near-ubiquity of $1/f$ noise condensed matter systems, it is tempting to search for a universal mechanism. However, because such a wide range of systems (from traffic flow to carbon resistors to SQUIDs) exhibit low frequency noise, it seems unlikely that there are a cohesive set of equations of motion that are universally valid in these systems. Therefore, most of the theoretical work done, to date, on explaining $1/f$ noise dynamics focuses primarily on a relatively small subset of systems. For our purposes, we will only worry about physical systems that are closely related to (or lend themselves to analogy with) Josephson junctions, such as semiconductors and/or metals and insulators.

3.1 Theory of 1/f Noise

3.1.1 Hooge Model

In general, we measure the voltage of a sample such as a resistor or junction as a function of time, $V(t)$. As a rule, if the process that is producing the noise we measure is stationary and Gaussian, we can assume that the

power spectrum of the noise uniquely characterizes the process. The spectral density (or power spectrum) is defined as the Fourier transform of the autocorrelation function, $C_V(t)$:

$$S_V(f) = \int_{-\infty}^{\infty} C_V(t) e^{-i2\pi ft} dt,$$
$$C_V(t) = \langle V(t)V(0)\rangle - \langle V\rangle^2 . \tag{3.1}$$

For a resistor exhibiting Johnson noise, this yields the well-known result $S_V(f) = 4k_BTR$, for $k_BT \ll hf$. However, $1/f$ noise is so called because the spectrum, $S_V(f)$ is not independent of f. Instead, $S_V(f) \propto 1/f$.

The starting point of much of the treatment of $1/f$ noise is with Hooge's empirical formula [16]:

$$S_V(f) = \gamma \frac{V_{DC}^{2+\beta}}{N_c f^{\alpha}}, \tag{3.2}$$

where α, β, and γ, are constants ($\beta \approx 0$), and N_c is the number of charge carriers in the sample. The inverse dependence on N_c was proposed by Hooge in order to unify the noise processes in metals and superconductors with $\gamma \simeq 2 \times 10^{-3}$. Note that γ is dimensionless only if $\alpha = 1$ and $\beta = 0$. According to this equation, the noise is independent of temperature and material parameters and is a power law at all frequencies. And while Eq. (3.2) fits a large amount of data from past experiments (see for example [16, 17, 23, 52, 58]), it is a postulate and has little theoretical basis that would lead one to expect any underlying tendency toward this behavior.

As an example of one flaw, Eq. (3.2) predicts a universal dependence on f, as mentioned above. This is clearly unphysical. Specifically, $\int_0^{\infty} f^{-\alpha} df = \infty$. For $\alpha = 1$, as in Hooge's formula, the integral diverges at both ends. There-

fore, if $S_V(f) \propto f^{-\alpha}$, the zero-time correlation function, $C_V(0)$ diverges. In short, if the process is stationary (as we expect it is), there must exist "rolloffs" at both high and low frequencies. That is, for sufficiently low frequencies $\alpha < 1$ should be true, while for sufficiently high frequencies $\alpha > 1$ should likewise be the case. Therefore, even though $1/f$ noise is commonly viewed as a low-frequency phenomenon, it is in fact an intermediate-frequency behavior. For any theory involving stationary processes with upper and lower characteristic times, the presence of these rolloffs is indisputable. Depending on the frequency range over which measurements of the $1/f$ noise is performed, these rolloffs will dominate the spectrum or be unobservable altogether.

3.1.2 Activated Random Processes

Another possible cause of $1/f$ noise is the existence of a random process with a single characteristic time, τ. This process would result in a Lorentzian feature to the power spectrum:

$$S(\omega) \propto \frac{\tau}{\omega^2\tau^2 + 1}. \tag{3.3}$$

Thus, many spectra could be constructed based on the distribution of characteristic times giving

$$S(\omega) \propto \int \frac{\tau}{\omega^2\tau^2 + 1} D(\tau) d\tau. \tag{3.4}$$

For the case of $1/f$ noise, $D(\tau) \propto \tau^{-1}$ over a finite region $\tau_1 < \tau < \tau_2$ gives rise to $S(f) \propto f^{-1}$ for $\tau_2^{-1} \ll \omega \ll \tau_1^{-1}$. If, as is often the case, τ is thermally

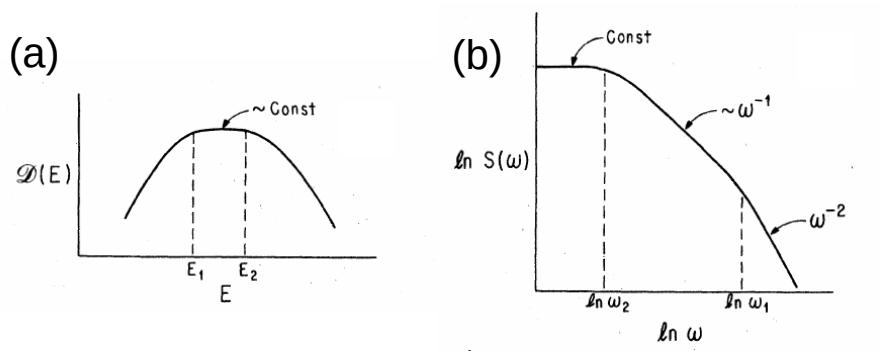

Figure 3.1 *(a) "Flat" energy distribution. (b) Frequency spectrum resulting from this distribution according to the model described by Eq. 3.4. From [9]*

activated, i.e.

$$\tau = \tau_0 e^{E/k_B T}, \tag{3.5}$$

then the required energy distribution is constant over a finite region: $D(E) = const.$ for $k_B T \ln(\tau_1/\tau_0) \leq E \leq k_B T \ln(\tau_2/\tau_0)$. This shifts the burden of justifying $1/f$ noise to explaining a region of constant activation energies. The first specific version of such a model is the McWhorter model of charge fluctuations at a semiconductor-oxide interface [38]. In this model, the exponential variation of the characteristic time τ is dependent on the distance of the trapping sites in the oxide from one contact to the other.

Despite the plausibility of this model, in fact it explains very few cases of measured $1/f$ noise. See [66] for a more in-depth discussion of the shortcomings of this model.

3.1.3 Dutta-Dimon-Horn Model

Likely the largest single step forward in getting a handle on the theoretical underpinnings of $1/f$ noise in solid state systems came from the work of Dutta, Dimon and Horn [8, 9, 66]. Although this model is similar to the

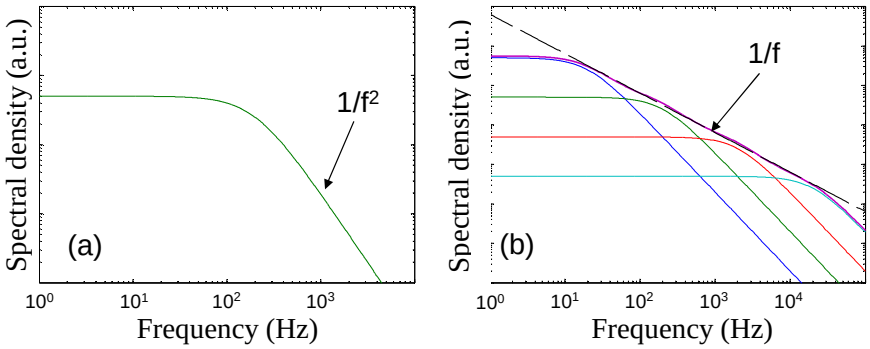

Figure 3.2 *(a) Power spectrum due to a single Lorentzian with the form given by Eq. 3.6. (b) Four TLS (two-level systems) are present. Their individual Lorentzians sum to produce a power spectrum that is very nearly* $1/f$ *over a finite region.*

activated random process model described above, it is more general and, among other things, arrives at a well-verified relationship between the slope of the power spectrum and the temperature dependence of the magnitude of the noise.

While previous models assumed a materials dependent source of $1/f$ noise, the Dutta-Horn model assumes that a number of thermally activated switching events occurring in two-level systems can superpose to produce a $1/f$ spectrum in a sample. Each two-level system (TLS) will produce a Lorentzian feature in the power spectrum:

$$S_i(\omega) \propto \frac{\tau_i}{\omega^2 \tau_i^2 + 1}. \tag{3.6}$$

When several TLS are present, their respective noise adds, creating an overlap of their power spectra. This produces a spectrum that is nearly $1/f$ over some finite bandwidth (see Fig. 3.2). More generally, and as assumed in the model developed by McWhorter, the fluctuating quantity does not need to be a TLS. The fluctuating quantity can assume a continuous distribution of values, but most current models (based on the work done by Dutta, Dimon,

and Horn) assume the simplifying case of individual two-level fluctuators.

The signal from a TLS is random telegraph noise. It is characterized in the spectrum by a single corner frequency given by the lifetimes of each state. The lifetime corresponding to the rolloff frequency of the Lorentzian produced will be [31]

$$\frac{1}{\tau_{\text{eff}}} = \frac{1}{\tau_1} + \frac{1}{\tau_2}, \tag{3.7}$$

where τ_1 and τ_2 are the lifetimes of the individual metastable states. A representative TLS would be a specific ion configuration that switches between two different arrangements, each of which affect the conductivity of sample differently. Another possibility, more in line with our view of the cause of $1/f$ noise in Josephson junctions, would be a localized defect site in the amorphous *AlO* junction barrier. Electrons would trap and untrap from the site, effectively blocking or unblocking a small conduction region of the junction, resulting in an effective change in the area of the junction and, hence, the critical current of the junction.

We can assume an exponential relation between the individual transition times and the associated trap energy, which has the same form as given by Eq. (3.5). This form derives from the fact that the TLS in question possess thermally activated noise kinetics. The lifetime of each state will be

$$\begin{aligned} \tau_1 &= \tau_0 e^{\left(E^{\pm}+\Delta E/2\right)/k_B T} \\ \tau_2 &= \tau_0 e^{\left(E^{\pm}-\Delta E/2\right)/k_B T}, \end{aligned} \tag{3.8}$$

where $E^{\pm}$ is the energy difference between the transition state and the average of the two metastable states [66] (see Fig. 3.3). This leads to a power

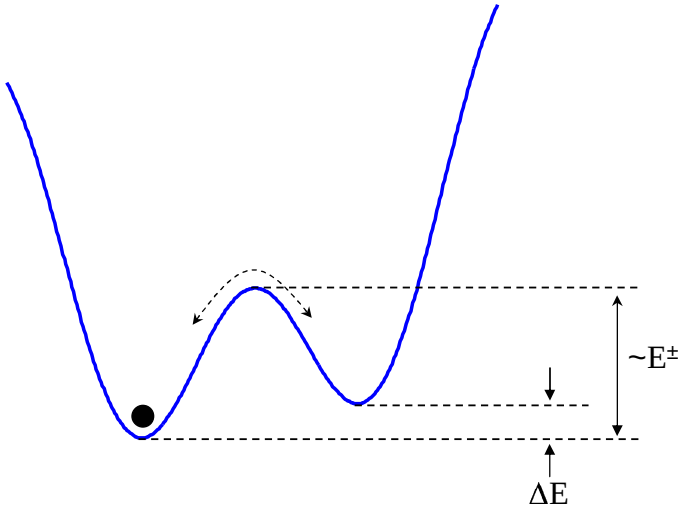

Figure 3.3 *Schematic showing the relevant energies, ΔE and $E^{\pm}$, for a two-level system in the classical regime adapted from [66]. Also as noted in [66], in the quantum regime the configuration coordinate will no longer be entirely localized in either well, but the energy difference of the eigenstates will still be close to ΔE as long as the barrier is large in comparison.*

spectrum identical in form to that given by Eq. (3.4):

$$S(\omega) \propto \int f\left(E^{\pm}, \Delta E, \omega\right) D(E^{\pm}, \Delta E) d(E^{\pm}, \Delta E), \tag{3.9}$$

where $f(E^{\pm}, \Delta E, \omega) = \tau_{\text{eff}} / \left(\omega^2 \tau_{\text{eff}}^2 + 1\right)$. Although the requirement that $D(E^{\pm}, \Delta E)$ be flat over some region still rigidly holds, it is actually only necessary that $D(E^{\pm})$ vary slowly compared to $k_B T$ for $S(\omega)$ to be "generic" $1/f$ noise, that is, $S(\omega) \propto f^{-\alpha}$ for $0.8 < \alpha < 1.4$. When $D(E^{\pm})$ varies slowly over a range $k_B T$ we can rewrite Eq. (3.9) as

$$S(\omega, T) \propto \frac{k_B T}{\omega} D(\tilde{E}), \tag{3.10}$$

where we have assumed that the distribution of energies is limited to a small region around $\tilde{E} \equiv -k_B T \ln(\omega \tau_0)$, the value of $E^{\pm}$ at which $f(E^{\pm}, \Delta E)$ is peaked.

This form gives us the temperature and frequency dependence of the magnitude of the noise, based upon the underlying assumption that the distribution of activation energies is either constant or slowly varying. However, if the constraint requiring a constant distribution of activation energies is relaxed, the dependence of $S(\omega, T)$ becomes a more complex function of its arguments. In this case, Dutta and Horn [8, 9] arrived at a relationship between the local frequency exponent, $\alpha \equiv -\partial \ln S / \partial \ln \omega$ and the temperature:

$$\alpha(\omega, T) = 1 - \frac{1}{\ln(\omega\tau_0)} \left(\frac{\partial \ln S(\omega, T)}{\partial \ln T} - 1 \right). \tag{3.11}$$

Effectively, Eq. (3.11) suggests that the temperature dependence of the noise magnitude becomes stronger as the spectral slope (α) deviates from unity.

Further insight into the Dutta-Horn model can be gained by multiplying the spectrum by the frequency, $S(\omega, T) \times \omega$, so that deviations from the ideal $1/f$ relationship appear as peaks (or troughs), which dominate the noise at their characteristic frequency. In short, a $1/f$ spectrum would now appear as a horizontal line and the location of the corner frequency of individual Lorentzians will be easier to track as a function of temperature. If a particular Lorentzian feature is thermally activated, the location of its corner frequency will increase with temperature, following Eq. (3.8) (see Fig. 3.4). In the limit of many fluctuators ($> 1/octave$), this leads to the result that the magnitude of the noise depends on temperature and frequency, as in Eq. (3.10). Furthermore, $S(\omega, T) \times \omega$ is proportional to the distribution of activation energies, $D(\tilde{E})$, from Eq. (3.10). This points to a characteristic energy for the activated process, which is an important clue as to the nature of the observed TLS.

This model runs into problems, though, when dealing with low tempera-

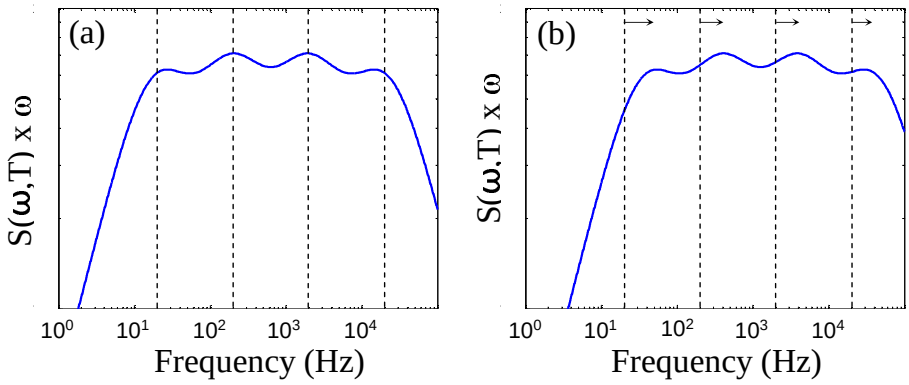

Figure 3.4 *(a) When $S(\omega, T)$ is multiplied by ω, $1/f$ noise becomes horizontal, making it easy to identify the characteristic frequency of a Lorentzian. (b) At higher temperatures, the corner frequency of the individual Lorentzians shift to higher frequency, in keeping with Eq. (3.8). Adapted from [62].*

tures. Being based upon the assumption that TLS are thermally activated, the Dutta-Horn model does not account for the switching behavior of TLS at extremely low temperatures. In this regime, the TLS are no longer thermally activated but are, instead, limited in their switching rate by the quantum tunneling rate, and in this regime the Dutta-Horn relationship does not apply. However, its applicability is extremely wide, given that it only requires the noise spectrum to depend on some characteristic parameter that has a broad distribution. Because of this, we still find it useful to understand our system. It should be noted that there are other flaws in the assumptions that lead to the Dutta-Horn results, and these are addressed at length in [66].

Despite any shortcomings in the Dutta-Horn model, a significant amount of work has been done that verifies the model in general. Examples include work done by Rogers and Buhrman [47, 48] measuring $1/f$ noise in metal-insulator-metal tunnel junctions. Shown in Fig. 3.5 are several plots indicating how well the thermal activation of individual TLS follows the exponential form given by Eq. (3.8). Furthermore, Fig. 3.5(c) illustrates quite clearly that the thermal activation model breaks down at temperatures low

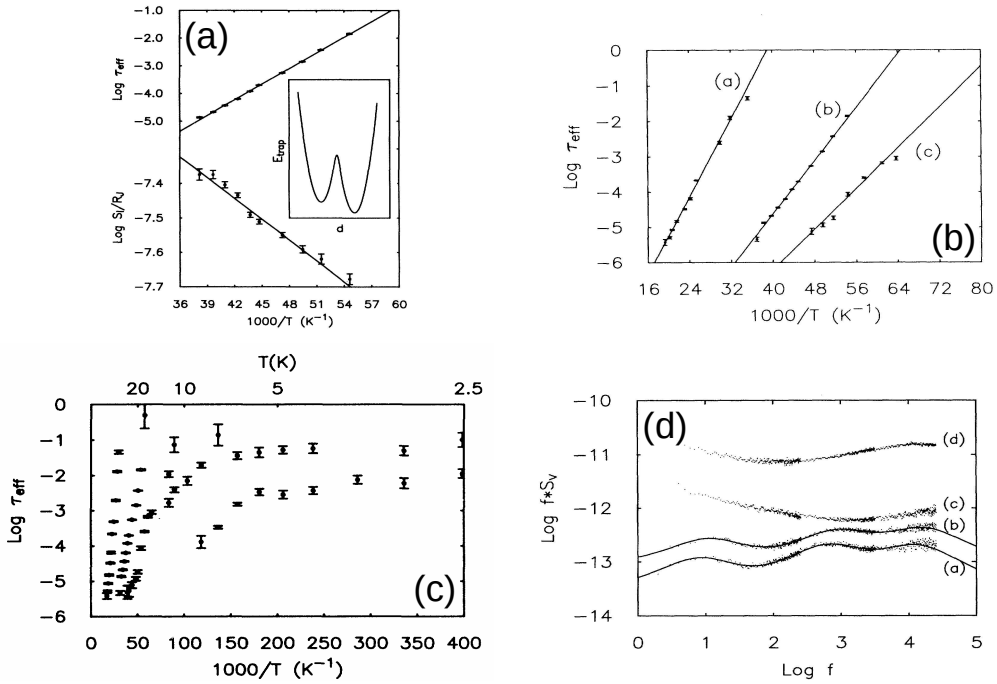

Figure 3.5 *(a) Plot of* $\log(\tau_{\text{eff}})$ *and* $\log(S_1)$ *vs.* $1/T$ *showing thermally activated behavior. Solid lines are fits assuming Eqs. (3.7, 3.8). Inset shows a double-well model which describes the rate-limiting kinetics. (b) Several activated rates showing exponential relationship of* τ *and the activation energy. (c) Plot showing an abrupt change from thermally activated behavior to nonactivated behavior below* $T \approx 15$ *K. (d)* $S(\omega, T) \times f$ *for a metal- insulator-metal tunnel junction. The solid lines are fits to* < 5 *individual Lorentzians. Traces c and d cannot be fit accurately with less than five Lorentzians. Subfigures (a) and (c) are from [48], while (b) and (d) are from [47].*

enough that the thermal energy is insufficient to cause a switching event.

3.2 Previous Work Measuring 1/f Noise in Josephson Junctions

Considerable work has been done by various groups in the measurement of $1/f$ low-frequency noise in Josephson junctions or SQUIDs [63, 64, 62, 10, 40, 49, 70, 7, 41, 37, 21, 20]. However, most of the measurements were taken at temperatures above 1 K, were performed on a SQUID or high-T_c Josephson

junctions, or some combination of all these.

There have been many measurements of $1/f$ noise in Josephson junctions (for example, [24, 10, 49]), but the first low temperature measurements (and measurements as a function of temperature) were made by Wellstood as a graduate student in Clarke's group at UC Berkeley. At the time, they did not publish their results [67], which indicated a T^2 dependence of the noise magnitude versus temperature down to approximately 300 mK. However, in 2004 they did publish this result [70], in addition to pushing their findings down to 90 mK.

There are several significant elements to their work that deserve our attention. The first of these is that they actually measured the $1/f$ noise present in dc SQUIDs. This is important because SQUIDs can exhibit $1/f$ noise due to critical-current fluctuations or from flux hopping and/or creep. Secondly, the junctions measured were, at their smallest, $2 \times 2\ \mu m^2$. This is a good place to start, as that size scale is easily fabricated using standard photolithographic techniques; however, insofar as we intend to measure the $1/f$ noise of junctions similar in size and geometry to those used in qubits (i.e. $\sim$100$\times$100 nm^2), the results obtained by Wellstood are not entirely conclusive. Additionally, their data begs the question of why they see a T^2 dependence as far down in temperature as they do. Based on the picture of thermally activated TLS kinetics, we expect the T dependence to flatten at sufficiently low temperatures. It is true that we do not know what temperature to expect this flattening in Josephson junctions to begin at, but it is not unreasonable to expect it to occur at a higher temperature than 90 mK, considering Rogers and Buhrman's work pictured in Fig. 3.5. Finally, while the measurement circuit they used shares some similarities, there are also important differences from our proposed circuit (see Chapter 7), so there is

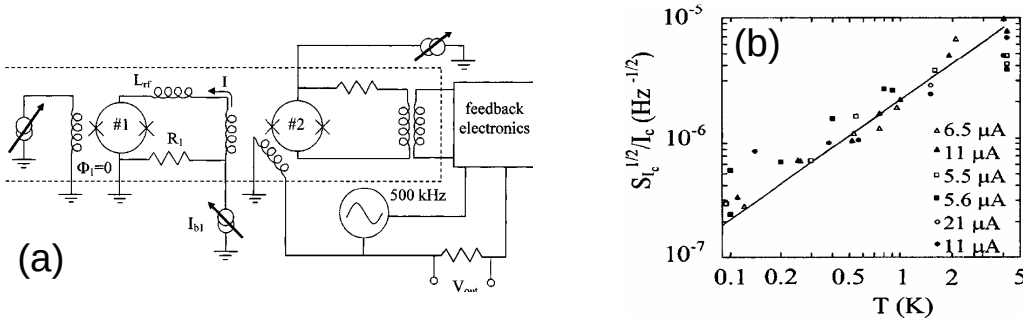

Figure 3.6 *(a) Experimental configuration used by F. Wellstood et al. [67, 70] to measure* $1/f$ *noise. (b) Normalized critical current noise* $S_{I_c}^{1/2}(1\ Hz)/I_c$ *vs. temperature for six devices with critical currents listed. A line of slope unity has been fitted to data. Figures and some text from [70].*

also the question of how the differing approaches will affect the measurement.

These are all issues that are recognized and, to some degree, addressed in [70], but as of yet, no clear results have answered any of the concerns mentioned above. In particular, given the proposed mechanism of electron trapping/untrapping in the oxide, they focus on the inconsistency of their measured temperature dependence (T^2) with the fact that the availability of electrons to trap, and states for them to go when they untrap, scales as $\exp(-\Delta/k_BT)$, where Δ is the superconducting gap. Their observed temperature dependence is incompatible with this exponential scaling.

For future reference, it needs to be mentioned that the circuit used by Wellstood *et al.* is similar to what we used. One of the primary differences is that they measured dc SQUIDs while we measured single junctions, though by the same token we both current bias our respective measured elements. Another difference, which is perhaps just as important, is the fact that their measurement is based on a low-impedance technique. In Fig. 3.6(a), there is a resistor, $R_1 \ll 1\ \Omega$, which is in series with the SQUID they measure (#1 in the diagram). They bias this SQUID to the point where the dynamic resis-

tance is the same as the SQUID shunt resistance, $R_D \sim R_s \sim 10\ \Omega$, allowing them to make the simplifying assumption that any current fluctuations they measure through the coupling of the test loop to the measurement SQUID (#2 in the diagram) are the same as the critical-current fluctuations of the SQUID (#1) itself. As we shall see in Section 7.3, this measurement scheme is different from ours in that we use a high-impedance approach.

Because the root cause of the $1/f$ critical-current noise is thought to be charge motion, it is worth examining at least one work that arrives at a T^2 dependence in SETs (single electron transistors) [22]. They assume a charged defect moves between two locations, resulting in a TLS that lives in an asymmetric double-well potential. They write the power spectrum resulting from the superposition of these Lorentzian-producing TLS as

$$\begin{aligned} S_q &= \frac{(\delta Q_0)^2}{\pi} \int_0^\infty \int_0^\infty d\epsilon_1 d\epsilon_2 D(\epsilon_1, \epsilon_2) \\ &\times \frac{1}{\tau_1(\epsilon_1) + \tau_2(\epsilon_2)} \frac{1}{(2\pi f)^2 + \left(\frac{1}{\tau_1(\epsilon_1)} + \frac{1}{\tau_2(\epsilon_2)}\right)^2}. \end{aligned} \tag{3.12}$$

Here $D(\epsilon_1, \epsilon_2)$ is the distribution of activation energies, where $\epsilon_{1,2}$ is the respective barrier height as seen by a particle on side 1,2 of the double-well potential. Furthermore, in the above integral, f is the frequency and they make the simplifying assumption that each fluctuator in the SET causes the charge to shift by an amount δQ_0. Their final two assumptions are that $D(\epsilon_1, \epsilon_2)$ is independent of either ϵ_1 or ϵ_2 and that $1/\tau_{0,1} = 1/\tau_{0,2} \gg f$, where $1/\tau_i(\epsilon_i) \equiv 1/\tau_{0,i} \exp(-\epsilon_i/k_B T)$. Based upon these various assumptions, they arrive at a simple expression for the dependence of the magnitude of the noise power on the temperature:

$$S_q \approx D(\epsilon_1, \epsilon_2)(\delta Q_0)^2 \frac{(k_B T)^2}{f}. \tag{3.13}$$

They attribute the T^2 dependence (in contrast to the linear dependence found in [8, 9] and summarized in Section 3.1.3) on their inclusion of exactly two degrees of freedom, ϵ_1 and ϵ_2. This suggests the possibility of a framework in which a T^2 dependence is reasonable to expect; however, it relies upon a number of assumptions that do not always hold true, and still assumes an exponential thermal activation mechanism.

In addition to the work done by Wellstood *et al.*, Wakai and Van Harlingen made a number of measurements of $1/f$ noise in superconducting Josephson junctions [62, 63, 64]. Their measurements focused on dc SQUIDs as well as unshunted (and thus hysteretic) Josephson junctions. This work covered the temperature range from 1-4 K. Edge junctions were used for these measurements and were on the order of 0.05-0.12 μm^2 in area. This work was important for the fact that they directly observed TLS dynamics at work in the junctions. They were able to determine individual lifetimes of each state and unequivocally show that the low-frequency noise dynamics of Josephson junctions is dominated by the presence of TLS, most likely in the oxide barrier. In this same experiment, they were able to observe multi-level systems (i.e. ones possessing more than two metastable states). Further work presented evidence of trap-trap interaction leading to series kinetics, in contrast to the parallel-trap kinetics previously thought to be the exclusive mechanism for low-frequency noise in these small-scale junctions.

The data from Wakai and Van Harlingen further supports the picture of some defect site that traps charge carriers or perhaps an ionic configuration that leads to a change in a conduction channel. Either of these possibilities would lead to a change in the critical current. However, this data does not address the temperature dependence of the observed $1/f$ noise at temperatures lower than 1.5 K. Given the 15 K threshold established by Rogers and

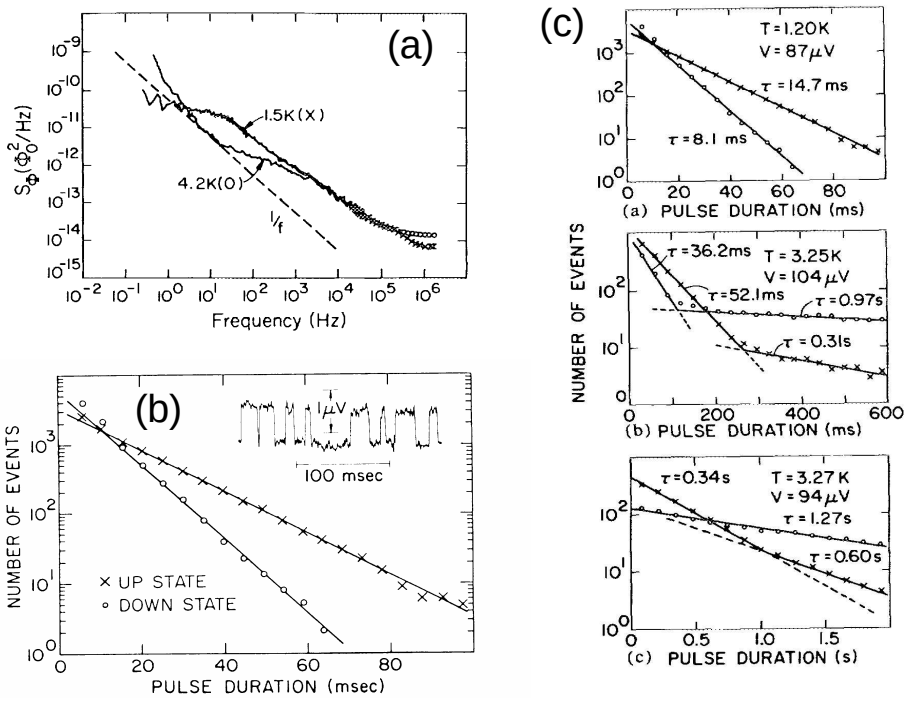

Figure 3.7 *(a) Equivalent flux power spectrum for a dc-SQUID showing a single Lorentzian at 1.5 K and at 4.2 K. (b) Histogram of electron untrapped (up) and trapped (down) times for a single two-state defect trap. Inset: real-time voltage. (c) Three different distributions of switching times for trapped and untrapped defect sites for dc-SQUIDs. The top box shows a single TLS. The middle box shows two independent TLS, and the lower box shows a three-level switching process. All graphs from [63, 64].*

Buhrman (see Fig. 3.5 and [47, 48]) and the weak dependence of the trap lifetimes on T, they believed they were measuring the noise in the quantum-tunneling regime.

Other groups (see [41], for example) have attempted to measure the low-frequency noise present in SQUIDs at zero bias. The rationale behind this measurement is that junctions used in qubits are almost always used in the zero-voltage state, so it makes sense to try to measure the noise in the same state. The net result is that the noise measured using a flux-bias scheme, which allows them to avoid biasing the SQUID into its finite-voltage state, is of the same magnitude as when they measure the noise using the more conventional method of dc-biasing a junction and measuring the resultant voltage fluctuations. Though it is not mentioned in the paper, we assume these measurements were performed at 4.2 K.

There have also been a number of experiments done measuring the $1/f$ noise of grain boundary junctions in high-T_c cuprates such as BSSCO and YBCO [37, 21, 14, 20]. These measurements are of less concern to our research, though they do lend further support to the supposition of a defect site that traps charge carriers, leading to critical-current fluctuations. They propose that an oxide layer forms between the two crystal orientations containing a high density of localized defect states. Of incidental interest is the result that their noise data is better explained by the presence of normal-resistance fluctuations in addition to the expected critical-current fluctuations. This is interesting from the standpoint that our junctions do not behave in the same fashion. As will be discussed in Chapter 8, a plot of the noise versus bias current at a constant temperature for our samples does track with the dynamic resistance, but it does not turn up and start increasing quadratically with the bias current. This gives us some clue as to the physical mechanism

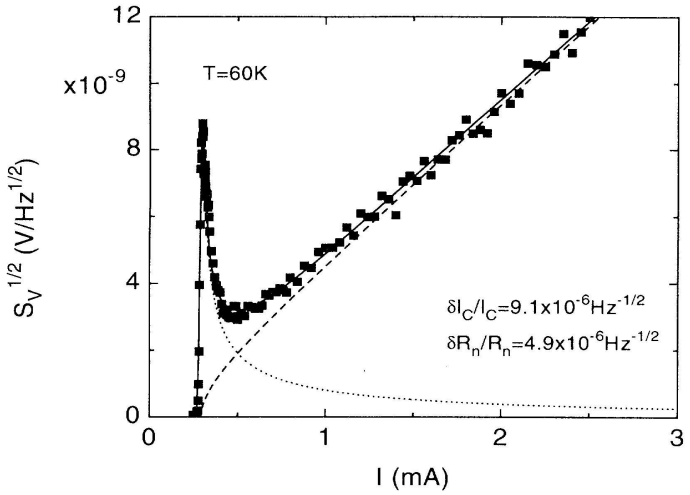

Figure 3.8 *Voltage noise versus bias current, as 63 Hz. The solid line is a least-squares fit based on the RSJ model assuming both critical-current and resistance fluctuations. The dotted/dashed line is calculated taking into account only critical-current/resistance fluctuations. From [37].*

responsible for the noise in our samples, or at least as to what the mechanism is not.

4 Qubits

This chapter covers what will turn out to be the underlying motivation behind the work done for this thesis. In the past decade there has been an explosion of interest in quantum information sciences such as quantum computation and cryptography. The basic goal of this nascent field, quantum computation and information, is the exploitation of the quantum-mechanical nature of systems to revolutionize the current paradigm of computing architecture and more generally the propagation of information, i.e. communication.

In quantum computation and information sciences, the fundamental component is the quantum bit (qubit). Our research focuses on the superconducting approach to making qubits (specifically flux qubits) which incorporate Josephson junctions as their primary constituent. This offers several advantages over qubit designs from other fields. Flux qubits are easy to control, readout, and couple to. Finally, they are readily scalable using standard lithographic techniques. This last point is something that is not true for many other qubit designs.

In addition, a good qubit must maintain long coherence times (i.e. the characteristic time it takes for a coherent linear superposition of the two qubit states to become ill-defined, or incoherent) so that the information encoded in the qubit remains distinguishable from noise. Numerous groups throughout the world currently use Josephson junctions as their qubit building block and are measuring coherence times for their particular qubits that are much less than expected based on theoretical work (see [34, 56, 45, 53] and ref-

erences therein, for example). Therefore there must be another, previously unaccounted-for, mechanism responsible for decohering qubits. We believe that low-frequency noise present in Josephson junctions possibly causes this premature decoherence. Understanding and eliminating this source of noise is critical to the successful implementation of superconducting qubits.

Currently there are three viable superconducting qubit designs: charge, flux, and phase. After discussing the general properties of two-state systems, the basic physics involved in each of the qubit designs will be outlined. Finally, we will examine how $1/f$ noise leads to dephasing in a qubit.

4.1 Two-State System

Qubits are an outgrowth of the more familiar bit. Historically, bits can have one of two values, 0 or 1. In contrast, qubits can be in a state other than 0 or 1. Standing for quantum bit, a qubit is a coherent linear superposition of the individual $|0\rangle$ and $|1\rangle$ states:

$$|\Psi\rangle = \alpha|0\rangle + \beta|1\rangle, \tag{4.1}$$

where naturally, the probability of finding the qubit in the $|0\rangle$ state is $|\alpha|^2$ and in the $|1\rangle$ state $|\beta|^2$, where we use the conventional normalization $|\alpha|^2+|\beta|^2 = 1$. Because of this condition and the unimportance of the overall phase of the state, we can write

$$|\Psi\rangle = \cos\frac{\theta}{2}|0\rangle + e^{i\varphi}\sin\frac{\theta}{2}|1\rangle. \tag{4.2}$$

Using this form, we can define what is known as the Bloch sphere, used for visualizing the state of a single qubit (see Fig. 4.1). Any point on the surface

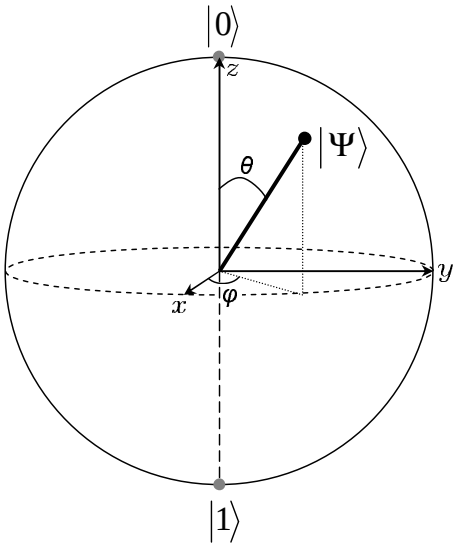

Figure 4.1 *Bloch-sphere representation of a qubit.*

of the Bloch sphere is a viable pure qubit state. Any operations on a qubit are simply a rotation of the state vector to another location on the sphere.

For now, we can consider the qubit in complete isolation from the environment. Given this condition, its motion is completely governed by a simple Hamiltonian

$$H_q = -\frac{1}{2}\hbar\Delta_0\sigma_x + \frac{1}{2}\epsilon\sigma_z, \tag{4.3}$$

where σ_i are the Pauli matrices and the basis is chosen such that the eigenstates of σ_z correspond to the system being localized in either the left or right well, as shown in Fig. 4.2(a). The value of ϵ determines the energy difference between the left and right states. The Hamiltonian given in Eq. (4.3) is equivalent to that of a spin $\frac{1}{2}$ particle in a magnetic field, such as would be found in an NMR experiment. The general nature of the dynamics of σ_z is sensitive to the ratio $\hbar\Delta_0/\epsilon$. If this ratio is small then the eigenstates of $\hat{H}$ are nearly indistinguishable from the eigenstates of σ_z and they are essentially localized to either the left or right well, as illustrated in Fig. 4.2(a).

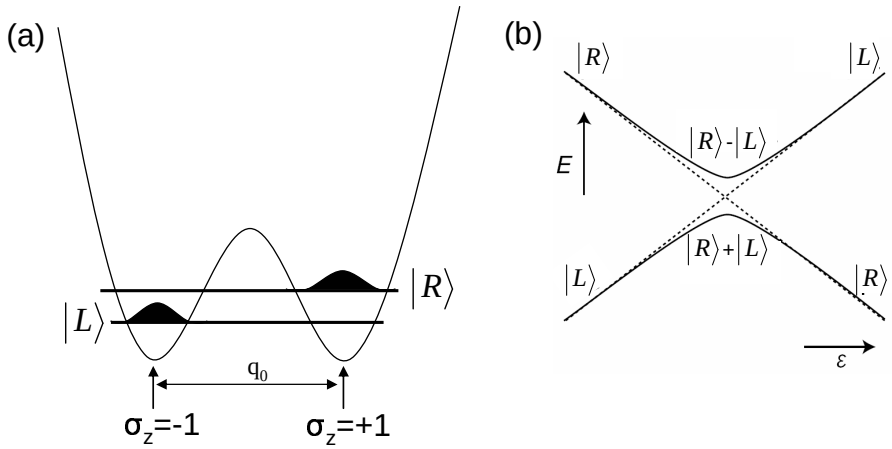

Figure 4.2 *(a) Double well potential showing the left and right localized states, offset for clarity. For the appropriate bias ($\epsilon = 0$) they are energetically degenerate. (b) Adapted from [11] – schematic showing the energy anticrossing indicative of a non-zero tunneling matrix. At the center $\epsilon = 0$ and the eigenstates are linear superpositions of the $|R\rangle$ and $|L\rangle$ states, while far from the degeneracy point the eigenstates are best approximated by the individual left and right states.*

However, if the ratio is large, the tunneling matrix element is significantly non-zero and the eigenstates spread across both wells. In the limiting case of $\epsilon = 0$ they are the familiar symmetric and antisymmetric combinations:

$$|\Psi_E\rangle = \frac{1}{\sqrt{2}}\left(|R\rangle + |L\rangle\right), \; |\Psi_0\rangle = \frac{1}{\sqrt{2}}\left(|R\rangle - |L\rangle\right), \tag{4.4}$$

where $|R\rangle$ and $|L\rangle$ correspond to the (normalized) ground states in the right or left well separately. The energy difference between these two states is $\hbar\Delta_0 \equiv E_E - E_0$. More generally, the energy difference between the states is the quadrature sum of the two energy scales

$$\Delta E = \sqrt{(\hbar\Delta_0)^2 + \epsilon^2}. \tag{4.5}$$

Provided $\hbar\Delta_0 \neq 0$ the dynamical behavior of σ_z displays an oscillatory nature. If $P(t)$ is defined as $P_R - P_L$, where $P_R(P_L)$ is the probability of

the system being found in the right(left) well state then, when we initialize the system such that $P(0) = +1$, the subsequent behavior is a sinusoidal "sloshing" of the wavefunction from right to left and back, repeatedly:

$$P(t) = \cos(\Delta_0 t). \tag{4.6}$$

It is this behavior, as characterized by the oscillatory nature of the amplitudes of the respective states, $|L\rangle$ and $|R\rangle$, that, having no analog in classical systems, forms the heart of a qubit.

If the system remains completely isolated from the environment, the Hamiltonian given by Eq. (4.3) remains a complete description and the resulting dynamics are easily calculable. However, in reality this is never the case. Every two-state system used as a qubit interacts with its environment, and, without exception, this interaction modifies the behavior of the system in question. The primary coupling mechanism to the environment is described by a term of the form $\sigma_z\hat{\Omega}$, where $\hat{\Omega}$ is some operator of the environment. This means that the environment is sensitive to the value of σ_z and vice versa. For reasons explained in [28], it is sufficient to constrain our focus only to environmental coupling to σ_z, ignoring the coupling of the environment to either σ_x or σ_y. Furthermore, following the arguments presented in [3], it is sufficient to represent the environment as a collection of harmonic oscillators that couple linearly to the qubit in their position and momenta coordinates. Thus, we get the spin-boson Hamiltonian, relayed in [28] as

$$\begin{aligned} H_{SB} &= -\frac{1}{2}\hbar\Delta\sigma_x + \frac{1}{2}\epsilon\sigma_z + \sum_\alpha \left(\frac{1}{2}m_\alpha\omega_\alpha x_\alpha^2 + p_\alpha^2/2m_\alpha\right) \\ &+ \frac{1}{2}q_0\sigma_z\sum_\alpha C_\alpha x_\alpha. \end{aligned} \tag{4.7}$$

Here, Δ is the tunneling matrix element, ϵ is the bias, x_α, p_α, m_α, and ω_α are the position, momentum, mass and frequency, respectively, of the αth harmonic oscillator of the environment, and q_0 represents the distance between the two potential minima (see Fig. 4.2(a)). C_α is the strength of the coupling of the qubit to an environmental oscillator, α.

While H_{SB} contains everything necessary to calculate the effect of an Ohmic environment (i.e. dissipative in a fashion analogous to the dissipation of power in a resistor) on a qubit, it helps our qualitative understanding of the situation to recast this interaction a little differently. As suggested in [28], the environment "observes" the qubit. One of the first things we learn about quantum mechanics is that an observation of a quantum mechanical system collapses the wave function. Therefore, this weakly coupled "observation" of the qubit by the environment leads to a collapse that extends over some length of time that depends on the strength of the coupling. The decay in amplitude of $P(t)$ is the result of this collapse.

As mentioned before, the time it takes for this decay to occur is much less than can be accounted for by the coupling of the qubit to the Ohmic environment. Thus we look to low-frequency $1/f$ noise as a likely cause of an additional noise term responsible for the premature decoherence of superconducting qubits.

4.2 Charge Qubit

One of the first superconducting examples of a functional qubit (i.e. coherent control and observation of quantum-state evolution in the time domain) was the Cooper-pair box design successfully implemented by Nakamura [42, 43, 46]. A single Cooper-pair box is composed of a small island, coupled to a

reservoir electrode via a Josephson junction, two gate electrodes capacitively coupled to the island, and an additional probe electrode connected via a highly resistive tunnel junction (see Fig. 4.3). The Hamiltonian for such a system is composed of the energy of individual Cooper pairs as well as the junction energy,

$$H = E_{CP}\,(N - N_g)^2 - E_J \cos\phi. \tag{4.8}$$

Here, $E_{CP} = (2e)^2/2C_\Sigma$ is the Coulomb energy of a Cooper pair on the island, where C_Σ is total capacitance of the Josephson junction plus the capacitance from the other electrodes. N is the total number of paired electrons on the island, and $N_G = C_G U/2e$ is the dimensionless dc-gate charge.

This system can be used as a two-state system to create a qubit with a two-state Hamiltonian identical in form to that of a spin-1/2 system. The same basis can be used, $|\uparrow\rangle \equiv |0\rangle$ and $|\downarrow\rangle \equiv |1\rangle$, resulting in an effective Hamiltonian

$$H = \frac{1}{2}\delta E(Q_t)\sigma_z - \frac{1}{2}E_J\sigma_x, \tag{4.9}$$

where $\delta E(Q_t) \equiv 4E_C(Q_t/e - 1)$ is the energy difference between the two charge states, and where E_C is the single-electron charging energy of the island and Q_t is the total charge on the island. As mentioned, this maps the quantum state evolution of the Cooper-pair box to the evolution of a spin-1/2 state in an effective magnetic field $\mathbf{B} \equiv (B_x, 0, B_z) = [E_J, 0, -\delta E(Q_t)]$. The qubit is controlled by biasing the gate electrode with a high-speed pulse, $V_p(t)$, to modulate Q_t non-adiabatically. Viewed in terms of the fictitious spin model, this amounts to changing abruptly B_z, after which the spin

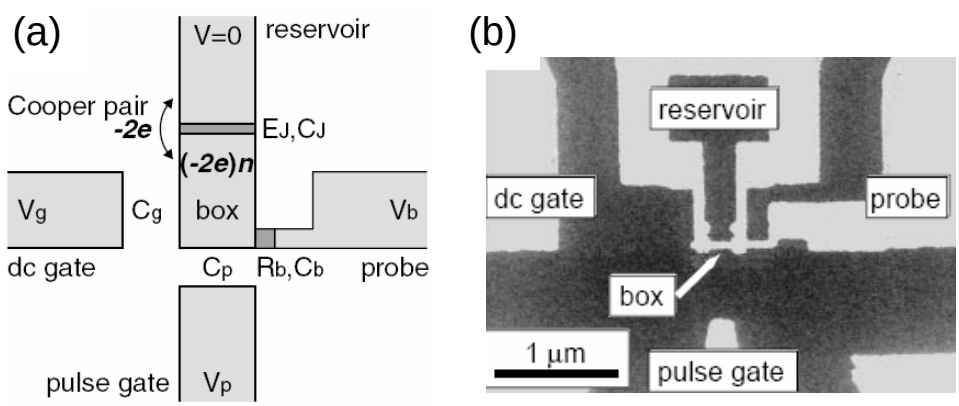

Figure 4.3 *(a) Schematic of a Cooper-pair box qubit. (b) SEM micrograph of a Cooper-Pair charge qubit. From [42, 43].*

precesses around the new field direction until B_z is switched back on with the termination of the pulse after time Δt. Thus, through the use of different length and strength pulses, the qubit's state vector, visualized with the Bloch sphere shown in Fig. 4.1, will move in whatever direction is desired. Using this methodology, the qubit can easily be switched between the two qubit states that differ in island-charge by an amount of one Cooper pair and in energy by $\Delta E(Q_0) = \sqrt{\delta E(Q_0)^2 + E_J^2}$, corresponding to the strength of the fictitious field.

Using this setup, Nakamura *et al.* were able to make several basic measurements, such as a free induction decay measurement (FID), which is essentially the type of measurement we use as the basis for the simulations we report on in Chapter 5. In an FID, the qubit is prepared in a superposition of the two basis states and allowed to freely evolve. The qubit state is then plotted as a function of the evolution time. Because the shortness of the resulting decay times was not adequately accounted for by coupling to a dissipative environment, they also performed spin-echo (see Appendix A and [15]) measurements meant to eliminate (or greatly reduce) the effect of $1/f$ noise in their measurement. This work conclusively showed that, indeed,

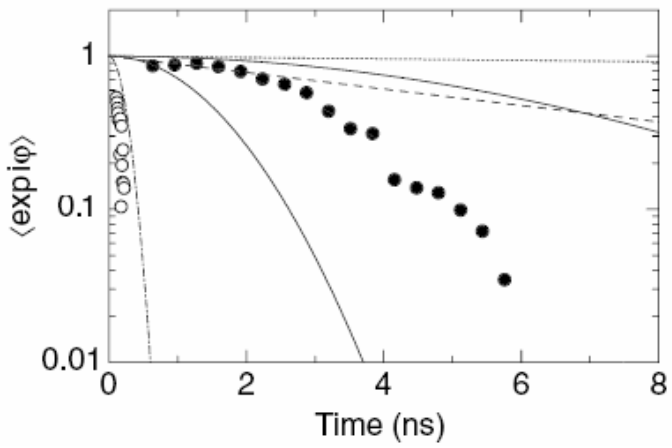

Figure 4.4 *The dotted line is a plot of the normalized amplitude of the decay signal when only an electromagnetic environment is present and responsible for decoherence of the qubit. Filled circles are the similarly normalized decay amplitudes measured using the spin-echo technique, while the open circles are the FID decay times measured without use of the spin-echo technique. The considerable effect of the spin-echo on decay times is immediately apparent. From [43].*

$1/f$ charge noise accounted for a considerable source of decoherence in their charge qubit. Figure 4.4 shows a very marked difference in the decay amplitude versus delay time between the two different methods used to make an FID measurement.

4.3 Flux Qubit

Several groups have chosen the flux qubit design for their superconducting qubit program. In its simplest form, a Josephson junction in a loop can be field-biased to a point at which there are two energetically degenerate states. This specific idea is most easily traced back to Leggett, with his suggestion of the use of an rf SQUID in the search for macroscopic quantum coherence [29, 27].

When appropriately field biased ($\frac{1}{2}\Phi_0$, where $\Phi_0 \equiv h/2e$ is the flux quantum), a spontaneous circulating current will be present in the superconduct-

ing loop, due to the constraints inherent to a multiply-connected junction. This current flows either to the left or to the right and can be found using Eqs. (2.23, 2.24). (See Section 2.2.2 for more about what happens when a magnetic field is applied to a loop, either with or without a junction.) In one case, the current will reinforce the field, bringing the integral of the phase around the loop to an integer multiple of 2π; in the other case the circulating current will subtract from the applied field, bringing the integral of the phase around the loop to zero. These two options are equally likely and are energetically degenerate.

Thus, by applying an appropriate external field, a two-well potential can be created using a multiply-connected Josephson junction in which the observable is a macroscopic quantity – the supercurrent around the loop, described by a single wavefunction. The Hamiltonian is composed of three terms: the Josephson energy, the magnetic energy, and the charging energy associated with any capacitance across the junction [36]

$$H = \frac{1}{2}\frac{Q^2}{C} - E_j \cos\phi + \frac{1}{2}LI_s^2. \tag{4.10}$$

Here I_S is the screening current around the loop, Q is the charge build-up at the junction, C is the capacitance of the junction, E_j is the Josephson energy from Eq. (2.14), and ϕ is the gauge-invariant phase across the junction from Eq. (2.15). Flux qubits are specifically designed such that $E_c = (1/2)(Q^2/C) \ll E_j$, allowing us to drop the first term of Eq. (4.10). The current around the loop can be expressed as the enclosed flux divided by the loop inductance, $I_s = \Phi_s/L = (\Phi_t - \Phi_x)/L$. This allows us to rewrite

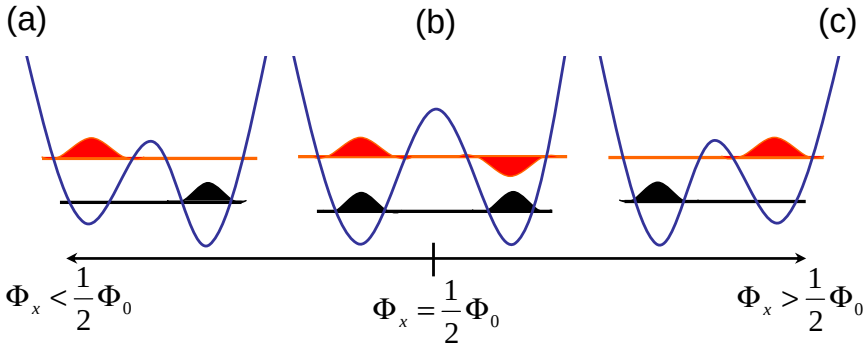

Figure 4.5 *(a) External field bias less than $1/2\Phi_0$ tips the double-well potential, creating a low-energy state in the right well. (b) External field bias equal to $1/2\Phi_0$ creates equal-depth wells, resulting in two energy levels that correspond to the symmetric and antisymmetric superpositions of the individual left and right states. (c) External field bias greater than $\Phi_0/2$ tips the double-well potential, creating a low energy state in the left well.*

the above equation as

$$U = -\frac{I_c \Phi_0}{2\pi}\cos\phi + \frac{1}{2L}\left(\Phi_x + \frac{\Phi_0}{2\pi}\phi\right)^2. \tag{4.11}$$

At the appropriate external-field bias ($\Phi_x = 1/2\Phi_0$) this is a symmetric double-well potential with minima corresponding to circulating currents in either the left or right direction. Changing the external bias will tilt the potential, preferentially selecting one well or the other, as shown in Fig. 4.5.

In addition to the qubit itself, a readout mechanism is necessary to determine the state of the qubit. For the flux qubit, this readout is achieved via a dc SQUID that encloses the qubit (see Fig. 4.6(b,c)). This SQUID can detect the flux that is enclosed by the qubit loop, determining which state the qubit is in, left or right circulating current. To make this measurement, the qubit is usually non-adiabatically biased to a point such that the degeneracy of the state is broken, trapping the qubit in whatever state it was in before the readout process began.

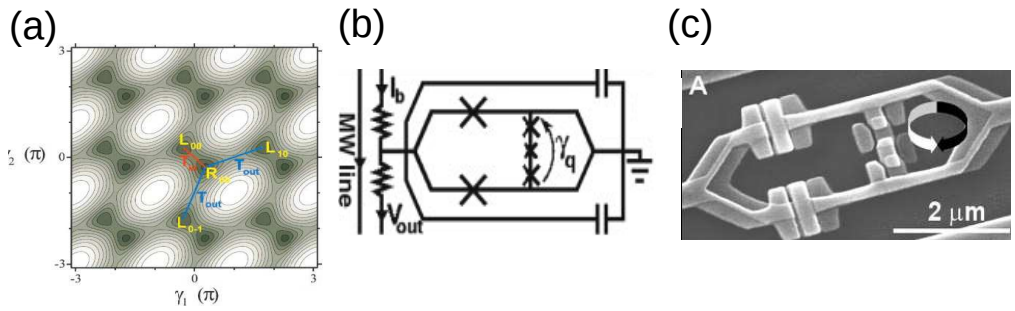

Figure 4.6 *(a) Qubit potential plotted as function of the two degrees of freedom, the gauge-invariant phase across each of the two similar junctions. There are two minima in each unit cell for the center cell indicated with L_{00} and R_{00}. Following the line from L_{00} to R_{00} results in a double-well potential, as does the route from R_{00} to L_{10} or L_{0-1}. (b) Schematic of a three junction qubit incorporated into a readout SQUID. (c) SEM micrograph of the device described in (b). Fabricated with double-angle evaporation, the overlapping regions form the junctions. From [39, 4].*

In order to maximize the decoupling from the environment while the qubit is in the degenerate configuration, a single junction in a loop is not the preferred design. Typical flux qubits incorporate three Josephson junctions, such as the Delft group uses [39, 55, 4]. In order to leave the dynamics fundamentally similar to a single-junction rf SQUID, they fabricate two of the junctions to have a different critical current from the third junction. Using this geometry, they actually create a three-dimensional double-well potential, where the x and y coordinates are the phases of the two different junctions and the z coordinate is the energy. The three-junction qubit is typically fabricated with two larger junctions and one smaller junction. The ratio of areas of one size of junction to the other is usually referred to as α and is a measure of the asymmetry between the two different types of junction. This parameter also determines the separation of the wells, or to put it another way, larger α leads to deeper wells (see [55, 4, 44] for more details).

As mentioned before, the inclusion of two more junctions does not appre-

ciably change the nature of the two-state system. As long as the slice of the two-dimensional potential taken goes through two minima, the resulting potential will be a double well. This can be controlled by using the appropriate biasing conditions which are determined when calibrating the system.

The addition of two junctions, however, does change the inductance of the loop, and that is their primary function. Given a Josephson junction, a Josephson inductance can be defined by combining the two Josephson equations from Eq. (2.16), giving

$$\frac{dI_s}{dt} = I_c \cos(\phi) \frac{2\pi}{\Phi_0} V. \tag{4.12}$$

With dI_s/dt proportional to V, this equation describes an inductor. This suggests that we define a Josephson inductance L_j by the conventional relationship $V = L(dI/dt)$, i.e.,

$$L_j = \frac{\Phi_0}{2\pi I_c \cos\phi}, \tag{4.13}$$

where, as usual, ϕ is the gauge-invariant phase of the junction. This is a non-linear inductance that modulates with the applied flux, allowing experimenters to use a smaller superconducting loop.

The small size is important because it helps to *decouple* inductively the qubit from the environment. However, if a simple rf SQUID were used with a small loop, it would be very hard to *couple* the qubit to the readout SQUID. With the addition of the non-linear Josephson inductance, the qubit couples strongly to the readout SQUID when the bias flux is set appropriately. Thus, by changing Φ_x the qubit can be tuned from a degenerate two-well system that is decoupled from the readout (Fig. 4.5(b)) due to a small L_j, to a tipped

double-well potential (Fig. 4.5(a,c)) that is strongly coupled to the SQUID (large L_j) for the purpose of state measurement. Further information about flux qubits can be found in, for example, [39, 55, 4, 11, 44].

4.4 Phase Qubit

The next superconducting qubit architecture to be covered is the phase qubit. The phase qubit is used by Martinis at NIST and Wellstood at Maryland and is based upon work done by Martinis while a graduate student working with Clarke at UC Berkeley [32, 33]. The phase qubit is simply a large-area Josephson junction fabricated and current biased so that there are a small number of bound states available to the phase particle trapped in the washboard potential described in Section 2.2.3.

In this scheme, a large-scale junction ($\sim 10 \times 10\ \mu\text{m}^2$) that incorporates single-shot capability with a relatively high measurement fidelity of 85% is used [35, 36, 50, 5, 26]. Below the critical current, a Josephson junction's phase is localized to a minimum of the potential given by [36],

$$H = \frac{1}{2C}Q^2 - E_j \cos\phi - \frac{I_b \Phi_0}{2\pi}\phi, \tag{4.14}$$

where I_b is the bias current. Furthermore, these junctions are designed to have a very small charging energy, which renders them insensitive to charge noise. The parameters Q and ϕ correspond to the charge and phase across the junction, respectively. Interpreted as quantum mechanical operators, they have the commutation relation $[\hat{\phi}, \hat{Q}] = 2ei$. This system will exhibit quantum-mechanical behavior, provided the bias current is sufficiently close to the critical current and $I_c\Phi_0/2\pi = E_j \gg E_c = e^2/2C$ [51].

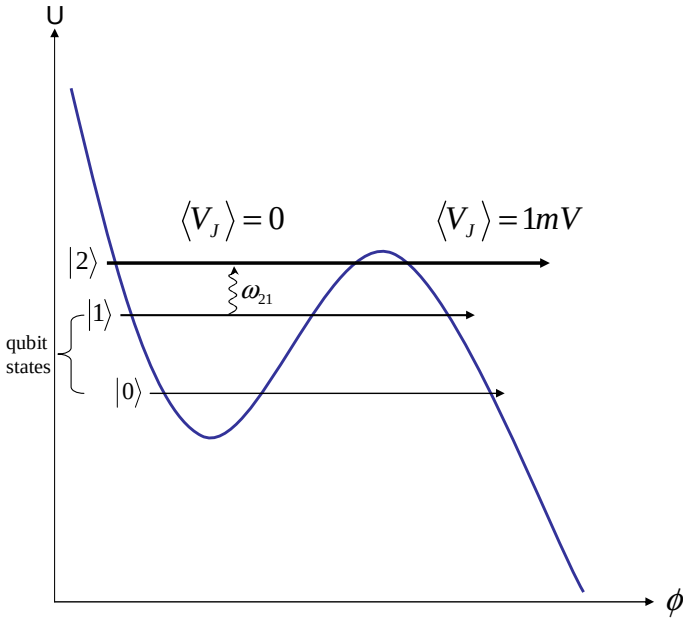

Figure 4.7 *Qubit potential U showing qubit states and measurement. Qubit operations are performed using the $|0\rangle$ and $|1\rangle$ states, but measurement occurs by tunneling from $|2\rangle$ into the finite voltage state. Adapted from [35].*

With zero dc voltage across the junction, the Josephson inductance and capacitance form an anharmonic LC-like resonator with a potential that is approximately cubic. This potential is characterized by the barrier height $\Delta U(I) \propto I_b^{3/2}/I_c^{1/2}$ and a (classical) plasma small-oscillation frequency at the bottom of the well, $\omega_p(I) \propto (I_b I_c)^{1/4}$ [35]. As the bias current is increased, the barrier height decreases to zero (see Fig. 2.8). For typical operation, there are on the order of $\Delta U/\hbar\omega \approx 3$ bound states residing in a local minimum. The two lowest quantized energy levels are used as the two qubit states.

All qubit operations are performed using the two lowest quantized energy states of the local minimum. When a state measurement is desired, resonant microwaves are applied to the junction in order to drive a $1 \rightarrow 2$ transition. This effectively determines the population probability of the first excited state, because if $|1\rangle$ were populated then the microwave pulse would drive it into $|2\rangle$, where it will promptly tunnel into the free-running, finite-voltage

state due to the large tunneling rate, Γ_2, where $\Gamma_{n+1}/\Gamma_n \sim 1000$ [35]. After tunneling, a voltage appears across the junction that is easily measurable with a standard preamplifier. Thus, the probability that the qubit was in $|1\rangle$, p_1, is equal to the probability of observing a voltage signal across the junction after applying the microwave pulse. Assuming the qubit has not decohered, the probability of the qubit being in $|0\rangle$ is simply $1-p_1$. It is worth noting that unlike the flux qubit, the phase qubit does not operate using two degenerate states. As long as the qubit state can be prepared in a linear superposition of the computational basis states that is then manipulable, however, it can be used as a qubit.

4.5 Quantronium Qubit

The final qubit architecture to be discussed has been dubbed a "quantronium" by its designers. In short, the quantronium is a fusion of the charge qubit Cooper-pair box with the superconducting loop and junction used in flux qubits. The motivation for this union of approaches is to render the resultant qubit insensitive to both charge and flux noise.

Similar to the charge qubit described in Section 4.2, the quantronium relies upon a Cooper-pair box with a Hamiltonian described by Eq. (4.8). In this case, $E_{CP} = (2e)^2/2(C_g + C_j)$, where C_j is the capacitance of the small Josephson junctions, while C_g is the capacitance of the gate electrode, as pictured in Fig. 4.8. The use of the Hamiltonian given by Eq. (4.8) is predicated upon the condition that the temperature and superconducting gap energy Δ satisfy the relation $k_B T \ll \Delta/\ln N$ and $E_{CP} \ll \Delta$ [59]. In contrast to the charge qubit, the quantronium qubit is designed such that $E_J \cong E_{CP}$.

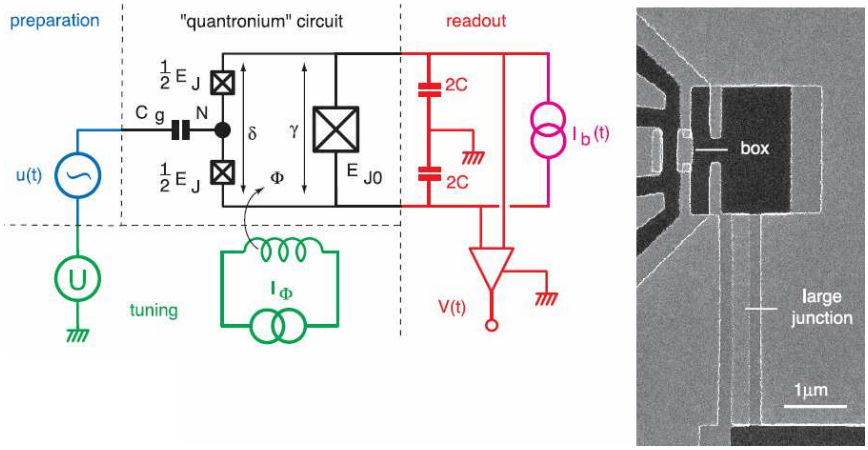

Figure 4.8 *Circuit diagram of the quantronium qubit plus the readout and preparation circuit components. The black dot represents the Cooper-pair box. The two small x-boxes are the small junctions that define the Cooper-pair box, and the large x-box is the large junction used for readout of the qubit state. Also pictured is an SEM image of a quantronium device fabricated using double-angle shadow evaporation. The overlapping areas are the Josephson junctions. From [59].*

Because the system is sufficiently nonharmonic, the ground and first excited states form a two-level system which, like many qubits, corresponds to a spin-1/2 system in an effective magnetic field. In this case, the Zeeman energy $h\nu_{01}$ is close to a minimum of E_J when $N_g = 1/2$. At this energy, the two qubit states (i.e. $|0\rangle$ and $|1\rangle$) have the same average charge $\langle N\rangle = 1/2$, effectively decoupling the system from first-order fluctuations of gate charge. Applying microwaves to the system ($u(t)$ in Fig. 4.8) with frequency $\nu \sim \nu_{01}$ allows the preparation of the generic quantum two-state wavefunction of Eq. (4.1), $|\Psi\rangle = \alpha|0\rangle + \beta|1\rangle$.

The difference between quantronium and the charge qubit lies in the readout and the fact that the Cooper-pair box lies within a superconducting loop. The single junction of a basic Cooper-pair box is split into two smaller junctions in order to achieve this. Figure 4.8 shows the qubit circuit, containing the Cooper-pair box surrounded by two smaller junctions. This series com-

bination of box and junctions is incorporated into a superconducting loop with another, much larger Josephson junction.

The Josephson energy in Eq. (4.8) becomes $E_J \cos \phi_j/2$, where ϕ_j, the phase drop across the series combination of two small junctions, is an additional degree of freedom. With this modification, the two qubit states are not discriminated between by the charge on the island, but through the supercurrent in the loop, $\langle I \rangle = (2e/\hbar)\langle H \rangle$. This is achieved by entangling the state vector with the phase across the large junction γ [59]. The various phases in the circuit are related by $\phi_j = \gamma + \phi_x$, where $\phi_x = 2e\Phi/\hbar$, in which Φ is the field-bias applied by the tuning portion of the circuit shown in Fig. 4.8.

The readout is accomplished by applying a current pulse, $I_b(t)$ that biases the parallel combination of the large junction and small junctions, bringing the large junction close to its critical current. Starting from $\phi_j \approx 0$, the phases γ and ϕ_j grow during the current pulse. Consequently, a supercurrent develops around the loop, adding to the bias current in the large junction. If the current through the large junction increases enough, it will switch into the finite-voltage state. If the qubit is in the excited state, $|1\rangle$, the probability of the large junction switching p_1 is high, whereas if the qubit is in the ground state, the probability p_0 for the large junction to switch is low. By careful calibration, the experimenters were able to achieve a maximum fidelity, $\eta \equiv p_1 - p_0$, of about 0.95 [59].

4.6 Decoherence Mechanism in Qubits for Low-Frequency Noise

For a qubit that has been initialized and then allowed to evolve, the subsequent state depends on how long it is allowed to evolve and the tunneling rate between the degenerate states of the qubit between which the qubit oscillates. To determine the expectation value of the qubit for a given evolution time, many measurements of the qubit state are made with that specific delay between the qubit initialization and measurement.

Interesting dephasing effects can be introduced by a changing tunneling-rate. Even in the absence of all other forms of intrinsic dephasing or decoherence, a repeated change in the tunneling frequency with each individual qubit state measurement leads to a phase noise that enters the measurement only in the limit of large N, where N is the number of single-shot qubit state measurements.

This is the effect of low-frequency noise on superconducting qubits. Such devices are vulnerable to two primary sources of $1/f$ noise: flux vortex hopping between pinning sites in superconducting films, and critical-current fluctuations in the constituent Josephson junctions, both illustrated in Fig. 4.9. Hopping of flux vortices between pinning sites acts like an effective change in the external field bias. For a qubit that has been initialized by carefully balancing the double potential well, vortex hopping leads to a breaking of the degeneracy by tipping the potential well (see Fig. 4.10(c)). In turn, this leads to a change in the tunneling frequency. However, this is only a second-order change, and because this change can be further minimized by fabricating devices with superconducting leads measuring less than $(\Phi_0/B)^{1/2}$, where $\Phi_0 \equiv h/2e$ is the flux quantum, and B is the applied field, we may ignore

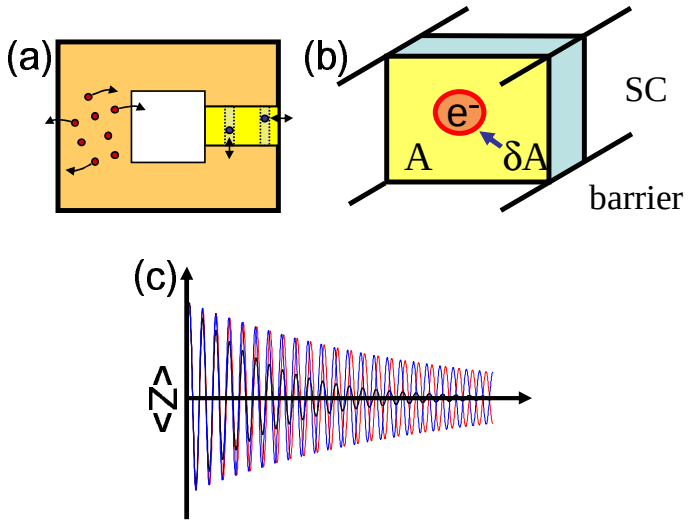

Figure 4.9 *Effects of low-frequency flux and critical-current fluctuations in a superconducting qubit. (a) Flux modulation from vortices hopping into and out of a loop, and critical-current modulation from electrons e^- temporarily trapped at defect sites in the junction barrier. (b) A single-charge trap blocks tunneling over an area ΔA, reducing the critical-current. (c) Fluctuations modify the oscillation frequency, inducing phase noise which leads to decoherence in time-averaged ensembles of sequential measurements of the qubit observable Z.*

$1/f$ noise due to flux hopping and concentrate on critical-current fluctuations.

Critical-current fluctuations are a more serious problem, if only because there is no known way to eliminate them from Josephson junctions, although there are techniques designed to mitigate their effect on qubits (see Appendix A on the spin-echo technique, for example). In our picture of $1/f$ noise, a charge hops into the amorphous oxide barrier of the junction. This charge, through Coulomb repulsion, effectively blocks a conduction channel in the junction. This effectively changes the area A of the junction by some amount ΔA (see Fig. 4.9(b)). When the area of a junction changes, its critical current changes as well, leading to a change in the tunneling frequency of $\Delta\Omega \sim \exp \Delta I_c$ (see Fig. 4.10(d)).

This charge hopping can be seen more simply as two-state fluctuators

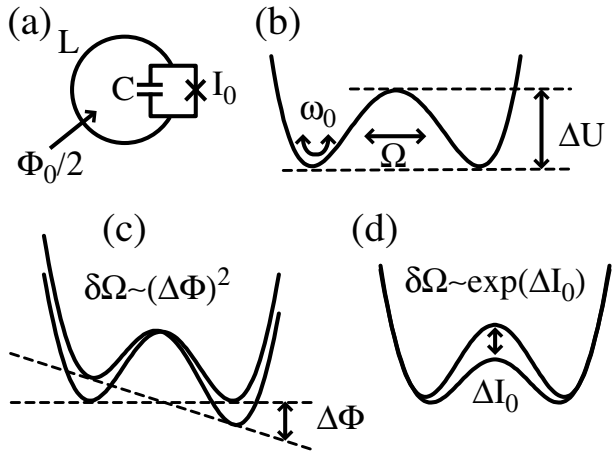

Figure 4.10 *One-junction flux qubit. (a) Schematic. (b)Symmetric double-well potential for flux bias $\Phi_x = \Phi_0/2$. (c) Flux fluctuation $\Delta\Phi$ couples to Ω only in second order. (d) Critical-current fluctuations, ΔI_0, produce and exponential change in Ω.*

present in the junction. Each fluctuator is characterized by its lifetime in the untrapped state τ_u, and its lifetime in the trapped state τ_t. This produces a Lorentzian in the noise power spectrum of the junction with an effective time of $\tau_{\rm eff} = (1/\tau_u + 1/\tau_t)^{-1}$. The dynamics of such fluctuators have been extensively studied [47, 48, 63]; for a review see Chapter 3. For the case in which the junction area is very small, it is possible to see single fluctuators [64]; however, in most cases there will be multiple fluctuators. Their individual Lorentzians combine to form a noise power spectrum that is $1/f$-like. Given the presence of $1/f$ critical-current noise in qubits incorporating Josephson junctions, an effective decoherence can arise. This is due to the fluctuation of the tunneling frequency of the qubit during the period of time over which data are acquired. In effect, the measurement, with this source of phase noise, averages several sine waves of different frequencies, as in Fig. 4.9(c).

For a given qubit, we assume an energy-level separation of $\hbar\Omega$, the magnitude of which depends on the critical current of the constituent Josephson junctions. We describe the sensitivity of a given qubit to a change in the

energy-level splitting due to critical-current noise by the dimensionless parameter

$$\Lambda \equiv \left| \frac{I_0}{\Omega} \frac{d\Omega}{dI_0} \right|. \tag{4.15}$$

This is the differential change in the tunneling frequency $d\Omega$, for a corresponding change in critical current dI_0, normalized by the ratio of the critical current to tunneling frequency.

The value of Λ depends largely on qubit architecture, device parameters, and the bias point. A larger Λ indicates that a given qubit is affected more strongly by critical-current noise, whereas smaller Λ qubits are more resistant to such noise. Ideally, qubits and the measurement architecture designed for qubit manipulation and readout would be designed to minimize Λ.

Looking back at the descriptions of the individual qubits, it is clear how each architecture is vulnerable to $1/f$ critical-current noise. Every design depends on a potential barrier, a tunneling barrier, the height of which determines the critical current. In essence, the accurate and repeatable measurement of all characteristic qubit times, such as the Rabi oscillation frequency, Ramsey fringes, T_1, and T_2 depend on a steady value of this tunneling barrier. Not only do measurements of these times depend on the noise properties of the critical current, but any attempts to control the qubit do as well. When experimenters attempt to manipulate the qubit state, they must apply some control such as microwaves or a dc gate voltage for a specific amount of time. This time is entirely dependent on the tunneling rate between states, and if the tunneling rate changes with time, the dynamics are unarguably altered.

If the noise associated with the critical current is white then how one measures or controls qubits does not matter. But, as we shall see, when

the noise shows a spectral density with some frequency dependence, the results depend very much on the measurement technique. This dependence is explored in the next chapter.

5 1/f Noise Simulations

As a part of this project, we simulated the effect of low-frequency critical-current noise fluctuations on the dephasing times of qubits in the absence of other sources of decoherence, such as coupling to a dissipative, Ohmic environment. This chapter covers the details of those simulations and helps to clarify the motivation behind this project.

5.1 Determination of Dephasing Times

Low frequency critical-current noise creates phase noise which enters the measurement of the qubit state by virtue of the fact that an accurate measure of the qubit-state probability distribution as a function of time requires several thousand single-shot samplings of the qubit state each of which see a different tunneling rate. In general, a qubit measurement consists of preparing the qubit in a degenerate state, allowing the qubit to evolve for a period of time, either under the influence of control microwaves (as in a Rabi oscillation measurement) or freely, and finally measuring the qubit with a pulse that drives the qubit out of the degeneracy on a time scale short in comparison to $\Omega \equiv E_{10}/\hbar$.

For the purposes of this work, we will focus on the ideal case in which the qubit is allowed to evolve freely after the initial state preparation. Following the initialization, the qubit is allowed to evolve for some time t_D, after which the measurement is performed. This sequence is followed in order to mea-

sure the dephasing time τ_ϕ. However, in reality, a measurement of τ_ϕ would require a much more complex qubit control and measurement process, such as a Ramsey fringe experiment. Nonetheless, it is important to note that the presence of $1/f$ critical-current fluctuations will affect such measurements as well, and that therefore we feel the simplified approach used in our simulations will accurately reflect the dependence of τ_ϕ on the presence of phase noise.

For our simulation we normalize the qubit states to either $+1$ or -1, and we always start the qubit in the $+1$ state before pulsing the qubit to the degeneracy point, in which the likelihood of measuring the qubit in either state is equal. In a dissipative environment containing the usual sources of noise responsible for qubit decoherence (such as coupling to an Ohmic environment), the subsequent quantum oscillations of the average of a generalized observable $\langle Z(t)\rangle$ follow the form

$$\langle Z(t)\rangle = e^{-t/\tau_0}\cos\Omega t, \tag{5.1}$$

where Ω is the tunneling frequency between the two states of the qubit, and τ_0 is the decoherence time set by the coupling to the environment. What was found in Van Harlingen *et al.* [57] is that the presence of critical-current fluctuations provides an additional decoherence mechanism and leads to a different functional form for the decay of $\langle Z(t)\rangle$.

5.2 Noise Generation

Van Harlingen *et al.* [57] estimated the critical-current noise for a Josephson junction with a particular area A, and critical current I_c, at 4.2 K using the

empirical formula

$$S_{I_c}(f,T) \approx \left[144\frac{(I_c/\mu\,\mathrm{A})^2}{(A/\mu\,\mathrm{m}^2)}\left(\frac{T}{4.2\mathrm{K}}\right)^2(\mathrm{pA})^2\right]\frac{1}{f}. \tag{5.2}$$

This expression for the noise was arrived at by surveying approximately ten different groups' reported $1/f$ noise for the types of junctions they were using [57]. In general, the noise was measured at 4.2 K. We simulated the noise for an Al shadow mask junction measuring 100 nm on a side and having a critical current of 1 μA at a temperature of 100 mK. This gives $S_{I_c}(1\text{ Hz}) = 8.16 \times 10^{-24}$ A^2/Hz. We can extrapolate over the range of frequencies of interest to us to arrive at a noise spectrum that obeys a $1/f$ dependence. Furthermore, we better approximated real noise by randomizing the phase and amplitude of each point of the noise spectrum. To randomize the phase, we multiplied each point by $\exp(i\theta)$, where $0 < \theta < 2\pi$ is a random number chosen from uniform distribution. The amplitude was similarly randomized by the inclusion of a multiplicative factor chosen from an exponential distribution with a mean of one. After the noise spectrum is generated, we take the real part of the Fourier transform of the spectrum to obtain the critical-current noise as a function of time.

In Fig. 5.1, the time trace and spectrum of simulated $1/f$ noise is shown for $N = 10^4$, where we use N to signify the total number of single-shot qubit measurements. For the purposes of our simulation, we assume each noise point is separated in time by t_z =1 ms. This value of t_z sets an upper boundary of 1 kHz for the bandwidth of the noise that affects our simulations. This does not imply that in reality there are no fluctuations with a characteristic frequency higher than 1 kHz, but merely that we do not sample fast enough for those higher frequency components to contribute to the phase

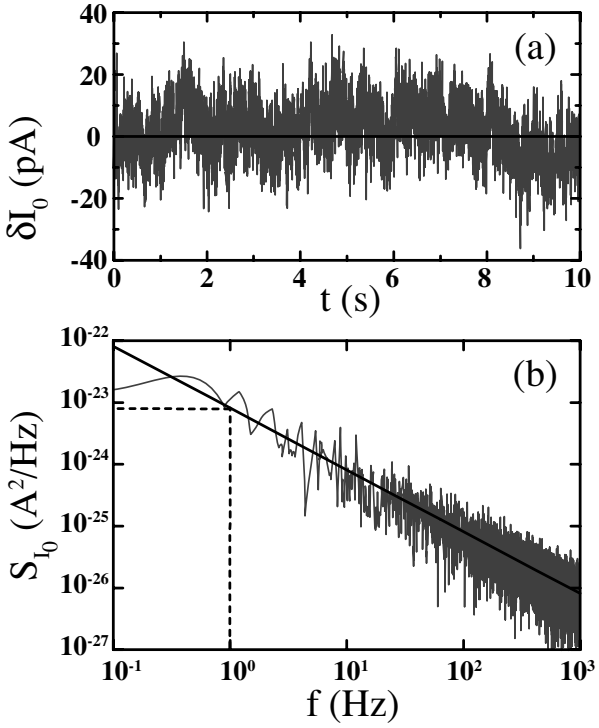

Figure 5.1 *(a) Time trace of simulated* $1/f$ *noise. (b) Corresponding spectrum showing a clear* $1/f$ *dependence.*

noise. Given Nt_z =10 s, we know the lower bound of the bandwidth of the noise that affects the measurements.

In performing these simulations, we are not only interested in noise with a $1/f$ power spectrum. We also consider noise sources that range in frequency dependence from white noise (no dependence on frequency) to brown noise ($1/f^2$ dependence on frequency). In order to compare the effects of noise having different frequency dependencies, it is necessary to normalize the different spectra. By including an appropriate normalization factor in our generation of a given noise spectrum, we can ensure that the integral of the spectrum over the appropriate bandwidth will be the same for each noise spectrum we generate, be it $1/f$, white, or something else.

5.3 Different Sampling Methods

To measure Rabi oscillations, Ramsey fringes or any other characteristic times of a qubit, the state of the qubit will be sampled a total of N times. Each sampling includes initialization of the qubit and time delay t_D between the initialization and the measurement. What occurs during this delay time depends on the measurement being made. For example, in a Rabi oscillation measurement the qubit is driven from state to state by microwaves, whereas for a free induction decay measurement the qubit is simply allowed to evolve without any other active involvement. This period is followed by the measurement and, lastly, some period time to allow the qubit to thermalize before re-initialization. We perform this simulation assuming the entire sampling process takes on the order of 1 ms. We refer to this time as t_z, and it sets the upper bound on the bandwidth of relevant frequencies. This is the same t_z by which our simulated noise points are separated. However, it is entirely possible to run the experiment faster, to decrease t_z. Just how fast a particular measurement sequence can be carried out depends on the amount of time it takes for the qubit to thermalize completely before re-initialization. If the qubit is not allowed to thermalize sufficiently, high-energy quasiparticles created during the measurement process will still be present and may lead to the further decoherence of the qubit in successive measurements.

If a Rabi oscillation is to be mapped out, several data points per period are necessary in order to resolve the sinusoidal nature of the qubit oscillation. For a signal of frequency f, the sampling frequency should be at least $2f$. Each of these data points on the oscillation curve will be separated by a uniform amount of time, t_d, such that if the third point of the oscillation curve is desired, $t_D = 3t_d$. This will result in a curve mapped out by several

hundred different points, each at a different t_D, extending far enough out that the decay time of the oscillation curve can be accurately measured. We use N_t to denote the total number of points used to define any such measured curve.

A single sampling of the qubit at each of the N_t points of the desired curve will not suffice to determine accurately the expectation value of the qubit for a given t_D. Instead, an ensemble of measurements is required. The number of qubit samplings made and averaged for each point of the curve is N_z.

The typical way to measure the expectation value of the qubit $\langle Z \rangle$, for a given t_D after the qubit initialization, is to make N_z measurements of the qubit each corresponding to the same value of t_D and then average the results. After making those N_z measurements, we increase t_D by t_d and make another N_z measurements. We repeat this process N_t times and get the desired curve. We will refer to this time-delay averaging method of qubit measurement as Method A (see Fig. 5.2(a)). Due to the grouping of the qubit samplings, only higher-frequency fluctuations are averaged over, because all of the qubit state measurements for a particular delay time are acquired during a time interval $N_z t_d$, rather than over the entire experiment. For Method A, the expectation value of the qubit observable $\langle Z \rangle$, after time $t_D = m t_d$, with $1 \leq m \leq N_t$, is given by

$$\begin{aligned} \langle Z^A(t_D) \rangle &= \frac{1}{N_Z} \sum_{n=1}^{N_Z} \cos \left\{ \left[\Omega + \frac{d\Omega}{dI_0} \delta I_0 \left(t_A \right) \right] t_D \right\} e^{-\frac{t_D}{\tau_\phi^0}} \\ &= \frac{1}{N_Z} \sum_{n=1}^{N_Z} \cos \left\{ \Omega \left[1 + \Lambda \delta i_0 \left(t_A \right) \right] t_D \right\} e^{-\frac{t_D}{\tau_\phi^0}}, \end{aligned} \tag{5.3}$$

where $t_A = [(m-1)\,N_Z + n]\,t_Z$. In effect, any fluctuations that occur on a time-scale larger than $N_z t_z$ will not be averaged out.

However, there is another way to make an effective measurement of a given property of the qubit. The alternative, Method B, entails a sampling process similar to that of Method A, except that the order in which the measurements are taken is different. This process begins as Method A does: measure the qubit once for a given t_D ($t_D = 0$, for example). For the next sampling of the qubit, we increase the amount of time we allow the qubit to evolve from $t_D = 0$ to $t_D = t_d$. This is in contrast to Method A, wherein the qubit state would be measured N_z times using $t_D = 0$ before changing the delay time to $t_D = t_d$. To continue with Method B, the third qubit sampling would be for $t_D = 2t_d$ (see Fig. 5.2(b)).

After N_z samplings of the qubit in this fashion, $t_D = (N_z - 1)t_d$. The very next qubit measurement would occur at $t_D = 0$. Therefore, for Method B the expectation value after $t_D = mt_d$ is

$$\begin{aligned} \langle Z^B(t_D)\rangle &= \frac{1}{N_Z}\sum_{n=1}^{N_Z}\cos\left\{\left[\Omega + \frac{d\Omega}{dI_0}\delta I_0\left(t_B\right)\right]t_D\right\}e^{-\frac{t_D}{\tau_\phi^0}} \\ &= \frac{1}{N_Z}\sum_{n=1}^{N_Z}\cos\left\{\Omega\left[1+\Lambda\delta i_0\left(t_B\right)\right]t_D\right\}e^{-\frac{t_D}{\tau_\phi^0}}, \end{aligned} \tag{5.4}$$

where $t_B = [(n-1)\,N_t + m]\,t_Z$. Here, τ_ϕ^0 is the dephasing time set by decoherence processes other than $1/f$ fluctuations, such as dissipative processes in the qubit and the environment. Using Method B allows the experimenter to average effectively over both high- and low-frequency noise fluctuations, because the qubit state measurement for a given time delay runs over the time of the entire experiment, Nt_d. Because of this, the number of decades

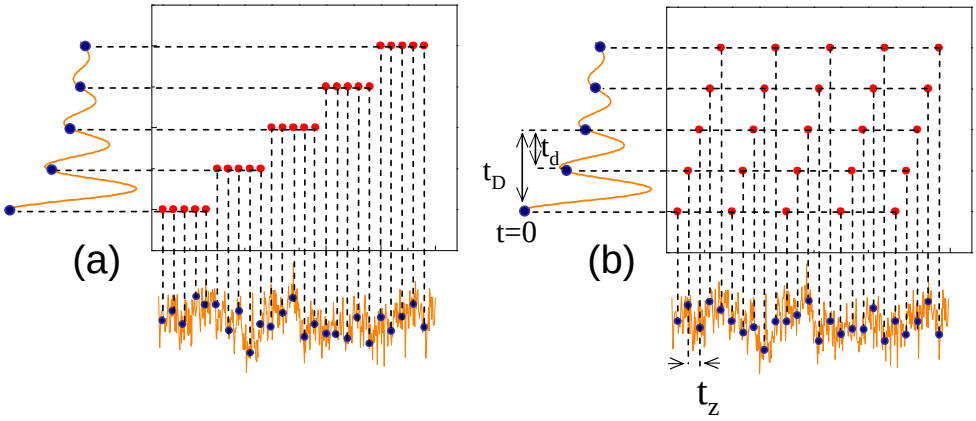

Figure 5.2 *(a) Method A utilizes a point averaging method to determine the expectation value of the qubit for a given t_D. This averages out higher frequency noise fluctuations only. (b) Method B utilizes a sweep averaging method to determine the expectation value of the qubit for a given t_D. This method averages both high and low frequency contributions to the critical current noise.*

of noise that affect the dynamics of the qubit is larger for Method B ($\ln N$) than for Method A ($\ln N_z$). See Fig. 5.2 for graphical representations of the different sampling methods.

The effect of using the two differing methods is most easily seen by simulating a free induction decay curve for a qubit with a single junction having standard aluminum shadow mask junction parameters ($A = 0.01$ μm^2, $I_C = 1$ μA, $\Omega/2\pi = 1$ GHz, $T = 100$ mK, $\Lambda = 100$) but substantially increased critical-current noise at 1 Hz: $S_i^{I_0}(1\text{ Hz}) = 1.4 \times 10^{-20}$ A^2/Hz.

Inserting noise with a $1/f$ spectrum, generated in the fashion described in Section 5.2, with $N = 10^6$, into Eqs. (5.3, 5.4) will result in a qubit oscillation curve that decays due to the presence of phase noise (Fig. 5.3).

It is apparent from Fig. 5.3 that although Method A produces a slightly longer dephasing time, as calculated by our fit, Method B is obviously a better measurement of the evolution of the state of the qubit as a function of delay time, t_D. For this simulation we used twenty points per oscillation of $\langle Z \rangle$, such that $N_t = 200$ for ten oscillations.

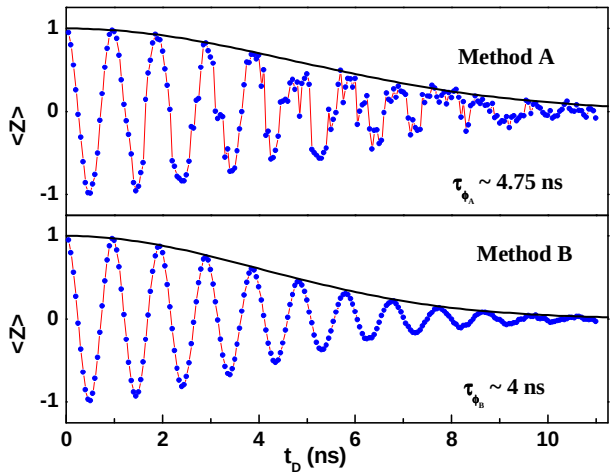

Figure 5.3 *The dephasing time for Method A is greater than for Method B; however, it is clear that Method B results in a much cleaner curve.*

If we use the same junction parameters but change the noise power at 1 Hz to the value given by the universal noise factor in Eq. (5.2), $S_i^{I_c}(1\text{ Hz})= 8.16 \times 10^{-24}$ A^2/Hz, we will get a more realistic picture of the decay curve. In this instance $N = 3 \times 10^6$, and $N_t = 1000$ (see Fig. 5.4). In this case, we sampled the qubit oscillations at $(1+\phi)\Omega/2\pi = 2.618$ GHz, where $\phi = (1+\sqrt{5})/2 \approx 1.618$ is the Golden Mean, so that $t_z = 0.382$ ns. The simulation results are independent of this choice of the sampling frequency. The envelope function is determined by convolving the averaged probability amplitude with the Gaussian filter kernel,

$$K(t) = \left(\frac{1}{2\pi\sigma^2}\right)^{1/2} \exp\left(-t^2/2\sigma^2\right), \tag{5.5}$$

where σ is chosen to be the sampling period t_z.

This decay envelope fits a Gaussian decay of the form

$$\langle Z_{env}\rangle \sim \exp\left(-t^2/2\tau_\phi^2\right), \tag{5.6}$$

where t_ϕ is the characteristic dephasing time. This form is due to the fre-

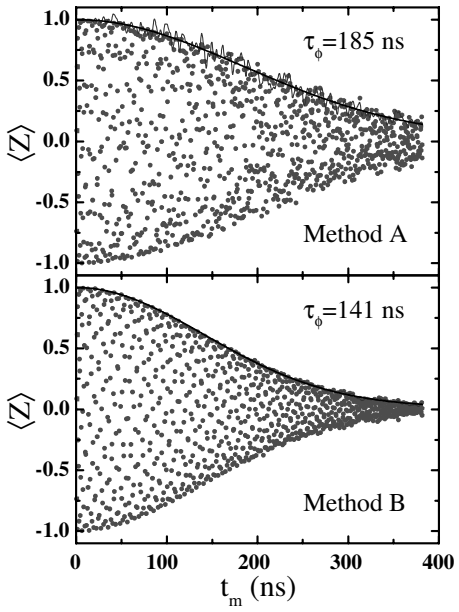

Figure 5.4 *Probability envelopes determined by simulations using measurement methods A and B for a qubit with* $I_0 = 1\ \mu A$, $S_{I_0}(1\ Hz) = 8.16 \times 10^{-24}\ A^2/Hz$, $A = 0.01\ \mu m^2$, $\Lambda = 100$, *and* $\Omega/2\pi = 1\ GHz$. *The structure visible in the Method B plot arises from periodic sampling of the oscillations and is evidence of the increased effective averaging relative to Method A.*

quency modulation of the qubit due to the phase noise introduced by the low-frequency, critical-current noise. This is in contrast to the exponential decay that is expected and seen in the case in which the dominant form of dephasing is dissipative coupling to an Ohmic environment. For long decay times, the decay envelope does not vanish, but instead decays to a steady-state noise floor that is present due to uniform randomization of the oscillation phase by the critical-current fluctuations. This noise floor is $Z_{noise} \approx N_Z^{-1/2}$ for both Methods A and B. For large N_z, this floor is negligible in determining the dephasing time, τ_ϕ. However, for smaller N, taking this noise floor into account is necessary to extract accurately a value for the dephasing time. We do this by fitting the decay envelope of the probability amplitudes to the quadrature sum of the noise floor term and the Gaussian decay term of

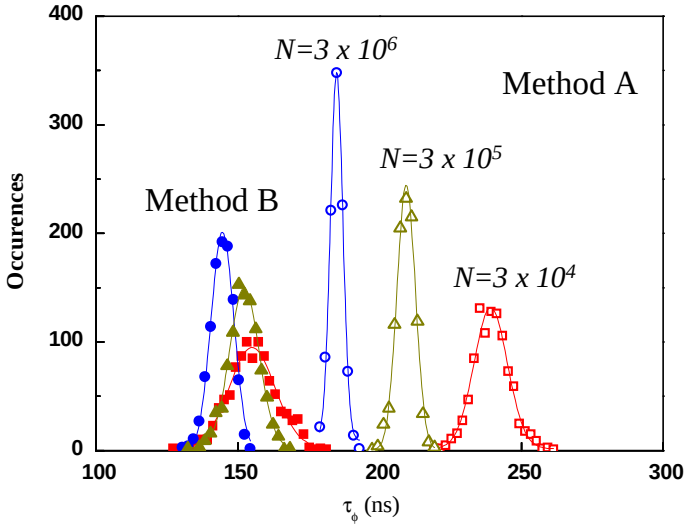

Figure 5.5 *Distributions of dephasing times, τ_ϕ, calculated by Method A (open symbols) and Method B (closed symbols) for different numbers of qubit state measurements: $N = 3 \times 10^4$ (squares), $N = 3 \times 10^5$ (triangles), $N = 3 \times 10^6$ (circles). Each distribution includes* 1000 *simulations of the coherent oscillations accumulated into bins of width 2 ns. Qubit parameters are as in Fig. 5.4.*

Eq. (5.6):

$$\langle Z_{env} \rangle = \sqrt{(Z_{noise})^2 + \left[\exp\left(-t^2/2\tau_\phi^2\right)\right]^2}. \tag{5.7}$$

The dependence of τ_ϕ on the number of measurements, which sets the range of $1/f$ noise that is effective in dephasing the qubit, can be found by carrying out the simulations for different measurement parameters, N_t and N_z, as shown in Fig. 5.5. We repeat the simulation 1000 times per different value of N to acquire statistical information about the distribution of dephasing times for the given N.

Based upon the statistics shown in the histogram, we can give a measure of the dephasing time for each of the two methods, assuming a $1/f$ spectrum. Using the empirical formula for S_{I_c} given by Eq. (5.2), and setting $N = 10^6$,

we find

$$\tau_\phi^A(\mu s) \approx 20A^{1/2}(\mu m)/\Lambda(\Omega/2\pi)(GHz)T(K) \tag{5.8}$$

for Method A and

$$\tau_\phi^A(\mu s) \approx 15A^{1/2}(\mu m)/\Lambda(\Omega/2\pi)(GHz)T(K) \tag{5.9}$$

for Method B.

5.4 Using Spectral Composition as a Diagnostic

Van Harlingen *et al.* [57] showed that measured decoherence times depend on which method is used to sample the qubit state. This difference between Methods A and B can be used as a diagnostic for determining the nature of the dominant noise in a superconducting flux qubit. If the dominant noise present in a qubit is white in spectral composition, then the sampling method should not matter.

The reason for this is straightforward. Because Methods A and B differ in how they group the measurements, they effectively average over different frequency regimes. But for white noise, the power of the noise is independent of where in the spectrum one samples, and thus the effect of the noise is independent of the method used.

For a superconducting flux qubit that predominantly exhibits $1/f$ noise, the use of Method A to sample the qubit will result in longer dephasing times. Because Method A effectively averages only the higher (lower power)

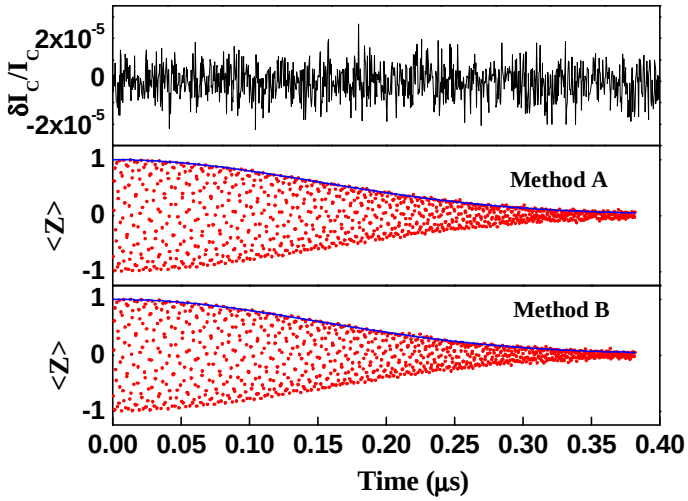

Figure 5.6 *From top to bottom: time trace of white noise* $(1/f^0)$*; decoherence envelope calculated using Method A; decoherence envelope calculated using Method B. For white noise, there is no difference between Methods A and B.*

frequency fluctuators, the lower frequency (higher power) fluctuators dominate, resulting in a qubit curve that is markedly less "coherent" than when using Method B, and thus the decay is less readily seen. To put it another way, the tunneling rate that is determined by the critical current, changes less frequently, when using Method A, but more dramatically, so the use of Method A averages less. Method B averages both high and low frequency fluctuators evenly, so neither the higher-power, low-frequency noise nor the lower-power higher-frequency noise dominates. This results in a curve that is considerably cleaner, due to the increased averaging. This is evident in Fig. 5.7.

Continuing in the vein of $1/f$ noise, qubit dephasing dominated by brown noise, (i.e. $1/f^2$), will show shorter times for Method B than for Method A. Because brown noise is dominated heavily by its low-frequency components, a beat-like phenomena can occur. This is due to the fact that, when sampling the qubit, one effectively only accesses a few different frequencies. The fewer

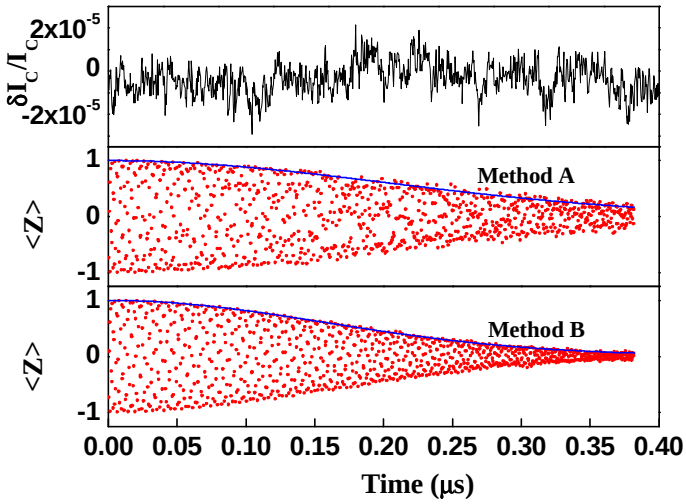

Figure 5.7 *From top to bottom: time trace of pink noise* $(1/f^1)$*; decoherence envelope calculated using Method A; decoherence envelope calculated using Method B. Times are shorter using Method B.*

frequencies one accesses, the more apparent the beat pattern is. In Fig. 5.8, the pattern seen in the Method B box is caused by averaging only two or three high power fluctuators.

It is not necessary for the brown noise to be caused by fluctuators in a junction. Indeed, it is more likely that a noise spectrum that goes as $1/f^2$ is due to instrument drift. However, the effect of instrument drift is fundamentally similar, in that it will lead to variations in the apparent tunneling frequency of the qubit.

It is also possible in extremely small junctions to find that the noise is caused entirely by a single fluctuator. If this is the case, the beat pattern hinted at when dealing with brown noise becomes obvious. If the tunneling frequency switches between two possible values, the effect is to average two sine waves, which results in a beat pattern (Fig. 5.9).

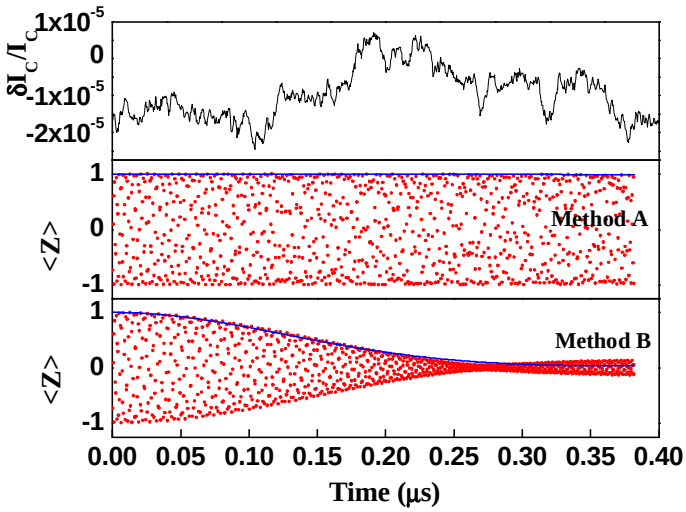

Figure 5.8 *From top to bottom: time trace of brown noise* $(1/f^2)$*; decoherence envelope calculated using Method A; decoherence envelope calculated using Method B. Times are shorter using Method B.*

In general, sampling a qubit using the two different methods (A and B) will result in two different dephasing times. The more imbalanced the noise power at high and low frequencies, the more apparent this difference will be. We can take the generic case where we generate noise with a $1/f^{\alpha}$ spectrum and vary α from 0 to 2 in order to plot the dependence of the ratio of the dephasing times versus the exponent α, of the noise (Fig. 5.10). The difference in dephasing times depends on the method used, and, in particular, the ratio of times can be used as a diagnostic of the noise environment the qubit is in. If the dephasing times from Method A and Method B are consistently the same then it is obvious that the qubit's dominant dissipative processes are white in nature (e.g. thermal fluctuations). But if the ratio of the measured dephasing time obtained using Method A to the dephasing time obtained using Method B is not unity, then the qubit dephasing is due to some process such as $1/f$ noise in the Josephson junctions.

The value of τ_{ϕ} as a function of N can also be used as a tool to diagnose the spectral composition of the dominant noise present in the qubit. In general,

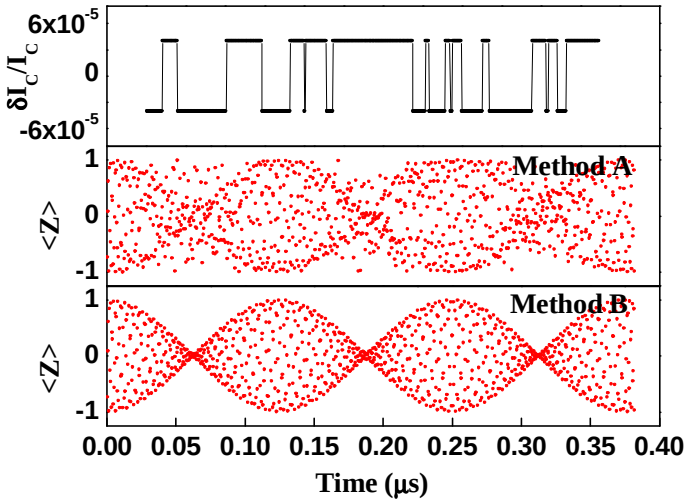

Figure 5.9 *From top to bottom: time trace of random telegraph noise caused by a single fluctuator; decoherence envelope calculated using Method A; deco-*

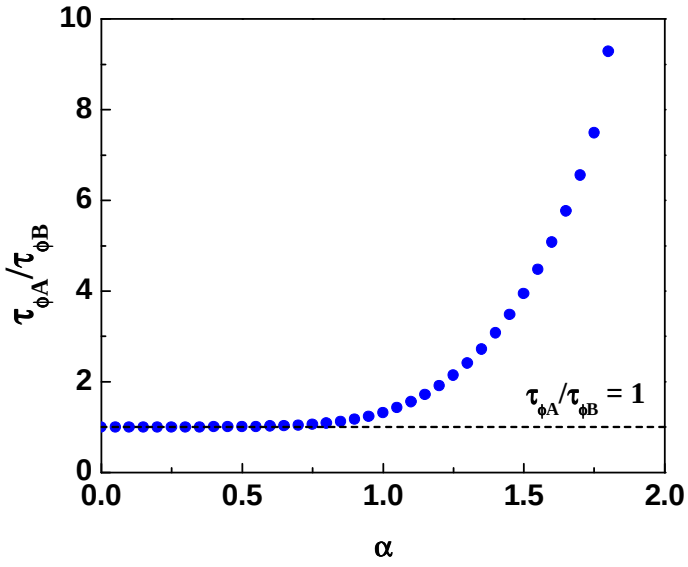

Figure 5.10 *Ratio of dephasing times using Method A over dephasing times using Method B versus the exponent of the spectral composition of the noise for $N = 1 \times 10^6$. That is, we plot $\tau_{\phi_A}/\tau_{\phi_B}$ vs. α, where the spectrum of noise is $1/f^\alpha$. For $\alpha = 1$, $\tau_{\phi_A}/\tau_{\phi_A} \sim 1.32$.*

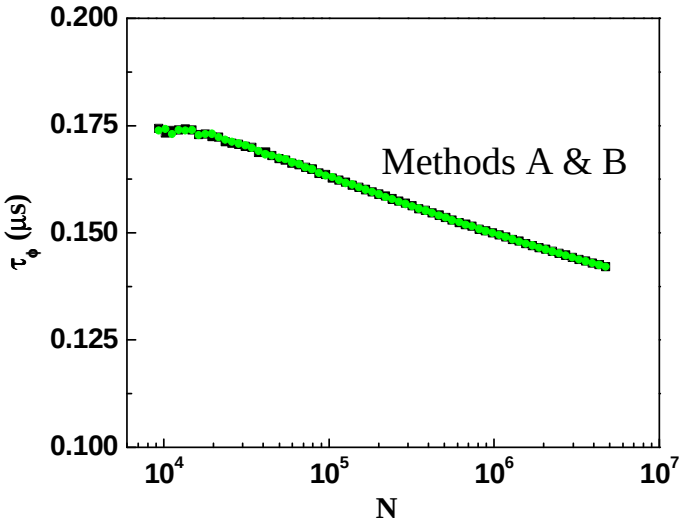

Figure 5.11 *Variation of the dephasing time, τ_ϕ, with the number of qubit state measurements, N, for Methods A and B in the presence of white critical-current noise. Each point corresponds to the mean value of τ_ϕ from 50 simulations of the oscillation decay envelope composed of $N_t = 1000$ points. Qubit and noise parameters as in Fig. 5.4.*

to get an accurate measure of the dephasing time of a qubit as a function of the number of measurements made, an ensemble of such measurements must be made for each value of N. We can then plot the mean of the measured dephasing times as a function of N. As one would expect, for the case of white noise in which the measured dephasing times are independent of the sampling method, we find that there is also a weak, power-law, dependence on N that is identical for Methods A and B (Fig. 5.11).

This same procedure can be followed for the case in which the dominant noise is $1/f$ or $1/f^2$ as well. In the former case, we see that the dephasing times for Method A are consistently longer by about 30%, as compared with the times measured using Method B. Furthermore, using the analytical form obtained by Martinis *et al.* [34],

$$\tau_\phi^M \equiv \left[\frac{1}{\ln(0.4N)}\right]^{1/2} \frac{1}{\Lambda(\Omega/2\pi)} \left[\frac{I_0^2}{S_{I_0}(1Hz)}\right]^{1/2}, \tag{5.10}$$

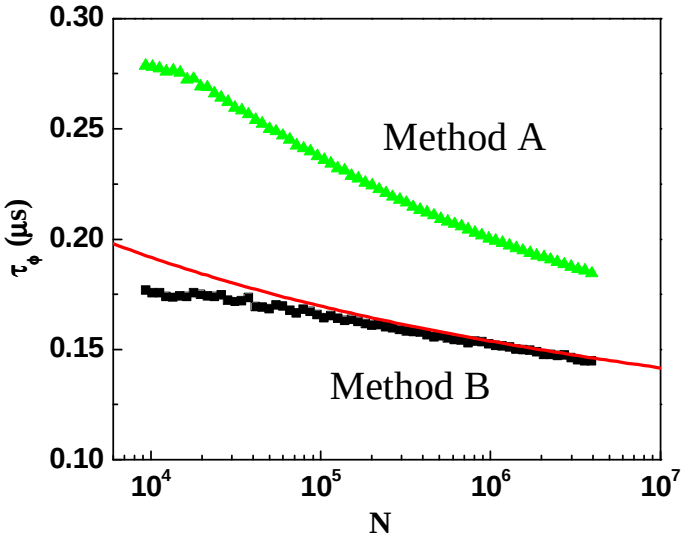

Figure 5.12 *Variation of the dephasing time, τ_ϕ, with the number of qubit state measurements, N, for Methods A and B in the presence of $1/f$ critical-current noise. Each point corresponds to the mean value of τ_ϕ from 50 simulations of the oscillation decay envelope composed of $N_t = 1000$ points. Qubit and noise parameters as in Fig. 5.4. The solid line is τ_ϕ^M from Martinis' analytical expression, Eq. (5.10).*

we can see that for the case of large N our simulated dephasing times calculated using Method B and Martinis' results are very similar, both in form and value (Fig. 5.12).

Finally, we can examine the behavior of the dependence of τ_ϕ on N for the case of predominantly "brown" noise ($1/f^2$). For this case, the noise is dominated by a few high-power, low-frequency fluctuators. Using Method A, these fluctuators do not affect the qubit state measurement. However, they substantially affect measurements made using Method B, resulting in times considerably shorter than the dephasing times calculated using Method A. The ratio of times depends largely on the value of N used in the simulations (Fig. 5.13).

In the limit of small N_z, Methods A and B give identical results. By reducing N_z, the effective number of fluctuators is reduced and limited to the high-power, low-frequency ones. This substantially decreases the averaging

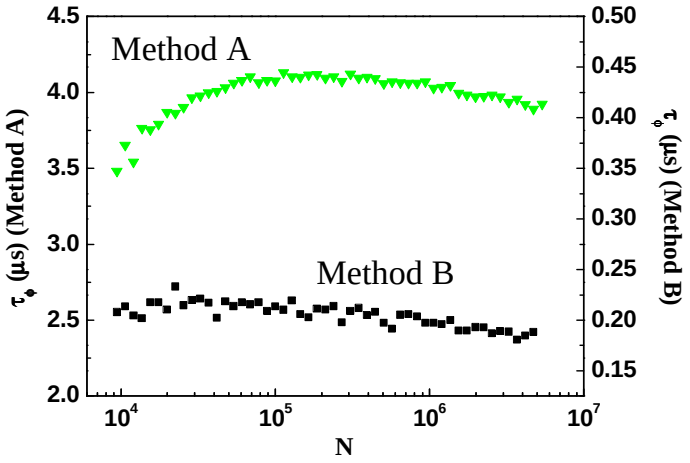

Figure 5.13 *Variation of the dephasing time, τ_ϕ, with the number of qubit state measurements, N, for Methods A and B in the presence of $1/f^2$ critical-current noise. Each point corresponds to the mean value of τ_ϕ from 50 simulations of the oscillation decay envelope composed of $N_t = 1000$ points. Qubit and noise parameters as in Fig. 5.4.*

performed and can lead to artificially low dephasing times. Given this, we can account for the downturn evident in the curves shown in Figs. 5.12 and 5.13 at low N. This is especially apparent in Fig. 5.13, in which the noise is $1/f^2$, and thus is even more strongly weighted towards the low frequencies. For the results pictured in Fig. 5.11, where the noise is independent of frequency, there is still some flattening of the Method A and B curves for low N_z, and we believe this is caused by the low amount of averaging present when N_z is small.

6 Sample Fabrication

This chapter describes both the samples ideal for this work as well as the actual samples used in this work, which for various reasons are not ideal. Josephson junctions can be fabricated in a variety of ways. For the purpose of this experiment, Josephson junctions fabricated in a fashion similar to the junctions used by those making measurements of dephasing times with superconducting qubits are ideal. But in some cases, the data was taken on junctions that were easier to fabricate, and thus more readily available.

To summarize, a Josephson junction is generically a device in which two superconductors are connected via a "weak link." This weak link can be a normal metal, an insulator, a geometrical constriction, etc. The key to successful fabrication of Josephson junctions is in controlling the characteristics of the weak link.

6.1 Ideal Sample

The purpose of this work is to characterize the $1/f$ noise as a function of temperature because we are concerned that this type of noise leads to a source of qubit decoherence in addition to that caused by an Ohmic environment. Therefore, the ideal sample, as mentioned above, would be identical to the types of junctions used for superconducting qubits. This would, we hope, give us the most insight into the mechanisms of decoherence and their possible solutions for the systems in which $1/f$ noise is a significant cause of

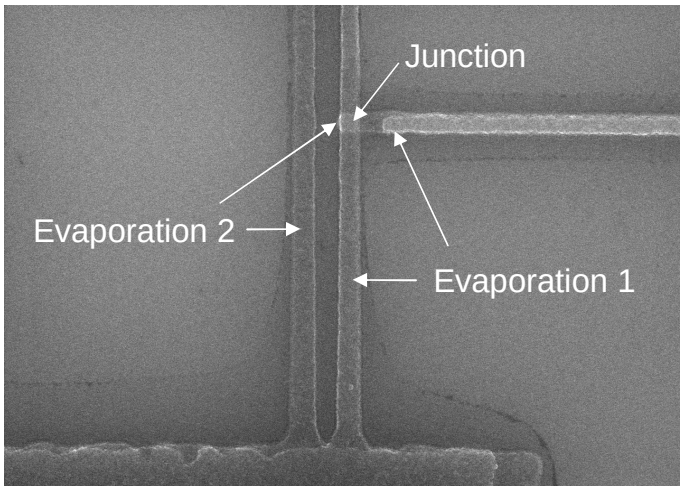

Figure 6.1 *SEM micrograph of an Al-AlO_x-Al junction fabricated by Madalina Colci using the double-angle evaporation technique. The overlapping regions of the vertical part of evaporation 1 with the horizontal part of evaporation 2 define the Josephson junction area: in this case approximately 200nm square.*

decoherence.

Groups working on the flux qubit generally use Al-AlO_x-Al Josephson junctions. The AlO_x insulating barrier suppresses the wavefunction describing the superconducting state in the Al and leads to the Josephson effect between the two Al superconducting leads. The junction is made using the standard shadow evaporation technique, in which aluminum is evaporated at one angle, oxidized, and then more aluminum is evaporated at another angle, resulting in a sandwich layering of Al-AlO_x-Al that is connected to Al leads.

The characteristics of these junctions that are important for the experiment are essentially two-fold. In order to use Josephson junctions in flux qubits, the size must be small enough that the Josephson energy ($\hbar I_c/2e$) is greater than the charging energy associated with the capacitance of the junction. The size restriction is relevant in determining the effect of $1/f$ noise on the rate of decoherence of a qubit incorporating a Josephson junc-

tion. As mentioned in Section 5.2 and explored more fully in Chapter 5, the noise spectral density, S_{I_c}, is inversely proportional to the area. Therefore, we would ideally measure the noise in junctions that are similar in size to those junctions being used in qubits. It should also be easier to measure the noise in smaller junctions, because the fractional change in area due to a single blocking site in the junction is higher for smaller junctions, resulting in larger critical current fluctuations.

Unfortunately, this type of junction is difficult to fabricate, requiring electron-beam lithography and considerable calibration of the evaporation system in order to get the two angles just right. As of yet, the Van Harlingen group has been unsuccessful in fabricating appropriately shunted junctions using this method. There are, however, other sources of junctions for measurement.

6.2 Samples from other groups

An alternate solution to the problem of acquiring ideal junctions is to get them from another group that has already perfected a fabrication process. This opens up several new avenues, as there are a number of groups doing research in superconducting qubits. The most likely candidates for our purposes are the groups of John Martinis at UC Santa Barbara, John Clarke at UC Berkeley, and Ray Simmonds at NIST.

Indeed, we already got several samples from Martinis while he was still at NIST. The junctions are approximately 10 μm on a side and would, at first glance, seem to be well suited to our experiment, as they are production junctions being used in their phase-qubit design. Unfortunately, the junctions we received from Martinis exhibited very strange resonances at different bias

levels [50, 5]. The cause for these resonances is still open to speculation, but suggested reasons include two-level systems that happen to be resonant with the applied control microwave pulses. Because this phenomenon possibly speaks to the very issue we are researching, Ray Simmonds and Kevin Osborn decided to design and fabricate samples specifically for us. The junctions they supplied range in size from 6.25 μm^2 to 100 μm^2. They are Al trilayer junctions, fabricated in much the same way as our Nb trilayer junctions are fabricated (see Sec. 6.3 below). Each sample has ten non-hysteretic junctions on it. There are normal-metal cooling fins attached to the shunt resistor of one the two junctions for a given size. The purpose of the fins is to help reduce the effect of hot electrons [68] in the shunt resistor. See Fig. 6.2 for example data showing the spurious resonators and a schematic of a junction made by Osborn.

The other group from whom we have received junctions is Clarke's. We have received two samples from them, to date. But the problem in this case is common to all junctions that are on the order of a hundred nanometers square: they are exceedingly easy to blow-out. When this occurs, a length of aluminum (or the junction itself) vaporizes when the current through the line spikes. This can occur when wiring the junction to a probe or when switching leads or turning the current supply on or off. Any situation in which static charge build-up and subsequent discharge through the junction is possible or likely will probably lead to the destruction of the junction because the small lines simply cannot dissipate enough heat. This is a problem that would have to be dealt with even were we to make our own small size-scale junctions, as another member of Van Harlingen's group (Madalina Colci) is doing.

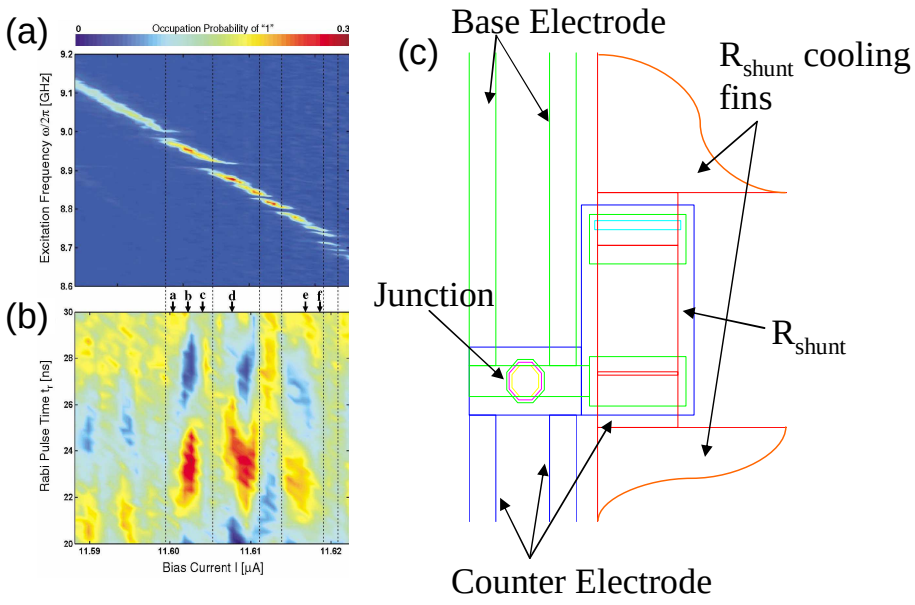

Figure 6.2 *Data and sample schematic from Simmonds and Osborn respectively. (a) Occupation probability of the first excited state for the Martinis/Simmonds [50] phase qubit versus microwave excitation frequency and bias current. Dotted lines indicate spurious resonators. (b) Measured occupation probability of the* $|1\rangle$ *state versus Rabi-pulse duration and bias current. (c) Schematic showing the geometry of the junctions we received from the NIST group and made by Osborn. Red corresponds to the shunt, green to the base electrode, and blue to the counter electrode.*

6.3 Homemade Samples

In our group we have the most experience making Nb-Al-AlO_x-Nb trilayer junctions due to the considerable amount of work done with scanning SQUID microscopy. Until recently, all of the SQUIDs used for this purpose were made by the graduate student running the SSM (scanning SQUID microscope). The obvious choice for making our own samples for measurement of $1/f$ noise would be to use this trilayer process, which is already developed and known to work. The junctions made this way are restricted in size to be no less than a couple microns square, but what they lack in terms of smallness is more than made up for in durability and relative ease of fabrication.

The junctions we make are commonly referred to as Nb trilayer junctions. They are labeled thus because the functional part of the junction, the tunneling barrier, is sandwiched between two layers of niobium. This trilayer structure is deposited in a single deposition cycle in our group's high vacuum sputter deposition chamber. The chamber includes an Ar ion mill, Nb and Al dc sputter guns, and an SiO_2 rf sputter gun. The standard process for trilayer fabrication begins by sputtering Nb first (about 50 nm), adding a layer of Al (10 nm), oxidizing the Al in 4 Torr of O_2 for 45 minutes, and then finishing by depositing a final layer of Nb (about 50 nm). The oxidization of the Al does not extend throughout the entire depth of the Al, thus the actual structure produced is Nb-Al-AlO_x-Nb, from bottom to top. Typical sputtering pressure for trilayer deposition is 10 mTorr of Ar, which is maintained by continuously pumping on the chamber while Ar flows into the chamber at a rate of 90 standard cubic centimeters per minute.

The next step in the fabrication process is to define the junction window. As it currently stands, after the trilayer deposition there is basically one huge

junction: two superconductors separated by a tunneling barrier. However, we want to define the junctions to be a specific size. In our case, the junctions we make range in size from 3 μm square to 10 μm square. Using standard photolithographic techniques, we define the junction area and reactively ion etch away the top layer of Nb in a localized region immediately adjacent to the junction window. The third step is to backfill with approximately 200 nm of SiO_2 into the regions from which Nb has been removed. This allows us to deposit the counter electrode of the junction, another layer of Nb (about 200 nm thick).

The final step in the fabrication is to deposit shunt resistors for the junctions. The shunt resistors are important, because without them the junctions would be hysteretic or underdamped (see Section 2.2.3 on the RSJ model of Josephson junctions). The shunts deposited for these junctions are an alloy of Cu and Au, in the ratio of 5 : 1 by weight. In order to create the alloy we thermally evaporate the Cu and Au in the same evaporation boat resulting in a layer of CuAu that ranges in thickness from about 200 nm to 300 nm. This evaporation is preceded by a very short evaporation of Cr, (10Å) onto the substrate in order ensure adequate adhesion of the Cu/Au alloy to the Si substrate.

Below are a number of diagrams illustrating the fabrication process. Between each step is a photolithographic step that defines the region to be affected by the subsequent deposition or etch step.

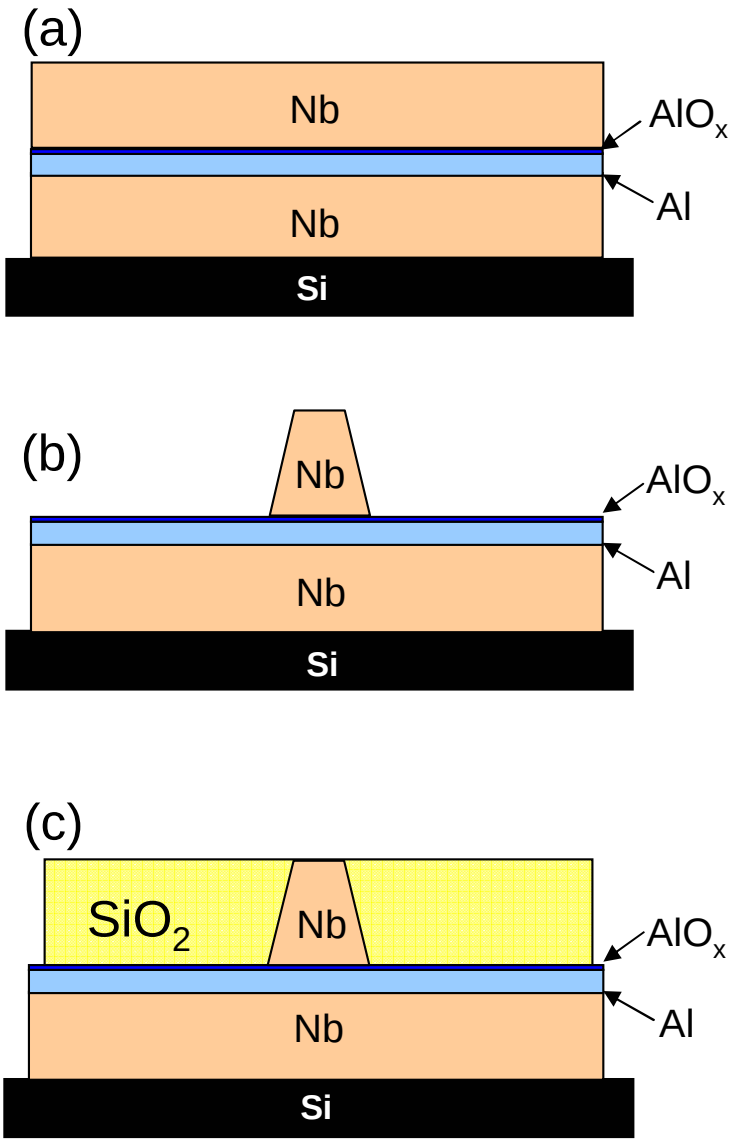

Figure 6.3 *(a) Step 1 of the Nb trilayer junction fabrication process. In this step, Nb trilayer is deposited, creating the S-I-S structure necessary for our junctions. (b) Step 2: In this step the junction window is defined by photolithography, and the top layer of the trilayer surrounding the junction window is reactively ion etched away. (c) Step 3: The void left after reactively ion etching the top layer of Nb is backfilled with the insulating barrier SiO_2.*

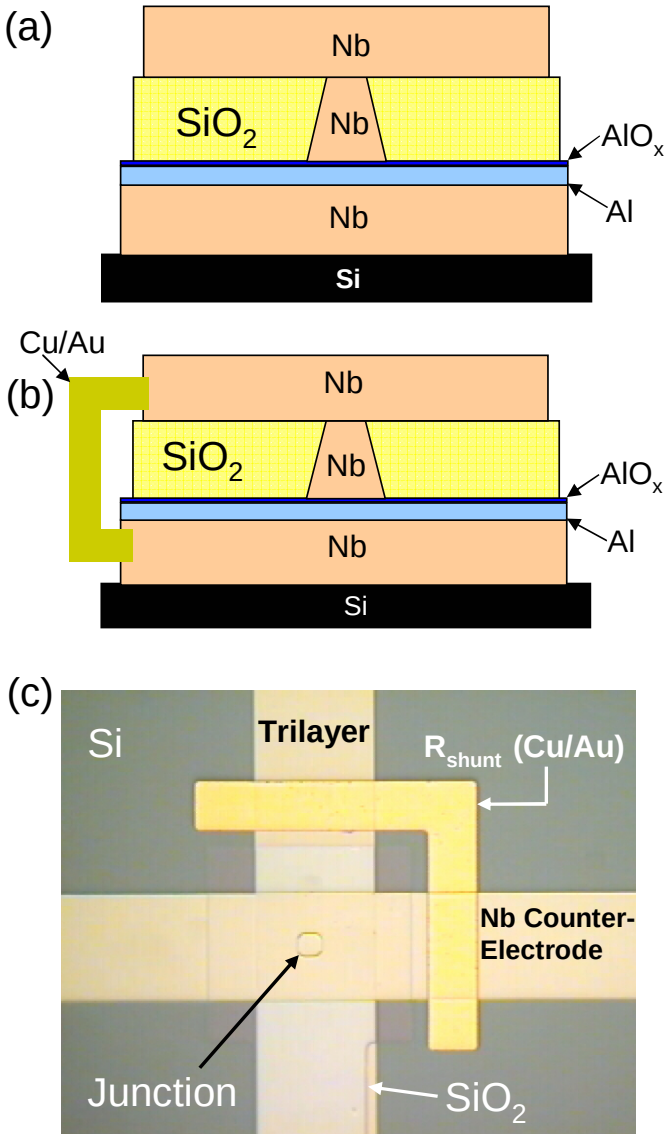

Figure 6.4 *(a) Step 4: Nb is deposited on top of the SiO_2 and junction window, creating the counter electrode. (b) Step 5: Finally, the Cu/Au shunt resistor is evaporated onto the sample, creating a resistive shunt between the bottom layer of the Nb trilayer and the Nb counter electrode. (c) Final product: This is a picture of a 7 μm square junction taken at 80x magnification. Each component in the fabrication process is clearly visible: the trilayer, junction window, SiO_2, counter electrode, and resistive shunt.*

7 Experimental Setup

7.1 Dilution Refrigerator

The purpose of this experiment is to determine the behavior and magnitude of the $1/f$ noise present in Josephson junctions as a function of temperature. In particular, we want to know how the noise behaves at the temperatures at which Josephson junctions are used in qubits. In order to minimize decoherence due to thermal noise, all present superconducting qubit experiments are performed in dilution refrigerators that can reach temperatures as low as 10 mK. Therefore, we need to measure the noise behavior of our samples at temperatures as low as 10 mK and ranging up to 1 K or more. In order to accomplish this, we used a commercial dilution refrigerator purchased from Oxford Instruments in the spring of 2001. The dilution refrigerator dewar is housed in an electromagnetically screened room and supported by an air-sprung vibration isolation frame (see Fig. 7.1).

Our refrigerator is the Kelvinox TLM (**T**op **L**oading into the **M**ixture). It has over 250 μW of cooling power at 100 mK. The TLM in the name means that the sample is loaded directly into the mixture of ^{3}He and ^{4}He. The base temperature reached with our probe is 9 mK. We can control the temperature and raise it as high as 1.7 K with $\pm$0.5 mK steady-state accuracy at lower temperatures. This level of control decreases slightly at higher temperatures. Above about 1.3 K, we can maintain the temperature to within about $\pm$2.5 mK.

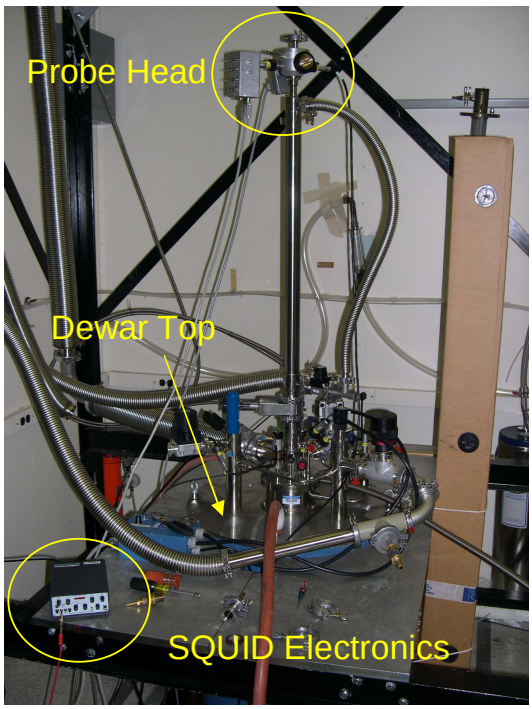

Figure 7.1 *The Oxford TLM used in making our measurements of* $1/f$ *noise. The dewar is nitrogen shielded, super-insulated and extends another five feet below the Al plate upon which the dewar top sits.*

Unlike traditional dilution refrigerators, we can keep the fridge at 1K pot temperatures continuously as we load and unload our sample probe. This allows us to remove the sample probe, modify it, and reinsert it within a single day. The fridge will then return to its base temperature within approximately eight to ten hours. This feature has been particularly helpful for this experiment, with the numerous (on occasion daily) changes we have had to make in order to get the experiment to work.

7.2 Sample Holder and Probe

The dilution refrigerator requires the use of sample probes that are on the order of nine feet in length. The sample is mounted at the bottom of one of these probes inside an Al box designed to shield rf and microwave noise.

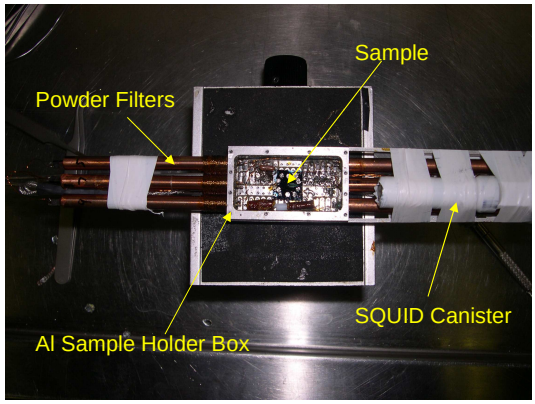

Figure 7.2 *This is a photograph of the Al sample holder box and the copper powder filters through which the measurement leads enter the box. Also visible (though wrapped in teflon tape) is the Nb canister in which a commercially available Quantum Design dc SQUID resides.*

Because the sample holder is immersed in the mixture of ^{3}He and ^{4}He, we added small holes with a 90° turn in their path that lead into the sample box. This allows liquid mixture to enter the sample box in order to cool thoroughly the sample while preventing radiation from entering.

All leads entering the box do so in twisted pairs through a copper powder filter. The filters are made by twisting a pair of two meter long formvar-covered manganin wires around a Teflon^{TM} former. This is inserted into a copper tube which is subsequently filled with a copper powder filled epoxy. This filter attenuates most of the high frequency noise that could couple to the sample through the leads. However, it does add some capacitance, on the order of 300 - 350 pF, due to the use of twisted pairs of wire. Once inside the box, the leads each go to a 100 Ω surface mount resistor before going to the indium pads used to make superconducting contact with the sample.

In addition, superconducting leads that connect the SQUID to the sample exit the Nb canister in which the SQUID resides and travel first through a small lead tube before heading through the copper powder filters and into the sample space. It is necessary that these leads are superconducting so

that no surface mount resistors are in place between the SQUID leads and the sample.

All of the wiring for the experiment extends from the sample box at the bottom of the probe up through the probe and breaks out at the probe head, visible in Fig. 7.1. Each lead has about $\sim 350\ \Omega$ of resistance between the sample box and the probe head due to the use of manganin wire in the probe design and the presence of the 100 Ω resistor in the sample box itself. All the leads are thoroughly heat sinked above the probe displacer.

7.3 Measurement Circuit

7.3.1 With Internal Feedback

Inside the sample box a sample is wired in a test circuit that allows us to current-bias the junction we want to measure. One of the possible circuits we can use is shown in Fig. 7.3. All electronics used in the screened room are powered by batteries. This allows us to shut off the ac power in the screened room, eliminating a considerable amount of 60 Hz noise.

We use a homemade current supply capable of sourcing up to 100 mA. With a 12 bit optically-isolated DAC controlling the current supply, our accuracy is determined by the maximum bias current required. The self-inductance of the circuit loop we estimate to be on the order of 2 μH whereas the mutual inductance coupling the circuit to the SQUID is 10.6 nH. This means that for a change of 195 nA in L_{SQ} there is a corresponding change of one flux quantum in the SQUID. Because we are interested in low-frequency noise (¡ 1 kHz), we assume the inductive component (due to the geometry of the circuit) of the impedance in the circuit loop is negligible. Thus we can

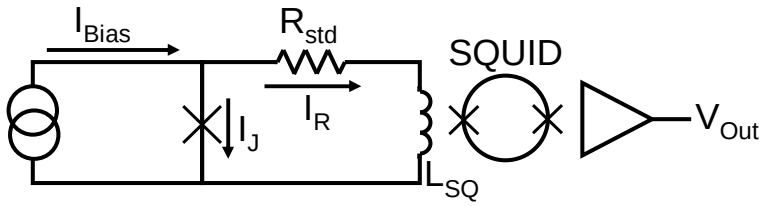

Figure 7.3 *Schematic of the internal-feedback version of the circuit used to measure the* $1/f$ *noise of a Josephson junction. The Josephson junction is in series in a loop with a standard resistor and the input coil of a commercially available SQUID, made by Quantum Design. We connect a room temperature current supply to the junction, such that when the junction is in its finite voltage state the current divides between the junction and the standard resistor/SQUID loop.*

safely assume there is no phase lag between the voltage across L_{SQ} and the current through it.

Operated in the standard flux-locked-loop configuration with internal feedback, the SQUID electronics output a voltage signal proportional to the amount of flux change in the SQUID. On the gain setting we use with the SQUID electronics for our noise measurements, we see a SQUID output voltage change of 0.731 V for a corresponding change of one flux quantum Φ_0 in the SQUID itself. If we change the gain setting, this proportionality constant merely changes by a factor of 10 by every factor of 10 that we increase the gain. Taking this into account with the mutual inductance, a change in current of 195 nA in the circuit loop will result in an addition of one Φ_0 to the SQUID.

As long as I_{bias} is less than the junction's critical current, all the bias current will flow through the junction, which is in its supercurrent, zero-voltage state. However, when the bias current exceeds the critical current, the junction enters its nonzero voltage state in which the junction has some nonzero dynamic resistance (R_D). Now the bias current will split, as in the case of an ordinary current divider. Some will continue to go through the

junction, but because in this regime the junction has a nonzero resistance, some will also go through R_{std}.

The amount of current that goes through each branch is determined by the relative values of R_{std} and R_D. To determine how the current splits, note that the junction and R_{std} are in parallel so that the voltages across the two are equal:

$$\begin{aligned} V_{Junction} &= V_R, \\ I_J R_D &= I_R R_{std}, \end{aligned} \tag{7.1}$$

where $R_D = dV_J/dI_J$. This is a simple relation, complicated by the fact that R_D is a function of I_J. Therefore it is not so straightforward to calculate what the dynamic resistance curve should be. However, based on the value of V_{out} we can determine what I_R is. In order for this to work, we calibrate the SQUID output voltage so that it is zero when zero current flows through R_{std} and L_{SQ}. When this condition is met, it is trivial to calculate the current flowing through the standard resistor based on V_{out}, using

$$I_R = V_{out}\left(\frac{195\text{ nA}}{\Phi_0}\right)\left(\frac{\Phi_0}{0.73\text{ V}}\right) = (0.267\ \mu\text{A/V})\,V_{out}. \tag{7.2}$$

From the manufacturer's specifications and from our own calibration measurements, we have determined that for every 0.27 μA through the SQUID input coil there is a 1 V change in V_{out}. With an accurate measure of the current through R_{std}, we can calculate V_R. This gives us the voltage across the junction. As we have the current through the junction we can arrive at a plot of the dynamic resistance, using Eq. (7.1).

In theory, this approach should work perfectly for the regime in which

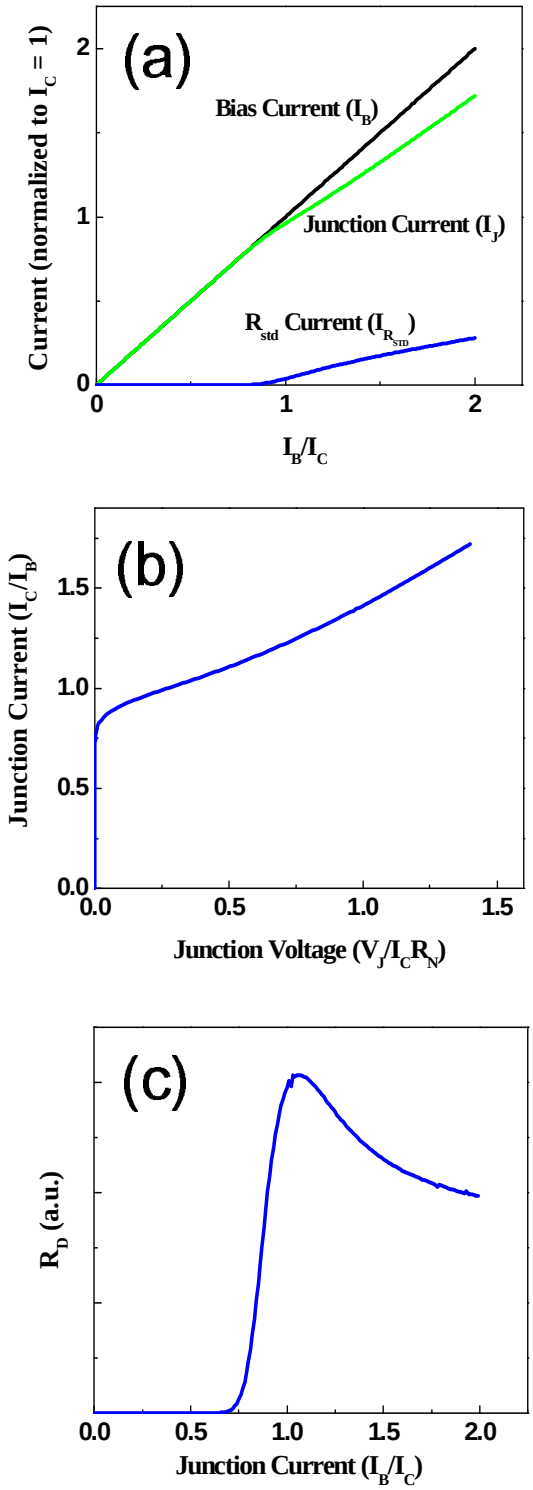

Figure 7.4 *Simulated transport properties for a junction in the internal-feedback experimental setup (a) Plot of the currents through the junction and the standard resistor as a function of bias current. The straight line is the applied bias current, $I_B = I_J + I_{R_{std}}$. (b) $I-V$ curve of a junction in the case where not all the bias current goes through the junction. (c) Dynamic resistance (R_D) of the junction.*

we perform our experiment. However, in practice we have found behavior which is anything but ideal. Figure 7.4(b) shows a simulated $I - V$ curve for a junction in the internal feedback experimental setup, and, as expected, the current through the junction is a monotonic function of the bias applied to the circuit. This is also shown in Fig. 7.4(a) and leads to a well-behaved dynamic resistance dependence on bias.

Although the internal feedback circuit works, there is a significant amount of data manipulation required before we arrive at a meaningful value for the measured noise. We can eliminate most of this by using an alternate experimental technique the relies upon an external feedback loop. As we shall see, the independence of this configuration on the SQUID transfer function lends itself to a simpler circuit analysis and facilitates a quicker transition between raw data acquisition and finished results.

7.3.2 With External Feedback

The purpose of introducing an external feedback path is to eliminate the current splitting that occurs when using the circuit shown in Fig. 7.3. The circuit wiring in the sample box remains identical to that shown in Fig. 7.3, but an external feedback line and resistor are added (Fig. 7.5). As a current bias is applied, the entirety of the current shunts through the Josephson junction, provided the applied current is below the critical current. However, when the applied bias exceeds I_c, some of the current will split into the branch of the circuit that contains R_{std}.

In normal, flux-locked-loop, operation, SQUIDs using an internal feedback path will couple a bias flux back into itself in order to keep the SQUID locked at an extremum of the $V - \Phi$ curve (see [18] for more information

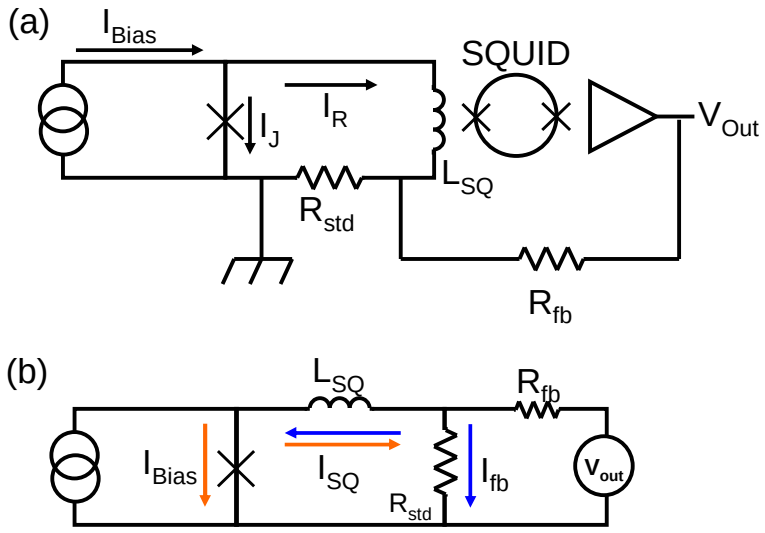

Figure 7.5 *Schematic of the external-feedback version of the circuit used to measure the 1/f noise of a Josephson junction. (a) The Josephson junction is in series in a loop with a standard resistor and the input coil of a commercially available SQUID. We connect a room-temperature resistor (R_{fb}) from the SQUID output to one side of R_{std} in order to feed current back into the circuit, nulling the current that couples to the SQUID. (b) Simplified schematic to illustrate why, when using external feedback, there is no current that couples flux to the SQUID. All bias current goes through the junction, and all feeback current goes through R_{std}, leading to the desired situation in which $I_{SQ} = 0$.*

about SQUID operation as a flux-to-voltage transducer). In short, if there is an applied flux that shifts the SQUID from its quiescent operating point, it will output a voltage in an attempt to drive itself back to its equilibrium point. When the internal feedback is used, this voltage is applied across an internal resistor that leads to an on-chip inductor that couples a bias flux back into the SQUID, sending it back to the equilibrium point. By disconnecting the internal feedback loop, we can provide our own external feedback resistor (R_{fb}) that connects the SQUID output back to the circuit (see Fig. 7.5), transforming the SQUID into a high-impedance voltmeter.

Therefore, when the applied bias current starts to split between the junction and R_{std}, some flux is coupled to the SQUID. At this point, the SQUID output voltage rises, feeding a current back into the circuit. This current

runs through R_{std} in opposition to the applied bias current, thus nulling it, and maintaining the SQUID at its equilibrium point. We can use this external feedback method to measure directly the current and voltage through the junction.

Looking at Fig. 7.5(b), the physics of the nulling effect of the feedback is more obvious. In the absence of the feedback current, the bias current would split between the junction and L_{SQ} when the junction is in its finite voltage state. However, with the external feedback path, the SQUID output voltage rises, sending a current into the circuit which splits between L_{SQ} and R_{std}. Therefore, the current from both sources, flowing in opposite directions through L_{SQ}, add and cancel each other, maintaining $I_{SQ} = 0$. The SQUID will track and null changes over some finite bandwidth that is limited on the upper end by the slew rate of the SQUID electronics. This turns out to be about a kilohertz for our system, well above the range of frequencies that interest us. At low frequencies, the SQUID has no trouble tracking and nulling the signal.

The current through the junction is now just the applied bias current, $I_J = I_B$ because in the presence of the external feedback there is no current through L_{SQ}. To determine the voltage across the junction is equally straightforward. The feedback current is simply $I_{fb} = V_{SQUID_{out}}/(R_{fb}+R_{std})$. All of this current passes through R_{std} which is in parallel with the junction, so the voltages across the two are the same (Eq. (7.1)). Thus,

$$\begin{aligned} V_J &= R_{std} I_{fb} = R_{std} \frac{V_{out}}{R_{fb} + R_{std}} = G^{-1} V_{out}, \\ V_{out} &= G V_J, \end{aligned} \tag{7.3}$$

where $G = (R_{fb} + R_{std})/R_{std}$ is the gain of the circuit. For typical values of

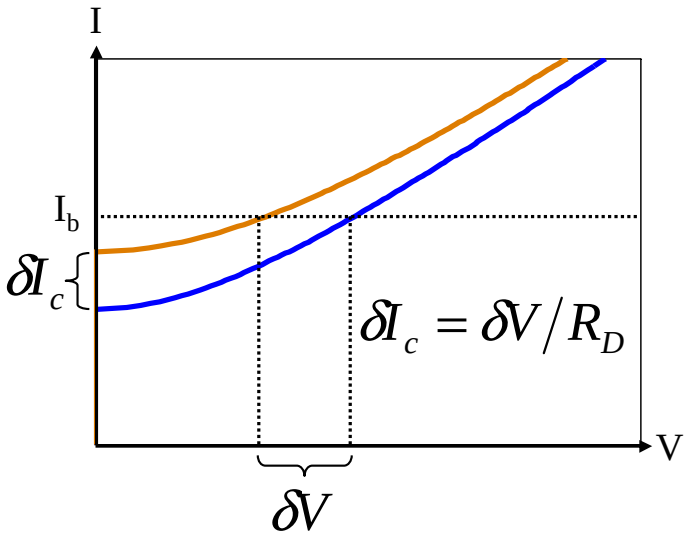

Figure 7.6 *Graphical representation of the relation between δV and δI_c in a Josephson junction $I-V$ curve. For a change of deltaI_c there corresponds a change δV the proportionality constant of which is the dynamic resistance.*

$R_{fb} \approx 200$ kΩ and $R_{std} \approx 1.14$ Ω, this yields a gain of $G \sim 175000$.

In Section 3.2, we alluded to the important fact that the external feedback circuit is a high-impedance measurement circuit. The external feedback circuit is effectively a high-impedance voltmeter. Therefore, critical-current fluctuations manifest as voltage noise across the dynamic resistance, resulting in a current fluctuating around the loop that couples to the SQUID via L_{SQ}. Using a high-impedance configuration means that we measure the voltage across the junction. For example, Fig. 7.6 shows two $I-V$ curves that differ in critical current by an amount δI_c. This would correspond to a situation in which we biased the junction to a constant value, I_b, and then the critical current of the junction changed. In order for us to determine what that change is, we measure the respective change in voltage δV, and divide by the dynamic resistance R_D at that bias point. This extends to the idea of measuring the noise caused by changes in the critical current, and is explored further in the discussion of our results in Chapter 8.

7.4 Noise Sources

This project's goal is to measure the noise present in a Josephson junction. As such, it is imperative that we know the source and can quantify the other types of noise present in our experiment. By looking at Figs. 7.5, and 7.3 we can list several obvious noise sources, the effect of which need to be considered. There is the SQUID itself, the standard resistor, the feedback resistor (if present), and the junction, which produces either white or both $1/f$ noise and white noise depending on where it is biased. Each of these noise sources for both instances of the measurement circuit will be addressed.

7.4.1 Intrinsic SQUID Noise

The SQUID electronics themselves contribute to the background noise. What that amount of noise is depends on the feedback scheme used. For the case of the internal feedback circuit, the analysis is straightforward. The noise level specified by Quantum Design for the commercial dc SQUID we are using is $S_V^{1/2} = 3.40\ \mu\Phi_0/\sqrt{\text{Hz}}$. Given a SQUID transfer function of 0.731 V/Φ_0, this translates into a voltage noise of 2.48 $\mu\text{V}/\sqrt{\text{Hz}}$. We have measured the noise from the SQUID while it is in the internal feedback configuration and found it to be at least as small as the specified value. When using an external feedback path, the effect of the SQUID noise is not so clear-cut.

In order to determine the noise introduced into the measurement circuit by the SQUID when using the external-feedback configuration, we need to calculate the open-loop gain of the SQUID and determine what the small signal response is for the external feedback circuit.

A change in the output voltage, δV_{out}, will be composed of a signal from the SQUID (δV_{SQ}) and from the measured junction (δV_{sig}) when it is in the

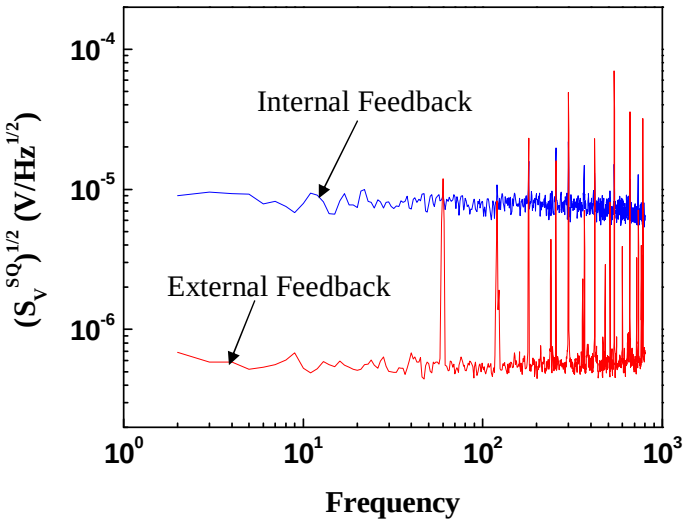

Figure 7.7 *Noise spectra showing the noise from the Quantum Design dc-SQUID in both the internal feedback configuration (8.2 $\mu V/\sqrt{\text{Hz}}$) and in the external feedback configuration (0.55 $\mu V/\sqrt{\text{Hz}}$). The noise from the internal feedback configuration is approximately* 15 *times larger.*

zero-voltage state (see Fig. 7.8):

$$\delta V_{out} = \delta V_{SQ} - \delta V_{sig}, \tag{7.4}$$

where we subtract δV_{sig} because we use a negative feedback configuration.

We can express δV_{sig} in terms of δV_{out}, R_{fb}, and the mutual inductance M by noting what signal results from a change in the output voltage:

$$\begin{aligned} \delta I &= \frac{\delta V_{out}}{R_{FB}}, \\ \delta \Phi &= \frac{M \delta V_{out}}{R_{FB}}, \\ \delta V_{sig} &= \frac{M \delta V_{out}}{R_{FB}} \left(\frac{\partial V}{\partial \Phi} \right), \end{aligned} \tag{7.5}$$

where $\partial V/\partial \Phi$ is the flux-to-voltage gain of the SQUID. We can insert Eq. (7.5) into Eq. (7.4) and solve for δV_{out} in terms of the small-signal SQUID voltage,

δV_{SQ}:

$$\begin{aligned}
\delta V_{out} &= \delta V_{SQ} - \frac{M\delta V_{out}}{R_{FB}}\left(\frac{\partial V}{\partial \Phi}\right), \\
\delta V_{out} &= \left(\frac{1}{1+\frac{M}{R_{FB}}\frac{\partial V}{\partial \Phi}}\right)\delta V_{SQ}, \\
\delta V_{out} &= \left(\frac{1}{1+G_{open}}\right)\delta V_{SQ}. \qquad (7.6)
\end{aligned}$$

The open-loop gain, $G_{open} \approx 18$, is the factor by which the SQUID noise is reduced when using the external-feedback circuit configuration. This is visible in Fig. 7.7, in which the background noise due to the SQUID in both internal-feedback and external-feedback configurations is plotted. The measured SQUID noise, when in the external feedback setup ($0.55\mu\text{V}/\sqrt{\text{Hz}}$), is about 15 times less than what we measure the noise to be when in the internal-feedback setup (8.2 $\mu\text{V}/\sqrt{\text{Hz}}$). The difference in what we measure versus what we calculate is likely to be due to some inaccuracy in determining the values of M and R_{FB} precisely enough.

7.4.2 Standard Resistor Noise

Another source of noise is the standard resistor, present in both measurement circuits. Because the circuit is coupled inductively to the SQUID, we need to know the current noise flowing through L_{SQ} produced by Johnson noise from the resistor. The standard resistor is at dilution refrigerator temperatures, 10 mK $< T <$ 1.5 K. Typically, our measurements are made with $R_{std} \approx$ 1.14 Ω. The current noise from the standard resistor therefore ranges from $(4k_BT/R_{std}) \approx 4.84 \times 10^{-25}$ A^2/Hz for $T = 10$ mK to $(4k_BT/R_{std}) \sim 7.2 \times 10^{-23}$ A^2/Hz for $T = 1.5$ K. For the internal feedback circuit, all of this current noise couples directly to the SQUID via L_{SQ}.

In the unbiased state, when the junction acts like a superconducting short, all of this noise is coupled to the SQUID. But this treatment fails when the standard resistor is not the only resistance in the circuit. If there were another resistance, such as a Josephson junction biased into the finite voltage state in which $R_D \neq 0$, then the Johnson noise produced by the resistor would lead to less current noise. In this circumstance, a different formula would be used to calculate the current noise seen by the SQUID:

$$S_I^{R_{std}} = \frac{4k_BTR_{std}}{R_{total}^2} = \frac{4k_BTR_{std}}{(R_{std}+R_D)^2}. \tag{7.7}$$

For a typical dynamic resistance value measured in the samples from NIST Boulder made by Kevin Osborn (Al trilayer, $25\ \Omega < R_D < 3\ \Omega$), this translates into a white-noise component from the standard resistor that is an order-of-magnitude less than for the unbiased case. However, this noise still couples directly to the SQUID and, given the mutual inductance $M = 10.6$ nH, leads to a white noise component in the SQUID output voltage of $\sim 1.4 \times 10^{-10}$ A^2/Hz on the high end.

The contribution of the Johnson noise produced by the standard resistor to the noise seen by the SQUID is not the same when we use the external feedback circuit. Consider Fig. 7.8 for the circumstance in which the bias current is less than the critical current. The standard resistor is in parallel with an ideal inductor and this combination is in series with the feedback resistor. Because of the feedback network in place, the SQUID maintains zero current through L_{SQ}. As the inductor is superconducting, the only way to achieve this is by keeping the voltage at Point **a** in Fig.7.8 zero, i.e. $V_a = 0$.

Therefore, when a voltage noise develops across R_{std} (e.g. Johnson noise) the SQUID will null it in order to maintain the condition that the current

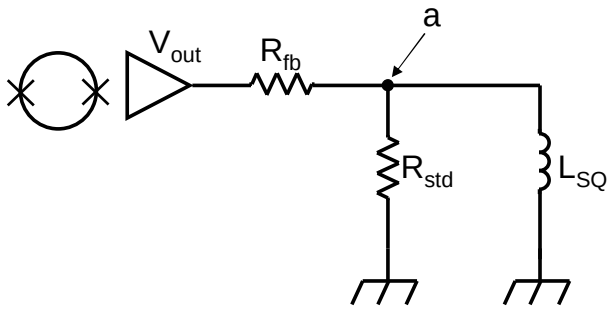

Figure 7.8 *Simplified schematic of the external feedback circuit in the circumstance that $I_B < I_C$. The SQUID, via the feedback resistor, attempts to maintain zero current through L_{SQ} by keeping $V_a = 0$.*

through L_{SQ} remain zero. A small signal analysis will determine how the SQUID responds to a change in voltage across the resistor $\delta V_{R_{std}}$, which means $V_a^{R_{std}} = \delta V_{R_{std}}$. The SQUID will output a voltage $V_{SQ} = I_{SQ}(R_{fb} + R_{std})$, which will bring the voltage at Point **a** back to zero. The additional voltage at Point **a** due to the current sourced by the SQUID will be $V_a^{SQ} = I_{SQ}R_{std}$. By definition, this voltage must equal the voltage due to the noise term: $V_a^{SQ} = V_a^{R_{std}} = \delta V_{R_{std}}$. We can therefore solve for the SQUID output voltage in terms of the voltage caused by Johnson noise:

$$\begin{aligned} V_{SQ} &= -\frac{R_{fb} + R_{std}}{R_{std}} \delta V_{R_{std}} \\ &= -\delta V_{R_{std}} G. \end{aligned} \tag{7.8}$$

Here, G is the feedback gain that we found above in Eq. (7.3). Therefore, the noise power at the SQUID output is proportional to the voltage noise produced by Johnson noise in resistor:

$$S_V^{SQ} = S_V^{R_{std}} G^2. \tag{7.9}$$

This results in a Johnson noise power of $4k_B T R_{std} G^2 = 2 \times 10^{-14}$ V^2/Hz for $T = 10$ mK and 3×10^{-12} V^2/Hz for $T = 1.5$ K.

7.4.3 Junction Noise

Finally, there is the noise produced by the junction itself. When $I_B < I_C$, the junction contributes some current noise at finite frequencies, but we can neglect it, as it is a superconducting short. However, this is not the case when $I_B > I_C$. When a resistively-shunted junction is biased into the finite voltage state, there are known to be at least two forms of noise produced. The first, and what we are studying in this project, is $1/f$ noise. See [10, 22, 41, 63, 64, 49, 70], among others, for similar work done measuring $1/f$ noise in SQUIDS and Josephson junctions. In addition to the $1/f$ noise, whose temperature dependence we hope to determine at low frequencies, there is a white-noise component [24, 30, 61, 25, 60].

The nature of the $1/f$ component is commonly believed to arise from the superposition of single fluctuators with a specific distribution of lifetimes (see Chapter 3). Despite the absence of a universal $1/f$ noise mechanism, Van Harlingen *et al.* compiled an empirical result that predicts the magnitude of the $1/f$ noise in Josephson junctions at 4.2 K, given specific junction parameters (see Eq. (5.2) and [57]). We hope to add to the understanding of this phenomenon. However, there is a relatively good understanding of the white noise produced by a resistively shunted junction biased into the nonzero voltage state, and we can compare this value to what is predicted by Van Harlingen *et al.*'s formula.

The white noise originates in the shunt of resistively shunted Josephson junctions. It is different from critical-current noise in origin, is white, has been studied extensively, and produces some noise rounding of the I-V curve at low voltages. For the case in which there is a nonzero amount of junction capacitance, Kurkijärvi and Ambegoakar [25] and Voss [60] computed the

power of the noise. Likharev and Semenov [30] and Vystavkin *et al.* [61] showed that, for the $C = 0$ case in the limit $h\nu_J \ll k_B T$ ($\nu_J = 2eV/h$ is the Josephson frequency), and for frequencies much less than ν_J, the spectral density of the voltage noise is given by

$$S_V^J(T) = \frac{4k_B T R_D^2}{R_s}\left[1 + \frac{1}{2}\left(\frac{I_c}{I_B}\right)^2\right],$$

where R_D is the dynamic resistance, R_s is the shunt resistance, I_c is the critical current, and I_B is the applied bias current. The second term, which is proportional to the square of the critical current of the junction, is due to noise mixing down from the Josephson frequency ν_j, as discussed in [24]. This formula is based upon the assumption that the noise is sufficiently small that there are no significant departures from the ideal RSJ I-V characteristic given by Eq. (2.30).

Again, the effect of this noise on the SQUID output signal depends on whether or not we use an internal feedback scheme or an external one. In the case of the internal feedback circuit (Fig. 7.3), we notice that this is effectively a voltage supply in series with two resistors, R_{std} and R_D. Therefore, the current noise produced by the intrinsic junction voltage noise is

$$S_I^J(T) = \frac{4k_B T}{R_s}\left[1 + \frac{1}{2}\left(\frac{I_c}{I_B}\right)^2\right]\frac{R_D^2}{(R_{std} + R_D)^2}. \tag{7.10}$$

When we bias the junction to the peak in the dynamic resistance, where $I_B > I_c$, we can use the above expression to estimate the amount of white noise that the junction and its shunt resistor contribute to the background signal. For a typical junction, $R_s \approx 2\ \Omega$, $R_D \approx 5\ \Omega$, $I_B \approx I_0$, $T \approx 10$ mK or as much as 1.5 K. Therefore, the flux noise power seen by the SQUID is

of order 7×10^{-12} Φ_0^2/Hz at low T and as much as 1×10^{-9} Φ_0^2/Hz at high temperatures.

This situation changes when we examine the effect of this white noise and, more generally, all noise originating in the junction. We saw in Section 7.3.2 that voltage noise from the junction is seen at the output of the SQUID, amplified by the gain. We also saw in Section 7.4.2 that the noise from the standard resistor is likewise amplified by the gain. Putting these results in a more general form we can write

$$S_V^{SQ}(T) = S_V^J(T) + S_V^{R_{std}}(T), \tag{7.11}$$

as the noise produced by either the junction or the standard resistor is incoherent; thus, the noise powers simply add.

The noise from the junction, $S_V^J(T)$, can be further reduced to its constituent parts (white noise and critical-current noise):

$$S_V^J(T) = S_V^{white}(T) + S_V^{I_c}(T).$$

Using Eq. (7.10) and the junction parameters listed above, we arrive at the amount of white voltage-noise produced by the junction: 1×10^{-23} V^2/Hz $< S_V^J(T) < 1.5 \times 10^{-21}$ V^2/Hz, depending on the temperature. From Eq. (5.2) we can estimate the current noise produced by the critical-current fluctuations and, by using the dynamic resistance, compare this to the number that we have just calculated for the white noise produced by the junction, to determine whether or not the $1/f$ component should be easily observable. By using the junction parameters for an approximately ideal junction of small area and small critical current ($I_c \sim 1\mu$A, $A \sim 0.01\mu$m^2) at 1.5 K and 1 Hz, the critical-

current noise is expected to be S_{I_c}(1 Hz, $T = 1.5$ K)$= 1.8 \times 10^{-19}$A^2/Hz. At lower temperatures, this becomes S_{I_c}(1 Hz, $T = 10$ mK)$= 8.2 \times 10^{-24}$ A^2/Hz assuming a T^2 dependence of the noise. To get the voltage noise, we multiply by $R_D^2 \sim 25\ \Omega^2$, giving 2×10^{-22} V^2/Hz $< S_V^{I_c} < 4.6 \times 10^{-18}$ V^2/Hz. These values of the voltage noise easily dominate over the white noise from the junction, as well as the Johnson noise from R_{std}, suggesting (as expected) that we will see be able to observe $1/f$ critical-current noise for small enough junctions below some nonzero frequency.

Figure 7.9 summarizes all the above noise calculations for a specific temperature, $T = 100$ mK. The other specific parameters used are listed in the caption. As seen in the figure, the expected $1/f$ noise signal expected when using the internal feedback configuration ($\sim 9 \times 10^{-11}$ V^2/Hz) is greater than the expected signal for the external feedback configuration ($\sim 2.5 \times 10^{-11}$ V^2/Hz). However, the background noise in the internal feedback configuration is higher, and, in short, this leads to a smaller signal-to-noise ratio for the internal feedback configuration of 1.66 versus 1.92 for the external feedback configuration.

To summarize, we expect the junction $1/f$ noise to exceed the SQUID $1/f$ noise. The dominant white noise will be from the junction's shunt resistor. In general, accounting for the various noise sources, we expect to see a clear $1/f$ noise signal from the junction at frequencies below roughly 10 Hz.

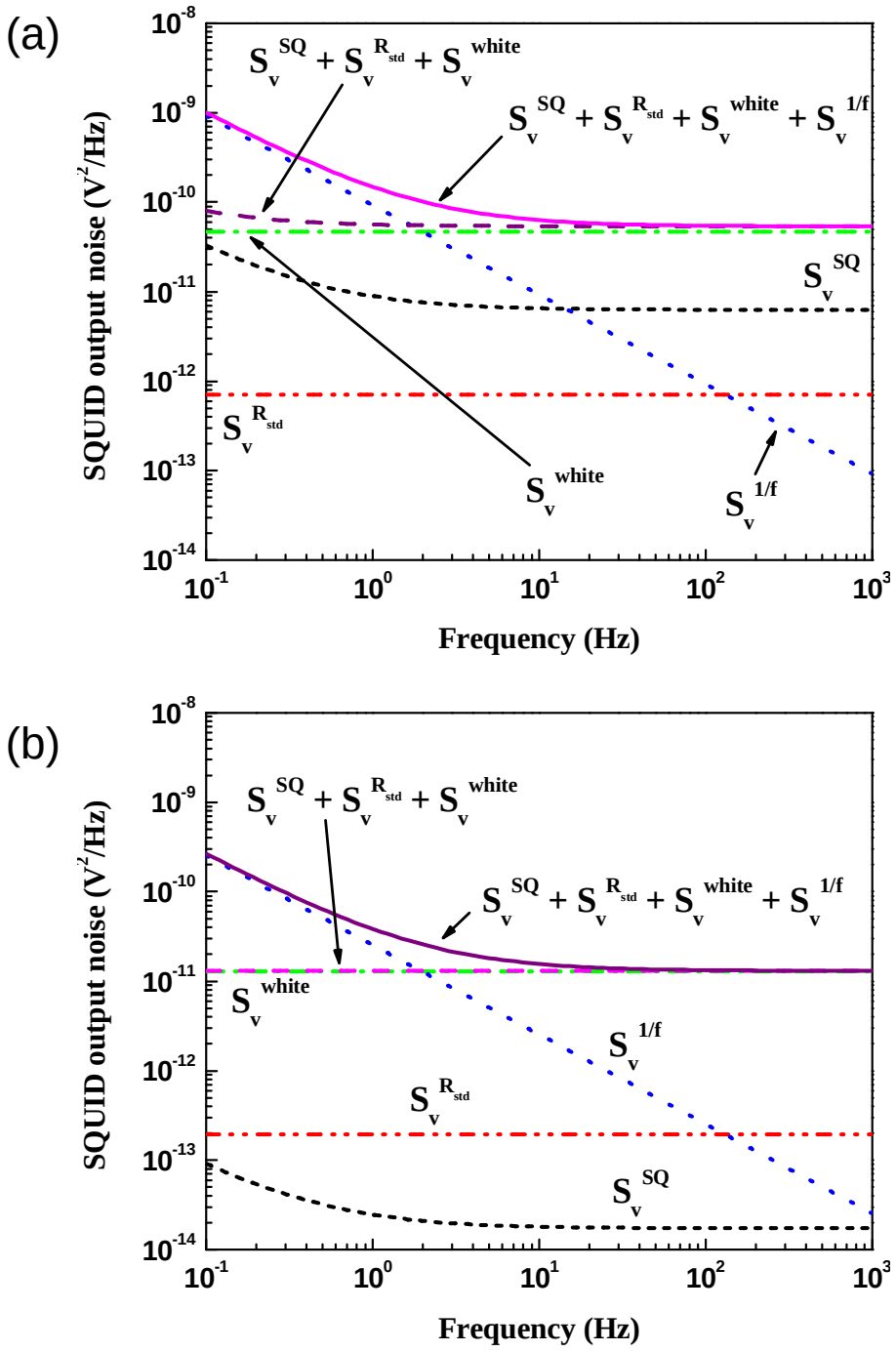

Figure 7.9 *Calculated noise levels for the various expected noise sources for $T = 100$ mK, $R_D = 10\ \Omega$, $R_{std} = 1.14\ \Omega$, $R_{shunt} = 2\ \Omega$. These values were selected as more or less average values. The $1/f$ noise is calculated for an ideal, small-area junction. Note that S_V^{white} is the expected white noise from the junction. (a) Noise levels for the internal feedback configuration. Expected signal-to-noise ratio is 1.66. (b) Noise levels for the external feedback configuration. Expected signal-to-noise ration for this configuration is 1.92. All noise values are calculated as the voltage signal out of the SQUID electronics.*

8 Experimental Results

In this chapter we will review the experimental results of measurements made on two types of Josephson junction – the *Nb* trilayer junctions produced in our laboratory and the *Al* trilayer junctions produced by Osborn at NIST-Boulder. Attention will be given to considerations of heating leading to an elevation of the measured noise levels. We also will revisit the question of qubit decoherence for qubits incorporating junctions similar to those measured and calculate approximate dephasing times using our measured noise levels. Finally, we will discuss future directions for this research, based upon questions raised by the current data.

8.1 Nb Trilayer Junctions

We fabricated our own Nb trilayer, large size-scale Josephson junction, as described in Chapter 6. We found that we could easily measure the $1/f$ noise of these samples. Unless otherwise specified, we used the internal feedback circuit configuration for the following measurements on junctions measuring 5 μm square and with $I_c \approx 25$ μA (see Fig. 8.1).

The process for making measurements is fairly straightforward and remains more or less unchanged, regardless of the feedback method used. A measurement of the background noise is made and then followed by a measurement of the junction noise when biased above the critical current. If the spectrum showed a clear flattening at higher frequencies, we used this

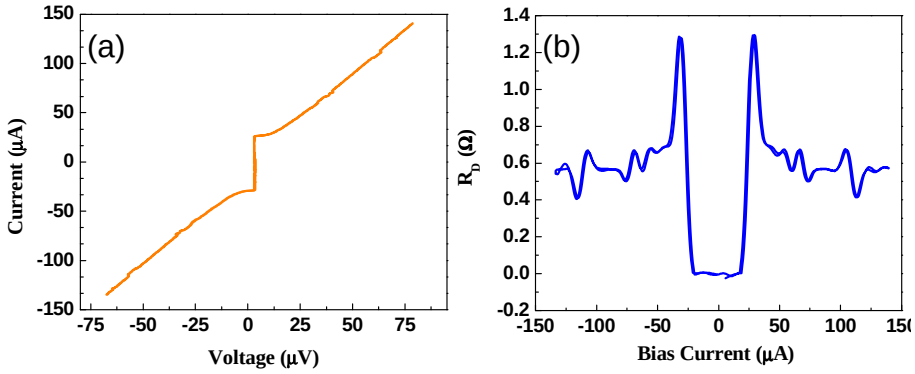

Figure 8.1 *Nb trilayer junction with $A = (5\ \mu m)^2$, $I_c \approx 28\ \mu A$, at 20 mK. This corresponds to a critical-current density of $J_c \approx 100\ A/cm^2$, which is common for the trilayer junctions. (a) Four point measurement of the $I - V$ characteristic curve in the dilution refrigerator. (b) Dynamic resistance curve calculated by differentiating (a).*

base level as the background signal. We could then subtract the background signal from the $1/f$ signal, and this would give us the contribution of the critical-current fluctuations to the noise. Because the circuits described in Section 7.3 are high-impedance ones, we measure voltage noise power and divide by the square of the dynamic resistance to obtain a measure of the critical-current noise:

$$\begin{aligned} S_V^{I_c} &= S_{I_c} R_D^2, \\ S_{I_c} &= S_V^{I_c} / R_D^2. \end{aligned} \tag{8.1}$$

For example, in the data shown in Fig. 8.2, the $1/f$ signal is $\sim 5 \times 10^{-21}$ A^2/Hz and the background is $\sim 9 \times 10^{-23}$A^2/Hz, resulting in a critical-current noise level only slightly less than the $1/f$ signal value.

The basics of the experiment call for making this type of measurement as a function of temperature and/or bias current. Ultimately, we are interested in the noise magnitude as a function of temperature, but for a given temperature we can also measure what the critical-current noise does as a function of

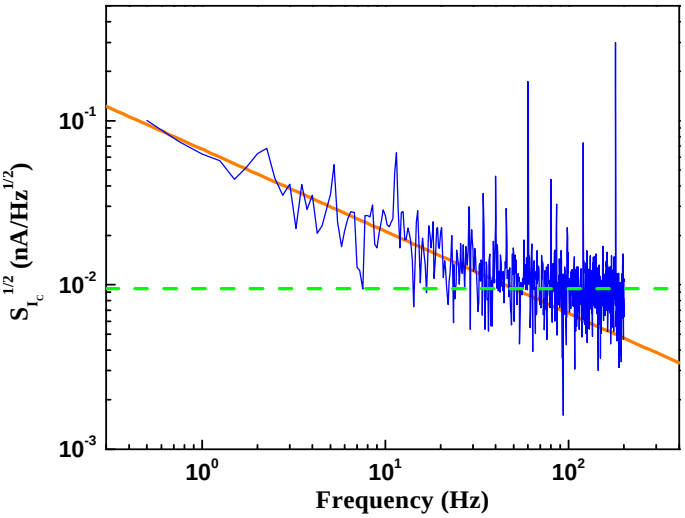

Figure 8.2 *$1/f$ spectrum from a Nb trilayer junction. The junction was current biased to the peak of the dynamic resistance curve for this measurement. The straight solid line indicates a $1/f$ spectrum, and the dashed line indicates approximate background noise level.*

current through the junction.

There are questions associated with any of these measurements, however. The first, and most important, is whether or not this noise is, in fact, due to critical-current fluctuations. The most obvious check is if the $1/f$ nature is visible when $I_b < I_c$. Second, when biased above I_c, the noise should scale with R_D. Furthermore, the noise should also depend on the area of the junction. However, the only way to check this would be to compare junctions that are identical in all respects except area. Although we did measure junctions of differing areas, we were never convinced that the area was the only varying parameter, so it remains unclear what the noise from our junctions does when only the area is changed. Despite this, we believe there is enough circumstantial evidence to support our supposition that the noise we observe is caused by critical-current fluctuations. Naturally, every time we measured the critical-current noise, we acquired spectra for both $I_b < I_c$ and $I_b > I_c$ to determine if there was some type of unexpected noise. In the

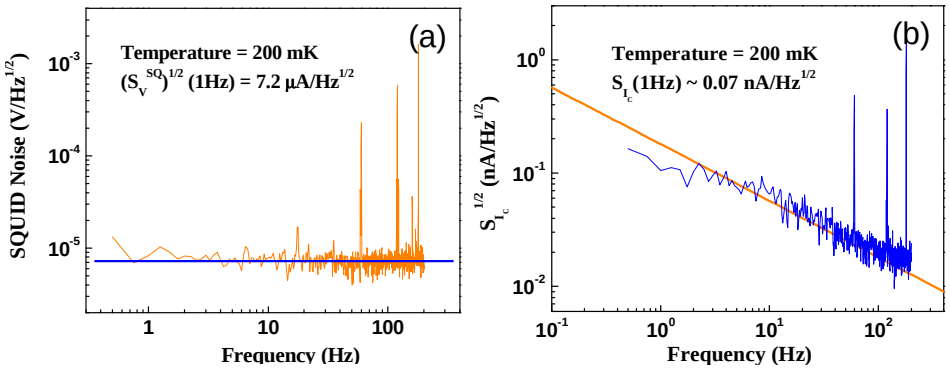

Figure 8.3 *(a) Noise spectrum acquired for $I_b < I_c$ showing a white noise spectrum. (b) Noise spectrum for $I_b > I_c$ showing a clearly $1/f$ frequency dependence.*

former case, the noise should be entirely white, or white with some small $1/f$ component from the SQUID at frequencies below the manufacturer's specified corner frequency of 0.425 Hz. As is clear from Fig. 8.3(a), this is the case. Also visible in Fig. 8.3(b) is the $1/f$ nature of the measured noise.

As mentioned above, we can also look at the junction noise as a function of bias. Any noise originating in the junction should scale as the dynamic resistance. This includes the $1/f$ noise as well as the white noise described in Section 7.4.3. Figure 8.4(a) shows the SQUID output noise signal as a function of bias current for the sample described in Fig. 8.1. When the output signal is appropriately normalized by the dynamic resistance and plotted again versus the bias current, we see a relatively flat line of noise, independent of bias. This is the expected behavior of the noise and provides some assurance that the noise originates with the junction. Deviations from the flat, dotted line in Fig. 8.4(b) are likely due to some degree of inaccuracy in measuring the dynamic resistance. Because we attempt to bias the junction to the peak of the R_D curve, any slight offset in the applied current could lead to a large change in the perceived dynamic resistance.

Another possibility that requires mention is that the current supply itself

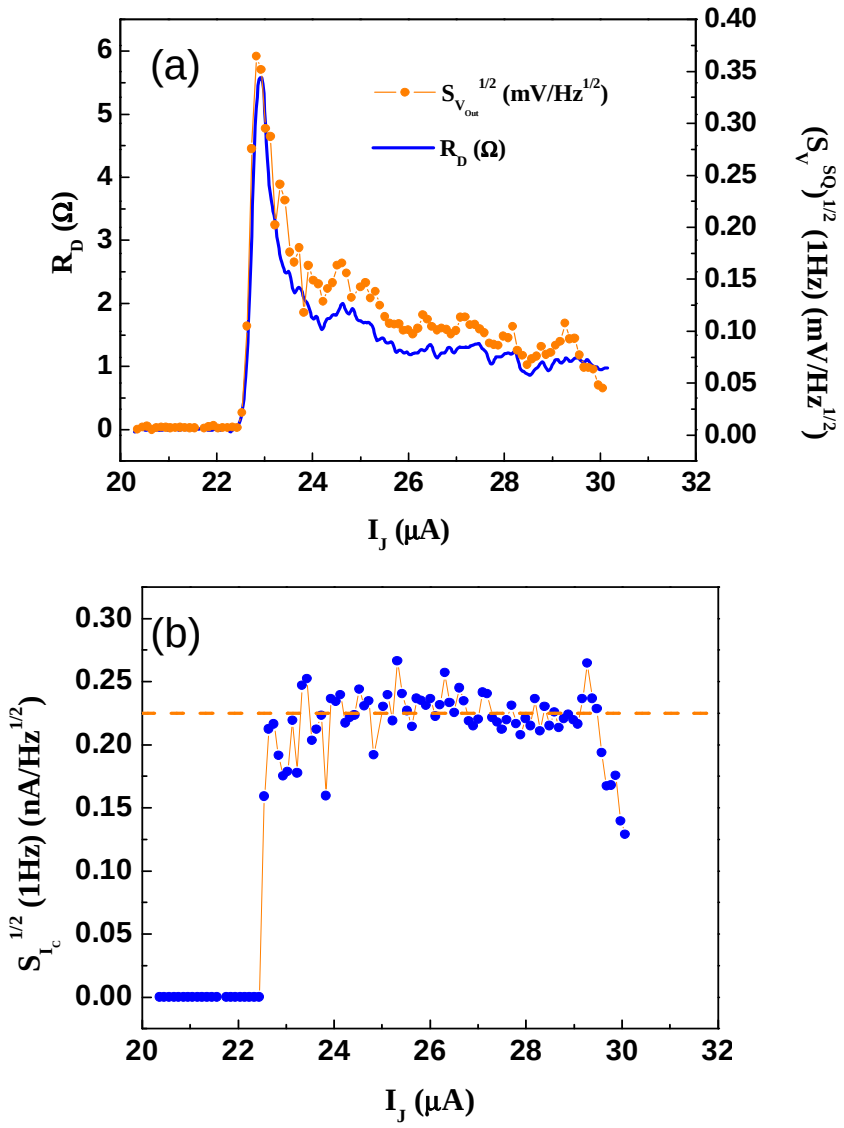

Figure 8.4 *Data from a Nb trilayer junction taken at 400 mK (a) Overlaid graphs of the dynamic resistance, R_D, and the SQUID output voltage noise versus the current through the junction. (b) Critical-current noise from (a), after being normalized by R_D as a function of bias current.*

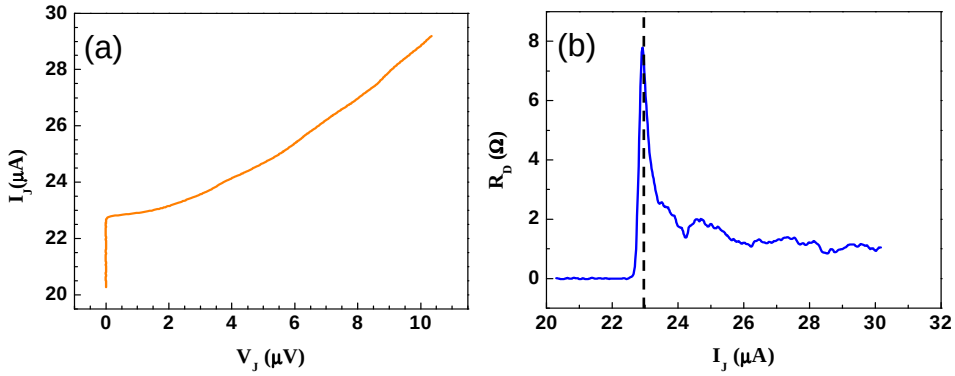

Figure 8.5 *$I-V$ and R_D curves taken at 200 mK. Curves such as these are taken for every temperature at which we want the noise magnitude. (a) $I-V$ curve showing a close-up of the transition from the zero-voltage to finite-voltage state. (b) R_D curve calculated from (a). The dashed line shows where the junction is biased for an ideal noise measurement.*

is the source of the $1/f$ noise. If this were the case, any current noise from the junction would also scale with the dynamic resistance. However, we measured the noise from the current supply and found it to be negligible in magnitude and completely white in spectral content.

Given the data presented above, we believe we are justified in holding our view that the $1/f$ noise seen in spectra such as Figs. 8.2 and 8.3(b) is in fact due to critical-current fluctuations. We can now turn our attention to the issue of temperature dependence. In order to measure the temperature dependence of the noise, we ramped the temperature of the sample box in the dilution refrigerator by 100 mK increments from 10 mK up to 1.6 K. At each temperature point we measured the $I-V$ curve and extracted the R_D curve of the junction. The repetition of this process is necessary, because, as we change the temperature, the critical current and dynamic resistance change (see Fig. 8.6). In order to measure accurately the critical-current noise, it is essential to have an accurate measure of the dynamic resistance for the bias point at which we measure the noise.

As an aside, the reader will notice a difference in the peak height of the

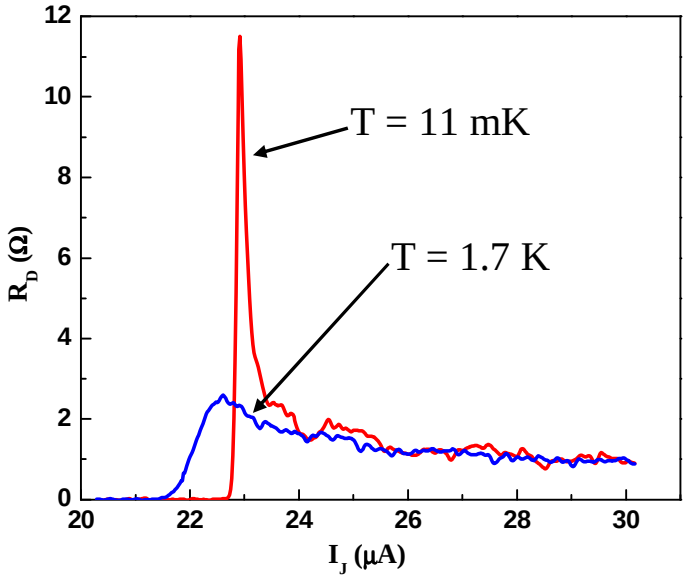

Figure 8.6 *Dynamic resistance curves taken for the same junction at two different temperatures – 11 mK and 1.7 K acquired with the maximum resolution necessary to judge accurately the peak R_D value.*

dynamic resistance curve in Fig. 8.1 versus that in Fig. 8.5. Because the data is composed of discrete points, each point must be sufficiently close in order to justify the use of a linear approximation to the slope of the $I - V$ curve as a function of bias. In Fig. 8.1, this was not the case, because, for a simple measurement of I_c, point spacing is not critical. However, when we measure the $1/f$ noise of the junction, an accurate value of R_D is necessary, so we decreased the point spacing until the R_D peak stops increasing. At this point, we assume we are sampling closely enough in current-space that we will accurately record the peak dynamic resistance value where R_D changes quickest.

With an accurate measure of the dynamic resistance as a function of bias current, we bias the junction to the peak of the dynamic resistance. Because the $1/f$ noise scales with the dynamic resistance whereas most of the environmental noise does not, we can achieve a higher signal-to-noise ratio at higher R_D values. Following this procedure, we can plot the noise

dependence on temperature.

8.1.1 Measurements from 1.5 K to 5.8 K

The first data plot of the temperature dependence is actually for higher temperatures, shown in Fig. 8.7. We were able to take this data using a standard, pumped, liquid helium cryostat, allowing us to access the temperature regime shown from 1.5 K to 5.8 K. We retrofitted this cryostat to accept the probe we use in the dilution refrigerator, obviating the need for any serious reworking of the experimental setup. This is important for our Nb trilayer samples, which have $T_c \sim 8.5$ K, but is unnecessary for the Al samples, as the T_c of Al is 1.2 K.

The data presented in Fig. 8.7 clearly shows a T^2 dependence, as expected from [70, 67] and reviewed in Section 3.2. There are, however, some outlier points that deviate from the expected relationship. We believe the solid line indicating a T^2 dependence is the lower limit for the noise in this junction, and any data points that show a higher noise magnitude were affected by some other, unaccounted for, noise source. One option is that, by coincidence, the bias at which the noise was measured corresponded to some type of resonance in the junction, such as a Fiske mode or perhaps a resonator similar to the type described by Simmonds *et al.* in [50]. Another option could be the presence of additional environmental noise. The SQUID is very sensitive to mechanical vibrations, so any disturbances in the building are likely to contribute to the overall noise level. Further, if there are a small handful of two-level systems (TLS) that are dominant in the junction at a specific temperature, the spectrum would not be purely $1/f$, and to extract a single value for the $1/f$ noise in this circumstance would be misleading.

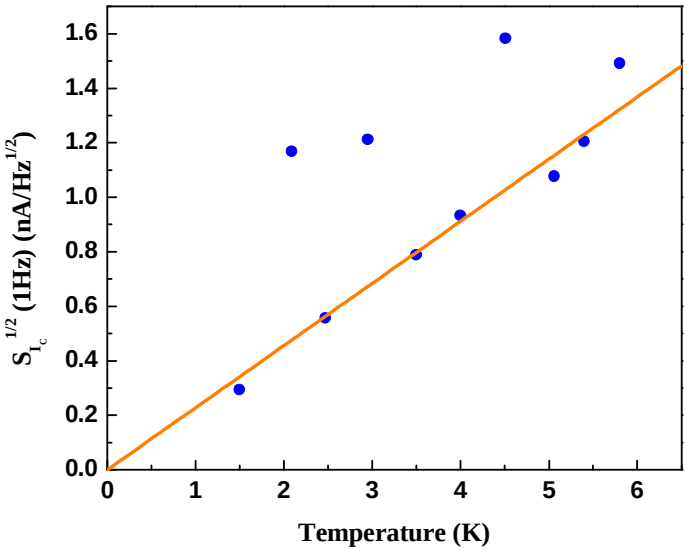

Figure 8.7 *Plot of the critical-current noise versus temperature for higher temperatures. The solid line indicates a T^2 dependence. The sample measured is 7×7 μm^2, $I_c \sim 85$ μA.*

8.1.2 Measurements from 10 mK to 1.6 K

By using a different junction we probed the noise dependence at lower temperatures as well. This sample failed before we could measure it at higher temperatures, but we were able to measure it from 10 mK up to 1.6 K, as shown in Fig. 8.8.

The immediately striking feature of the low temperature data shown is the flattening out of the noise at approximately $T = 870$ mK. This behavior is expected, but the question has always been: at what temperature this will occur? If the $1/f$ noise is due to the superposition of many thermally activated TLS, there should be a temperature below which the TLS enter the quantum regime. Once this happens, the TLS should not switch states due to thermal activation, but rather from quantum tunneling between the available states. This will result in a flattening of the temperature dependence, as we see. Rogers and Burhman found, from experiments performed on metal-insulator tunnel junctions [47, 48], that the crossover from thermal activation

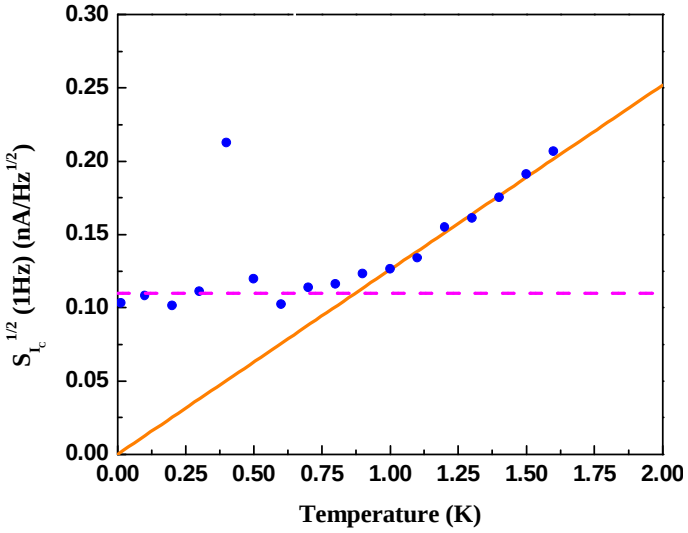

Figure 8.8 *Plot of the critical-current noise magnitude versus temperature for low temperatures. The solid indicates a T^2 dependence, and the dashed line indicates no temperature dependence. The sample measured is 5×5 μm^2, $I_c \approx 25$ μA.*

should occur at a temperature on the order of 10 K (see Fig. 3.5). We do not necessarily expect this result to hold rigidly in our system, but we do expect a flattening to occur at a temperature well above the 90 mK threshold set by Wellstood *et al.* in [70], and ~ 1 K does not seem an unreasonable scale at which this could occur.

8.1.3 Concerns about Heating

However, an alternative possibility is that this flattening is due to heating. If the local temperature of the substrate and sample is different from the sample box temperature (to which the thermometer is affixed), the noise magnitude will not necessarily correspond to the measured temperature. In particular, we current-bias the junction to the point at which the dynamic resistance is at its highest. This is in the nonzero-voltage regime, so some amount of power is dissipated by the junction. It is typically assumed that when shunted Josephson junctions dissipate power, it is the shunts from which the

power is dissipated. If the cooling power of the surrounding ^{3}He/^{4}He mixture is too low to dissipate thoroughly the power from the shunts, they will heat and, due to their proximity to the junction barrier, cause the barrier to heat as well.

We believe there is sufficient cooling power to keep the substrate upon which the junction is fabricated at the same temperature as the the rest of the mixture. This is an advantage of using the TLM dilution refrigerator; the sample is immersed in the mixture. However, we can only say with any certainty that the substrate temperature of the sample is what we expect. There remains the possibility of phonon and electron heating, due to an inadequate amount of cooling power between the substrate and the phonons and between the phonons and electrons, i.e., a high Kapitza resistance and a high phonon-electron thermal resistance.

The possibility of electron heating in thin films was addressed by Wellstood *et al.* [69]. A schematic breakdown of the thermodynamic subsystems is shown in Fig. 8.9. The central conclusion of their work is an expression relating the temperatures in the electron gas and phonons to the power dissipated by the electrons:

$$P = \Sigma\Omega\left(T_e^5 - T_p^5\right), \tag{8.2}$$

where Ω is the volume of the thin film, and

$$\Sigma \equiv \frac{\hbar}{2\rho v_s}\left[\frac{2\epsilon_f}{3}\right]^2 \frac{D(\epsilon_f)k_B^5\Gamma(5)\zeta(5)}{2\pi\hbar^5 v_s^3 v_f \Omega}.$$

Here, v_f is the Fermi velocity, $\Gamma(n)$ is the gamma function, and $\zeta(n)$ is the Riemann zeta function. Essentially, Σ is a materials-dependent factor, which

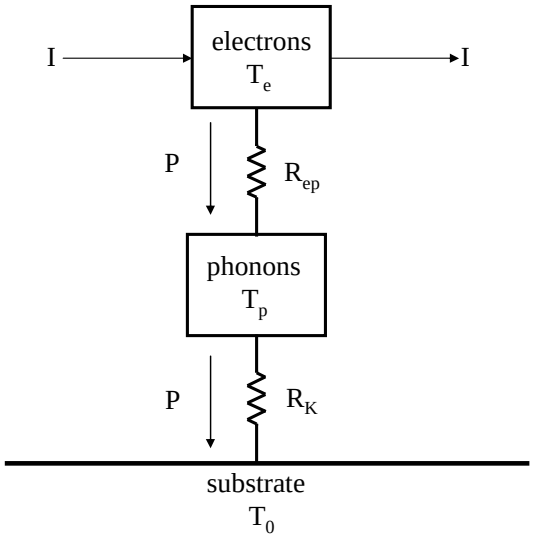

Figure 8.9 *Coupling between thermodynamic subsystems. Power dissipated by the electron gas by a current, I, flows into the phonons via the electron-phonon interaction which can be modeled as a thermal resistance, R_{ep} and then into the substrate via the Kapitza resistance, R_K. At steady state, the power dissipated by the electrons into the phonon bath is equal to the power transferred from the phonons to the substrate. From [69].*

we estimate for our shunt resistors to be 2.4×10^{-8} $\mathrm{Wm^{-3}K^{-5}}$, using the estimate given in [69]. Wellstood *et al.* made the simplifying assumption that the phonon temperature could be adequately approximated by the bath temperature because, at the relevant temperatures, the thermal phonon wavelengths are on the order of the film thickness. We feel confident in making the same assumption, which leads to an effective electron temperature

$$T_e \approx \left(\frac{P}{\Sigma \Omega} + T_0^5 \right)^{1/5}. \tag{8.3}$$

We can use this to approximate the electron temperature in the shunts of our junctions. The junction that we measured to get the data shown in Fig. 8.8 has a shunt with an approximate area of $2000 \mu\mathrm{m}^2$ and a thickness of 260 nm, giving $\Omega = 5.5 \times 10^{-16}$ m^3. Furthermore, the resistance of the shunt is $\sim 0.6\ \Omega$ which can be found from at Fig. 8.1(a), where the $I - V$

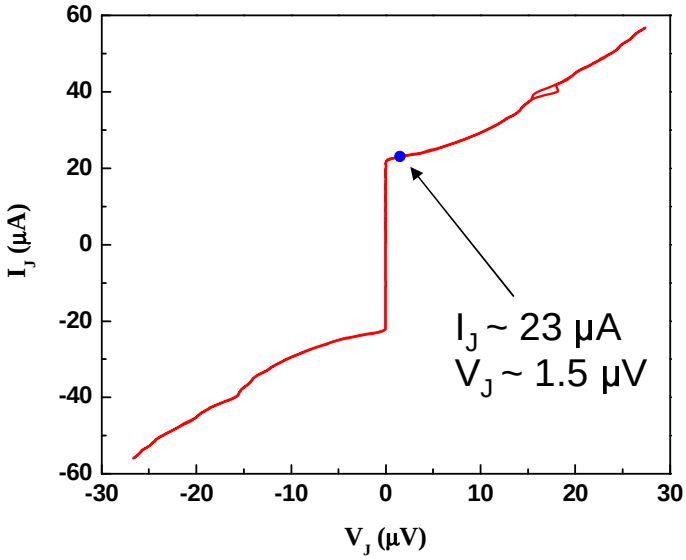

Figure 8.10 *$I-V$ curve of a Nb trilayer junction with $A = 25\ \mu m^2$ and $I_c \approx 25\ \mu A$ at 10 mK. The dot shows where the junction was biased for the calculation of possible hot-electron effects for comparison with a noise spectrum taken at that bias. The estimated power dissipation in the shunt is 3.75 pW.*

is linear. At the lowest temperature (10 mK) the hot-electron effect will be most pronounced, so we calculate the effective electron temperature for the noise measurement in which we bias the junction to the peak of the dynamic resistance at this temperature. At the applied bias, the voltage across the junction is $\sim 1.5\ \mu$V, resulting in a power dissipation of $V_J^2/R_s = 3.75$ pW. We can insert these parameters into Eq. (8.3) to arrive at an elevated electron temperature of ~ 78 mK. To be sure, this is a significant increase over the bath temperature, but by no means does it account for a flattening of the noise versus temperature dependence at ~ 1 K. Furthermore, this hot-electron effect speaks only to elevated temperatures in the shunt. There remains the question of how much this excess heat diffuses over the approximately 100 μm distance between shunt and junction to increase the temperature of the oxide barrier in which the TLS responsible for the $1/f$ noise most likely reside. Only in the event that the oxide barrier itself is at an el-

evated temperature can the flattening of the curve be attributed to heating. Despite the uncertainty of whether or not the hot-electron effect was a factor in the flattening of the curve, we decided to add cooling fins to the shunt resistors in future samples. The sample that provided the data for Fig. 8.7 had fins attached to the shunt resistor, but we were unable to measure it at temperatures low enough to observe any flattening.

We can further examine the question of possible heating by examining the superposed plots of the dynamic resistance and noise magnitude versus bias current, Fig. 8.4(a). First, note that at low temperatures, the voltage-noise versus bias plot peaks sharply at the place R_D peaks. This is to be expected, given the relation expressed in Eq. (8.1) (i.e., $S_V^{I_c} \propto R_D^2$) and leads to the flat nature of the plot in Fig. 8.4(b). In general, the voltage-noise plot follows the R_D plot, so we can assume that at higher temperatures the voltage-noise peak is much broader. The R_D analog of this is well illustrated by Fig. 8.6.

Now, let us assume that, for some reason, the barrier heats up significantly when we bias the junction into the nonzero-voltage state. This could be due, for example, to a high subgap conductance, in which the quasiparticles flowing through the junction dissipate more power than would typically be expected. This would effectively increase the temperature of the junction while we measure the noise and would, likewise, lead to a broader peak of voltage noise versus bias plot. That is, the voltage noise across the junction would increase at the same bias as R_D, but the barrier would also heat up at this point. This effect would broaden the peak of the voltage-noise plot, but we do not observe this to be the case. At all temperatures for which we measured the noise versus bias, we see a strong correlation between R_D and the magnitude of the voltage noise. This suggests that whatever heating may occur in the oxide barrier, it does not significantly alter the effective

temperature seen by the TLS present. This leaves us where we started. We believe the flattening observed in Fig. 8.8 is most likely due to the transition from thermal activation to quantum tunneling of the TLS.

8.2 Al Trilayer junctions

Kevin Osborn at NIST offered to fabricate Al trilayer junctions for us to measure. Because these junctions are identical to those being used by Simmonds at NIST and Martinis (first at NIST, now at UC Santa Barbara) for qubit experiments, we agreed to work with Osborn to develop a sample geometry that would provide a wide array of junction sizes, with and without cooling fins. Unlike Nb, these samples have a T_c of about 1.2 K, allowing us to explore the entire regime necessary to determine the temperature dependence of the noise while in the dilution refrigerator. For these samples, we switched to the external circuit configuration.

The measurement process when using the external feedback configuration is much the same as when using the internal feedback circuit. However, things are simpler because all the bias current applied goes through the junction, and the voltage across the junction is directly proportional to the SQUID output voltage (see Eq. (7.3)).

We measured two junction sizes for the Al junctions. The first junction measured had an effective area of 100 μm^2, though its geometry is octagonal (see Fig. 6.2(b)). At low temperatures, $T < 300$ mK, this junction exhibited exemplary $1/f$ noise behavior. Figure 8.11(a) shows the $1/f$ spectrum at $T = 14$ mK, and it does not appear to have any dominant single TLS leading to a pronounced Lorentzian. Furthermore, the magnitude of the noise corresponds well with the numbers reported in other work [41, 70]. However

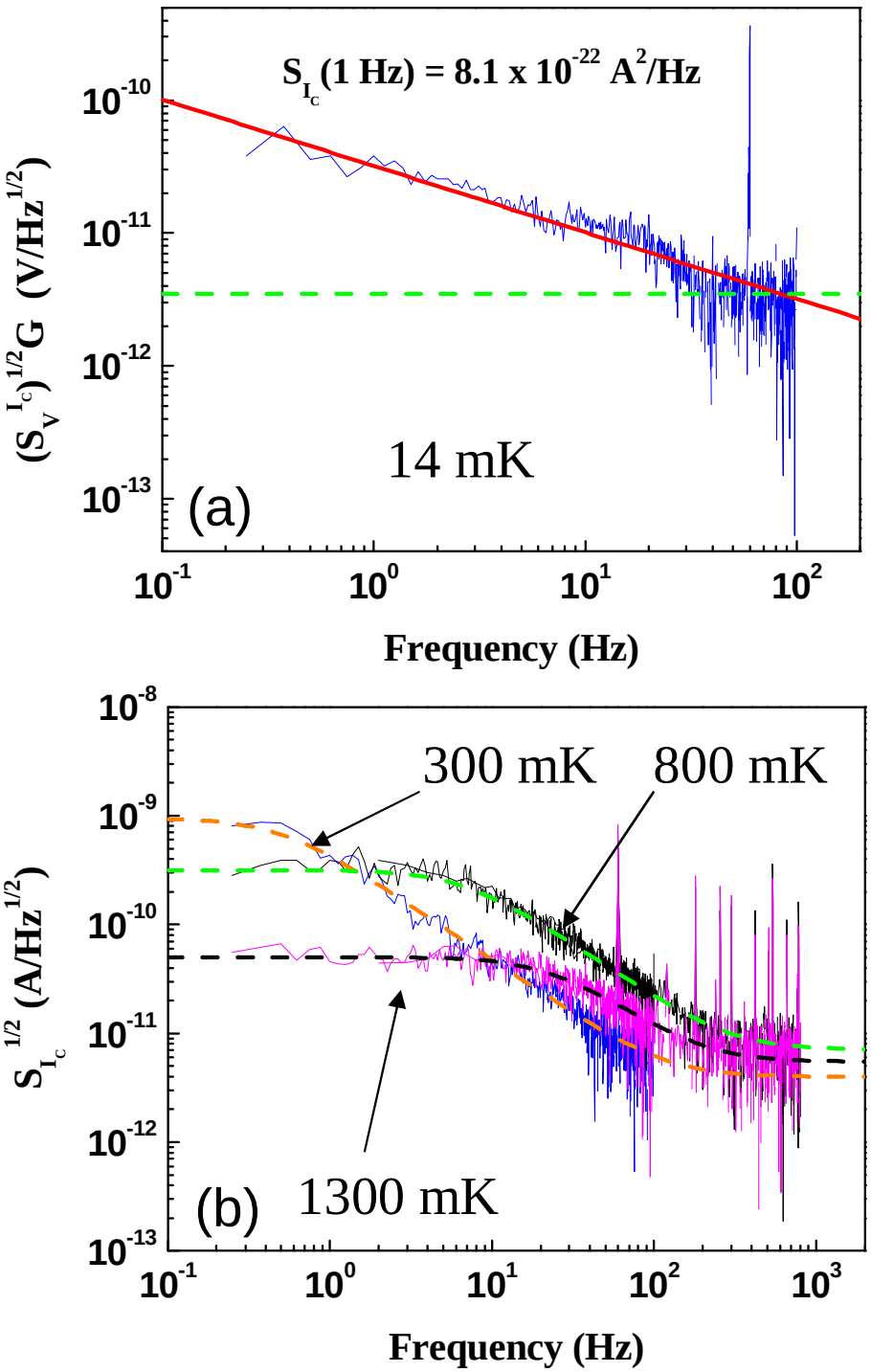

Figure 8.11 *Noise spectra from a large area Al trialayer junction. (a) Critical-current noise spectrum clearly exhibiting $1/f$ behavior (solid line) at 14 mK. After subtracting the background (dashed line) and normalizing by the dynamic resistance, we arrive at $S_{I_c} \sim 8.1 \times 10^{-22}$ A^2/Hz for the critical-current noise at 1 Hz. (b) Critical-current noise spectra clearly showing individual Lorentzians. The characteristic time, $\tau_{\rm eff}$, decreases with temperature, as expected. The magnitude of the noise caused by the fluctuator also decreases with temperature.*

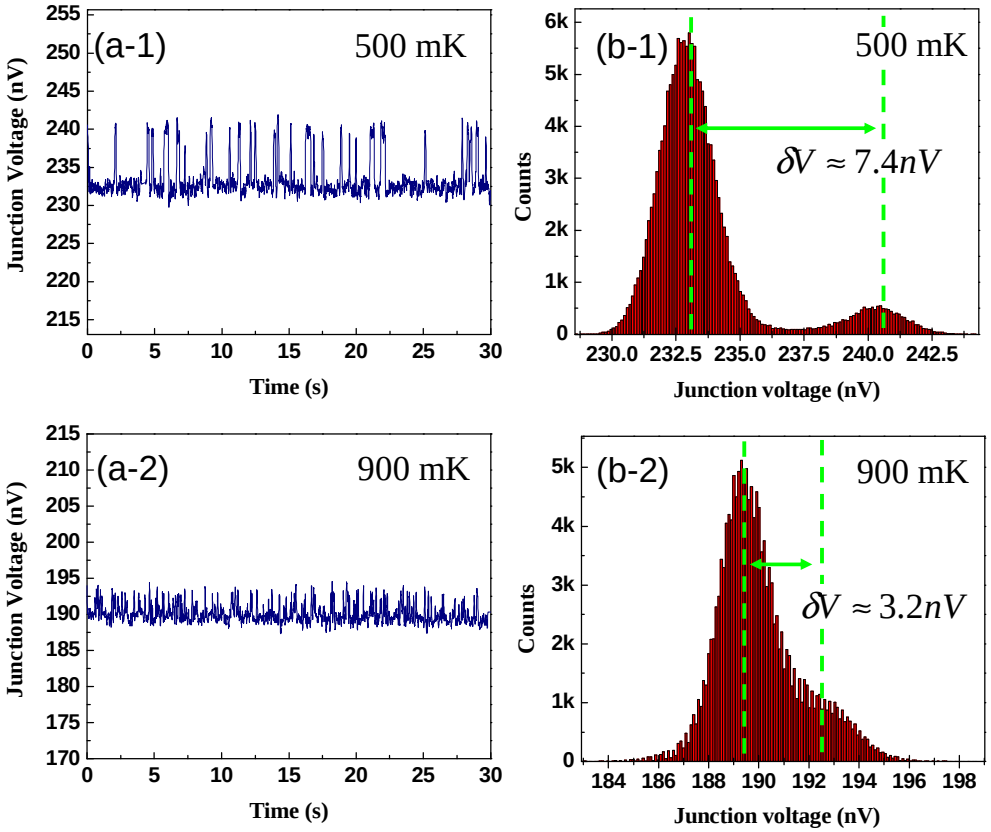

Figure 8.12 *Junction voltage time trace and histogram data. (a-1,2) Time trace of the voltage across the junction showing individual switching events, for $T = 500$ mK and 900 mK. (b-1,2) Histograms of the voltage time trace data of (a) for $T = 500$ mK and 900 mK.*

at higher temperatures, a large fluctuator becomes pronounced and begins to dominate the dynamics of this junction as illustrated in Fig. 8.11(b).

Looking back at Fig. 3.2(a), we notice that a single Lorentzian has a high-frequency rolloff proportional to $1/f^2$. This happens to be the same rolloff as a low-pass filter. Therefore, when looking at the spectra showing what appear to be a single Lorentzian, we need to determine whether this is actually an effect of filtering that we were unaware of. To determine this, we biased the junction to the peak in the dynamic resistance and measured the voltage across the junction as a function of time.

If a single large TLS is present, there should be at least two metastable

voltage states of the junction for a given bias. Figure 8.12 shows the raw voltage time trace signal and the histogram of that data for both $T = 500$ mK and $T = 900$ mK. For the TLS at the lower temperature, we estimate a voltage difference of $\delta V \approx 7.4$ nV, corresponding to a change in critical current of $\delta I_c = \delta V / R_D \approx 3.3$ nA, where $R_D = 2.23\ \Omega$ (see Fig. 7.6). Similarly, the change in critical current of the TLS at the higher temperature is $\delta I_c \approx 1.8$ nA for $R_D = 1.75\ \Omega$. This corresponds to a fractional change in the critical current of $\delta I_c / I_c \approx 3 \times 10^{-3}$ and $\delta I_c / I_c \approx 2.3 \times 10^{-3}$ for $T = 500$ mK and $T = 900$ mK respectively.

This is an enormous fractional change in critical current. While there is little doubt that what we see in this data is, in fact, a large TLS switching, we do not know what could be responsible for this much of a fractional change in critical current, which for this junction should be a factor of 100 to 1000 less. A possible cause could be the opening/closing of a dominant conduction channel in the junction. Depending on how inhomogeneous the current distribution in the junction, a mechanism such as this could yield a large correction to the critical current. Further, if the TLS responsible for this were easy to couple to via microwaves, then it would explain the odd resonances in the data from Simmonds *et al.* [50], shown in Fig. 6.2, as these junctions were made in a manner identical to those used in the qubits measured by Simmonds and Martinis. The qualitative effect of such a large single fluctuator on a qubit would be similar to what was discussed in Section 5.4 concerning the the possibility of a beat pattern arising in the osciallation/decay curve of the qubit state due to a single, large TLS.

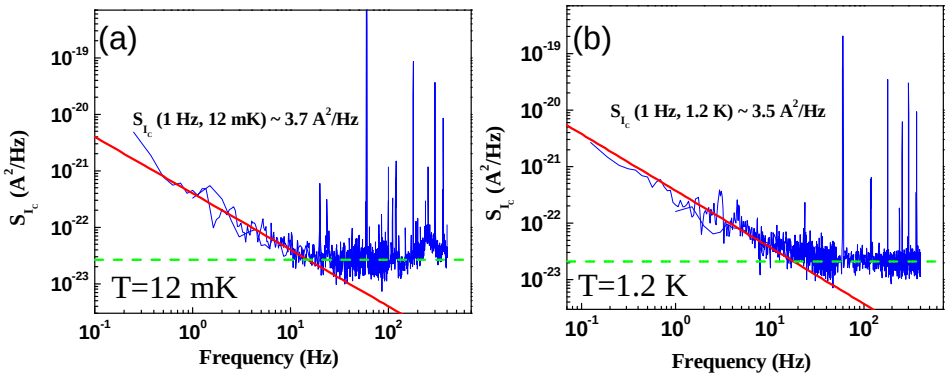

Figure 8.13 *Critical-current noise from a smaller size-scale junction with* $A = 2.5 \times 2.5\ \mu m^2$ *and* $I_c \approx 0.4\ \mu A^2$. *(a) Noise power spectrum for* $T = 12$ *mK. (b) Noise power spectrum for* $T = 1.2$ *K. In both plots the dashed line is the background signal while the solid line is the* $1/f$ *fit from which we extracted a value for the noise.*

8.2.1 Measured Temperature Dependence of Al Junctions

Because of the presence of the large two-level system shown in Fig. 8.11(b), we found it impossible to plot the $1/f$ noise magnitude as a function of temperature. Therefore, we switched to a smaller Al trilayer junction with $A = 2.5 \times 2.5\ \mu\text{m}^2$ and $I_c \approx 0.4\ \mu\text{A}$. The noise measured in this junction maintained a strong $1/f$ dependence regardless of temperature, shown in Fig. 8.13. Given this, we measured the critical-current noise magnitude as a function of temperature. Again, we ramped the temperature up from 12 mK to 1.4 K in 100 mK increments. At each temperature we measured the $I - V$ characteristic, from which we could extract the dynamic resistance dependence on bias current. Biasing the junction to the peak of R_D, we then measured the noise of the junction and subtracted the background to arrive at a value for the critical-current noise.

This dependence is plotted in Fig. 8.14 for two different Al junctions with the same parameters as those mentioned in Fig. 8.13. The most immediately

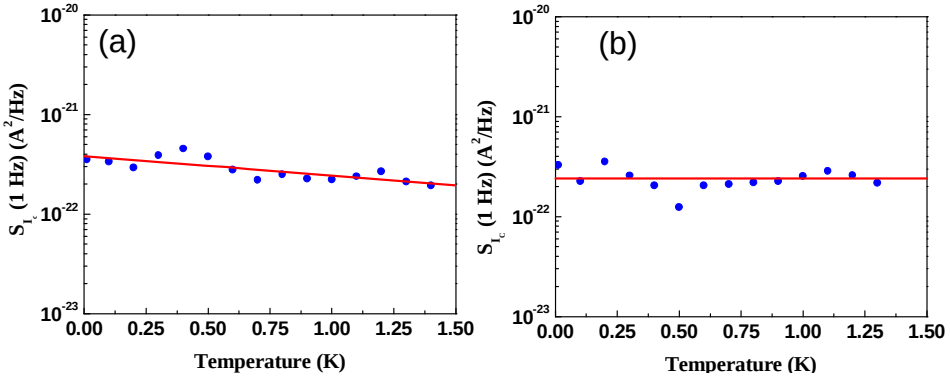

Figure 8.14 *Critical-current noise (S_{I_c}) at 1 Hz as a function of temperature for two Al trilayer junctions. (a)The solid line indicates a $T^{-0.2}$ dependence. (b)Temperature dependence appears generally flat. Both junctions' parameters are the same as those specified in Fig. 8.13.*

obvious characteristic of Fig. 8.14(a) is the decrease in critical-current noise power with temperature. Why this might be the case is unclear. However, because the second junction showed a flat dependence on temperature (Fig. 8.14(b)), we believe that in general, the Al junctions' noise power dependence on T is flat. Because Al is not superconducting at higher temperatures, we were unable to determine the higher temperature dependence as we did with the Nb junctions, shown in Fig. 8.7. However, there still remains the fact that the Nb junctions exhibited a T^2 dependence above $T \sim 1\ K$ (see Fig. 8.8), that suggests we should see some type of positive correlation between the noise magnitude and temperature.

8.2.2 Consideration of the Flat T Dependence

Why we do not see the expected temperature dependence for the Al junctions is puzzling but not without possible explanations. We mentioned in the preceding section covering the Nb junctions that Rogers and Buhrman predicted the transition temperature between thermally activated TLS and a quantum tunneling process to be in the neighborhood of 10 K. While we

found it to be an order of magnitude lower in Nb, it does not necessarily have to be lower in Al. Assuming the TLS in the oxide barrier of the Al junctions are in the quantum regime at $T < 1.5$ K does not explain the slight negative correlation between the noise and temperature, but it would definitely suggest that we should not see a T or T^2 squared dependence.

By using a large magnetic field, one could drive the junctions normal at low temperatures, allowing a continuous measurement of the noise characteristics from very low (10 mK) to very high temperatures (room temperature) without the superconducting to normal transition complicating the issue. This would be an experiment very similar to the work done by Rogers and Buhrman [47, 48] with the same goal of determining the crossover temperature from the dominance of thermal activation to quantum processes.

Another possible contributing factor is the quality of the Al itself. The nominal T_c of Al is 1.2 K. However, we clearly see junction behavior up to at least $T = 1.4$ K. This suggests impure Al, because unlike most superconductors, the T_c of Al actually rises with the impurity concentration. Given the likely sensitivity of the noise to the dirtiness of the sample, it seems reasonable to suspect the low-quality Al as a cause for the odd temperature dependence. Figure 8.15 shows an $I-V$ of an Al junction that, while heavily noise rounded, still exhibits superconducting behavior, as seen in the plot of R_D shown in the inset.

Heating of the oxide barrier could also contribute to the flat temperature dependence of the critical-current noise. We believe the dependence of the noise magnitude on current bias is the best indicator of anomalous heating behavior in the oxide. Therefore we performed measurements of the noise power as a function of bias current and compared them to the dependence of R_D on bias current, in keeping with the procedure illustrated in Fig. 8.4.

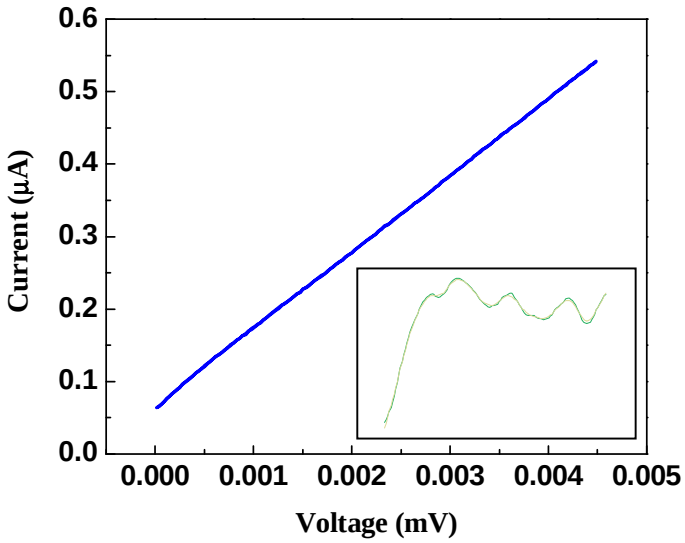

Figure 8.15 *$I-V$ of an Al trilayer junction with the same parameters as the junction in Fig. 8.13. Inset shows the R_D curve of the $I-V$, clearly showing superconducting behavior, though heavily noise rounded.*

Looking at Fig. 8.16 we see that, as we expected, the voltage noise magnitude measured by the SQUID tracks the dynamic resistance very closely. This does not conclusively rule out the possibility of heating in the barrier, but it does suggest that whatever heating there is, is insufficient to cause a transition in the TLS present in the junction from the quantum tunneling regime to one of thermal activation.

Based upon this, we feel confident in our position that in the Al junctions, the thermal activation of the noise freezes out well above the temperatures of interest for use in qubits. This would suggest a reevaluation of the chosen material for use in superconducting qubits incorporating Josephson junctions.

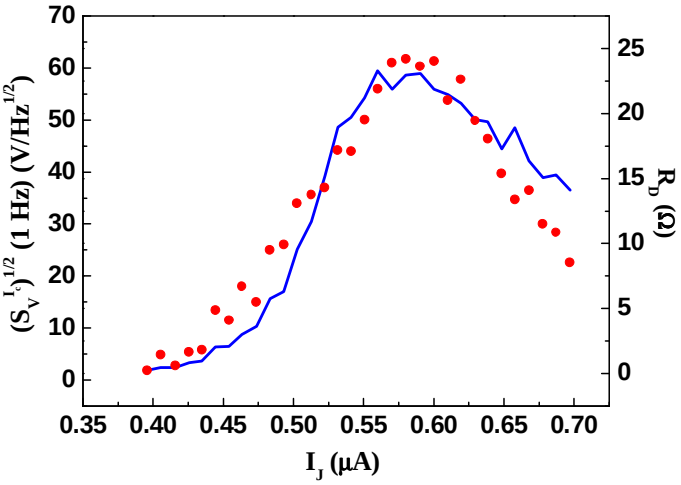

Figure 8.16 *Plot of the SQUID output voltage noise at 1 Hz and R_D versus bias current through the junction.*

9 Conclusions and Future Work

In analyzing the data we came to the conclusion that in Nb junctions any two-level systems present undergo a crossover from thermal activation to quantum tunneling at $\sim$ 1 K, as seen in Fig. 8.8. Similarly, we find that in Al trilayer junctions, the dominant processes responsible for $1/f$ noise in the junctions undergo a tunneling/activation crossover at temperatures even higher than aluminum's T_c. There are several questions relating to these conclusions that suggest further areas of research and continued analysis of the systems.

The first thing to note is that for every junction measured, the noise power was substantially higher than predicted by the empirical formula for S_{I_c}, given by Eq. (5.2), when using the parameters for the junctions we measured. Equation. (5.2) is repeated below for reference:

$$S_{I_c}(f,T) \approx \left[144\frac{(I_c/\mu\,\mathrm{A})^2}{(A/\mu\,\mathrm{m}^2)}\left(\frac{T}{4.2\mathrm{K}}\right)^2(\mathrm{pA})^2\right]\frac{1}{f}.$$

In the case of the Nb junctions, the lowest noise value recorded was $S_{I_c} \approx 1\times10^{-20}\mathrm{A}^2/\mathrm{Hz}$ at $f = 1$ Hz and $T \approx 1$ K. The value of critical-current noise predicted by Eq. (5.2) for similar junction parameters, temperature and frequency is $S_{I_c} \sim 2\times10^{-22}$ A^2/Hz, differing from the measured value by a factor of 50 in power. In order for this value to match what we measure, the temperature would have to be on the order of 10 K. If we calculate the noise expected from Eq. (5.2) for these junctions at 10 mK (the temperature

at which qubits are operated), the result differs from our measured value by a factor $\sim 6 \times 10^5$ in power.

This discrepancy between calculated and measured noise is more severe for the Al junctions. The lowest measured noised in an Al junction is $S_{I_c} \sim 2 \times 10^{-22}$ A^2/Hz. But when we calculate the noise using Eq. (5.2) with the appropriate junction parameters and temperature, the result ($S_{I_c} \approx 6.4 \times 10^{-25}$ A^2/Hz) is off by a factor of $\sim$ 300 in power. This corresponds to an effective temperature of $\sim$ 20 K. And again, if we calculate the noise for these junctions at the qubit operating temperature of 10 mK, we find that our measured noise differs by a factor of $\sim 6 \times 10^6$ in power. It is worth noting, however, that the elevated temperatures necessary for the calculation of the noise to be comparable to the measured values are both close to the threshold of 15 K, measured by Rogers and Buhrman [47, 48] (see Fig. 3.5). This suggests the possibility that our data accurately reflects the temperature dependence of the Josephson junction critical-current noise.

For further comparison, we can use our measured noise powers in the simulation of the noise as detailed in Chapter 5 to arrive at some feeling for what these elevated noise levels mean, insofar as qubits are concerned. From Martinis' analytical expression for the dephasing time of a qubit (Eq. (5.10)) we expect $\tau_\phi \propto 1/S_{I_c}^{1/2}$. Given this dependence, simulated dephasing times will be of order $\sqrt{50}$ – $\sqrt{6 \times 10^5}$ times shorter for our Nb junctions and $\sqrt{300}$ – $\sqrt{6 \times 10^6}$ times shorter for the Al junctions depending on the temperature used to calculate the expected noise power.

There also remains the question of why our critical-current noise temperature dependence differs so much from that measured by Wellstood and Clarke [70] in which they observed a T^2 dependence as low as 90 mK. We believe the fact that they measured a SQUID plays a large part in the dis-

crepancy. When dealing with a SQUID there is always the possibility of flux noise. To avoid the issue of flux noise, they biased the SQUID to a maximum of the $V - \Phi$ curve, at which the transfer function is zero. Provided trapped flux in either the junctions or the loop remains fixed and unmoving, their assumption holds. However, there is no reason to assume that in this situation the trapped vortices will remain fixed, and this will lead to $1/f$ noise caused by flux dynamics instead of critical-current fluctuations.

The issue of flux requires some thought for our situation as well. For very small scale junctions on the order of a few square microns, flux trapped in the junction is uncommon. However, the junctions we measured were all larger than this, some as large as a hundred square microns. These junctions can trap flux easily. Once again, if the flux remains stationary, there is little to worry about. One possible area of further study would be the effect of flux on the measured noise. Specifically, how does the noise depend on applied field? There is also the variation on this experiment described in Section 8.2.2 which involves using a high enough field to suppress the superconductivity in the hope of finding the tunneling/activation crossover.

In addition to the treatment of magnetic fields in this system, there is the question of the effect of individual fluctuators that could be more fully explored.

Furthermore, the issue of heating in the oxide barrier remains as one of the key questions in need of further analysis and measurements. So far we have not ruled out its presence or absence. The evidence we have suggests that it is not a significant factor, but we cannot be certain this is the case.

Despite the uncertainties of the data presented and the numerous questions that remain, we believe the data gathered supports our view that critical-current noise in Josephson junctions must flatten out at a tempera-

ture higher than the useful temperature range for qubits. This effect leads to artificially short dephasing times in qubits, and will require substantial materials research and experimentation to effectively reduce.

Appendices

A Spin Echo Technique

In NMR a spin-echo technique is used to reduce or eliminate the effect of the broadening of the ensemble spin vector with time. Initially a parallel magnetic field is used to align weakly all the spins in an NMR sample. Immediately following this alignment step, a perpendicular field is applied for a period of time sufficient to rotate the ensemble spin vector by $\pi/2$. Typically, at this point the spins are allowed to freely evolve. Due to spatial inhomogeneities in the parallel magnetic field some of the individual spin vectors will start to precess clockwise, and some will precess counterclockwise. This constitutes a "fanning-out" or broadening of the ensemble spin vector. This is allowed to proceed for a specific amount of time, τ, after which another perpendicular field pulse is applied, this time rotating the spin vectors by π. After waiting for a period of time equal to τ, the individual spins have precessed back to the original starting point, and the measurement of T_1 or T_2 can proceed as usual. This process eliminates the effect of spatial field inhomogeneities which degrade the signal during the period of time when ringing in the control electronics forces the experimenter to wait before making any measurement. Due to any spatial inhomogeneity in the ambient field, this delay would contribute to dephasing that would artificially decay the NMR signal. A process similar to this can be applied to qubit control and readout.

When applied to qubits, the goal is to reduce the effect of $1/f$ fluctuations on the qubit's coherence times. The exact procedure followed by an experimenter attempting to use a spin-echo technique will differ depending

on the type of qubit and control method in use. But mathematically the procedures are analogous and result in the same desired "re-focusing" that eliminates the effect of fluctuations occurring on a time scale longer than the period of time it takes to perform a qubit state measurement.

References

[1] V. Ambegaokar and B. I. Halperin. *Phys. Rev. Lett.*, 22:1364, 1969.

[2] J. Bardeen, L. N. Cooper, and J. R. Schrieffer. *Phys. Rev.*, 108:1175, 1957.

[3] A. O. Caldeira and A. J. Leggett. *Ann. Phys. (N.Y.)*, 149:374, 1983.

[4] I. Chiorescu, Y. Nakamura, C. J. P. M. Harmans, and J. E. Mooij. *Science*, 299:1869, 2003.

[5] K. B. Cooper, M. Steffen, R. McDermot, R. W. Simmonds, S. Oh, D. A. Hite, D. P. Pappas, and J. M. Martinis. *Phys. Rev. Lett.*, 93:180401, 2004.

[6] L. N. Cooper. *Phys. Rev.*, 104:1189, 1956.

[7] E. Dantsker, S. Tanaka, and J. Clarke. *Appl. Phys. Lett.*, 70:2037, 1997.

[8] P. Dutta, P. Dimon, and P. M. Horn. *Phys. Rev. Lett.*, 43:646, 1979.

[9] P. Dutta and P. M. Horn. *Rev. Mod. Phys.*, 53:497, 1981.

[10] V. Foglietti, W. J. Gallagher, M. B. Ketchen, A. W. Kleinsasser, R. H. Koch, S. I. Raider, and R. L. Sandstrom. *Appl. Phys. Lett.*, 49:1393, 1986.

[11] J. R. Friedman, V. Patel, W. Chen, S. K. Tolpygo, and J. E. Lukens. *Nature*, 406:43, 2000.

[12] T. Fulton and L. N. Dunkelberger. *Phys. Rev.*, 89:4760, 1974.

[13] V. L. Ginzburg and L. D. Landau. *Zh. Eksperim. i. Teor. Fiz.*, 20:1064, 1950.

[14] R. Gross, P. Chaudhari, M. Kawasaki, M. B. Ketchen, and A. Gupta. *Appl. Phys. Lett.*, 57:727, 1990.

[15] E. L. Hahn. *Phys. Rev.*, 15:580, 1950.

[16] F. N. Hooge. *Phys. Lett. A*, 29:139, 1969.

[17] F. N. Hooge and T. G. M. Kleinpenning. *Appl. Phys. Lett.*, 27:160, 1975.

[18] W. G. Jenks, I. M. Thomas, and J. P. Wikswo Jr. In *Encyclopedia of Applied Physics*, page 457. VCH Publishers, INC., 1997.

[19] B. D. Josephson. *Phys. Lett.*, 1:251, 1962.

[20] M. Kawasaki, P. Chaudhari, and A. Gupta. *Phys. Rev. Lett.*, 68:1065, 1992.

[21] M. Kawasaki, P. Chaudhari, T. Newman, and A. Gupta. *Appl. Phys. Lett.*, 58:2555, 1991.

[22] M. Kenyon, C. J. Lobb, and F. C. Wellstood. *Jour. Appl. Phys.*, 88:6536, 2000.

[23] T. G. M. Kleinpenning. *J. Phys. Chem. Solids*, 37:925, 1976.

[24] R. H. Koch, D. J. Van Harlingen, and John Clarke. *Phys. Rev. B*, 26:74, 1982.

[25] H. Kurkijärvi and V. Ambegoakar. *Phys. Rev. Lett.*, 31A:314, 1970.

[26] K. M. Lang, S. Nam, and J. Aumentado. *IEEE Trans. Appl. Supercond.*, 13:989, 2003.

[27] A. J. Leggett. In *Percolation, Localization and Superconductivity, NATO ASI Series B: Physics*. Plenum, New York, 1984.

[28] A. J. Leggett, S. Chakravarty, A. T. Dorsey, M. P. A. Fisher, A. Garg, and W. Zwerger. *Rev. Mod. Phys.*, 59:1, 1987.

[29] A. J. Leggett and A. Garg. *Phys. Rev. Lett.*, 54:857, 1985.

[30] K. K. Likharev and V. K. Semenov. *Zh. Eksp. Teor. Fiz. Pis'ma Red.*, 15:625, 1972.

[31] S. Machlup. *J. Appl. Phys.*, 24:341, 1954.

[32] J. M. Martinis, M. H. Devoret, and J. Clarke. *Phys. Rev. Lett.*, 55:1543, 1985.

[33] J. M. Martinis, M. H. Devoret, and J. Clarke. *Phys. Rev. B*, 35:4682, 1987.

[34] J. M. Martinis, S. Nam, J. Aumentado, K. M. Lang, and C. Urbina. *Phys. Rev. B*, 67:94510–1, 2003.

[35] J. M. Martinis, S. Nam, J. Aumentado, and C. Urbina. *Phys. Rev. Lett.*, 89:117901, 2002.

[36] J. M. Martinis and K. Osborn. *cond-mat*, 0402415, 2004.

[37] A. Marx, U. Fath, W. Ludwig, R. Gross, and T. Amrein. *Phys. Rev. B*, 51:6735, 1995.

[38] A. L. McWhorter. In *Semiconductor Surface Physics*. University of Pennsylvania, Philadelphia, 1957.

[39] J. E. Mooij, T. P. Orlando, L. Levitov, L. Tian, C. H. van der Wal, and S. Lloyd. *Science*, 285:1036, 1999.

[40] M. Mück, C. Heiden, and J. Clarke. *J. Appl. Phys.*, 75:4588, 1994.

[41] M. Mück, M. Korn, C. G. A. Mugford, J. B. Kycia, and John Clarke. *Appl. Phys. Lett.*, 86:012510–1, 2005.

[42] Y. Nakamura, Y. A. Pashkin, and J. S. Tsai. *Nature*, 398:786, 1999.

[43] Y. Nakamura, Y. A. Pashkin, T. Yamamoto, and J.S. Tsai. *Phys. Rev. Lett.*, 88:047901–1, 2002.

[44] T. P. Orlando, J. E. Mooij, L. Tian, C. H. van der Wal, L. S. Levitov, S. Lloyd, and J. J. Mazo. *Phys. Rev. B*, 60:15398, 1999.

[45] T. P. Orlando, L. Tian, D. S. Crankshaw, S. Lloyd, C. H. van der Wal, J. E. Mooij, and F. Wilhelm. *Physica C*, 368:294, 2002.

[46] Y. A. Pashkin, T. Yamamoto, O. Astafiev, Y. Nakamura, D. V. Averin, and J. S. Tsai. *Nature*, 421:823, 2003.

[47] C. T. Rogers and R. A. Buhrman. *Phys. Rev. Lett.*, 53:1272, 1984.

[48] C. T. Rogers and R. A. Buhrman. *Phys. Rev. Lett.*, 55:859, 1985.

[49] B. Savo, F. C. Wellstood, and John Clarke. *Appl. Phys. Lett.*, 50:1757, 1987.

[50] R. W. Simmonds, K. M. Lang, D. A. Hite, S. Nam, D. P. Pappas, and J. M. Martinis. *Phys. Rev. Lett.*, 93:77003, 2004.

[51] M. Steffen, J. M. Martinis, and I. L. Chuang. *Phys. Rev. B*, 68:224518, 2003.

[52] J. T. M. Ströken and T. G. M. Kleinpenning. *J. Appl. Phys.*, 47:4691, 1976.

[53] L. Tian, S. Lloyd, and T. P. Orlando. *Phys. Rev. B*, 65:144516, 2002.

[54] M. Tinkham. *Introduction to Superconductivity: 2nd Ed.* McGraw Hill, 1996.

[55] C. H. van der Wal, A. C. J. ter Haar, F. K. Wilhelm, R. N. Schouten, C. J. P. M. Harmans, T. P. Orlando, S. Lloyd, and J. E. Mooij. *Science*, 290:773, 2000.

[56] C. H. van der Wal, F. K. Wilhelm, C. J. P. M. Harmans, and J. E. Mooij. *Eur. Phys. J. B*, 31:111, 2003.

[57] D. J. Van Harlingen, T. L. Robertson, B. L. T. Plourde, P. A. Reichardt, T. A. Crane, and John Clarke. *Phys. Rev. B*, 70:064517–1, 2004.

[58] L. K. J. Vandamme. *Phys. Lett.*, A49:233, 1974.

[59] D. Vion, A. Aassime, A. Cottet, P. Joyez, H. Pothier, C. Urbina, D. Esteve, and M. H. Devoret. *Science*, 296:886, 2002.

[60] R. F. Voss. *J. Low Temp. Phys.*, 42:151, 1981.

[61] A. N. Vystavkin, V. N. Gubankov, L. S. Kuzmin, K. K. Likharev, V. V. Migulin, and V. K. Semenov. *Phys. Rev. Appl.*, 9:79, 1974.

[62] R. T. Wakai. PhD thesis, University of Illinois at Urbana-Champaign, 1987.

[63] R. T. Wakai and D. J. Van Harlingen. *Appl. Phys. Lett.*, 49:593, 1986.

[64] R. T. Wakai and D. J. Van Harlingen. *Phys Rev. Lett.*, 58:1687, 1987.

[65] J. R. Waldram. *Superconductivity of Metals and Cuprates*. Institute of Physics, 1996.

[66] M. B. Weissman. *Rev. Mod. Phys.*, 60:537, 1988.

[67] F. C. Wellstood. PhD thesis, University of California at Berkeley, 1988.

[68] F. C. Wellstood, C. Urbina, and J. Clarke. *Phys. Rev. B*, 49:5942, 1994.

[69] F. C. Wellstood, C. Urbina, and John Clarke. *Phys. Rev. B*, 49:5942, 1994.

[70] F. C. Wellstood, C. Urbina, and John Clarke. *Appl. Phys. Lett.*, 85:5296, 2004.

Vita

Trevis A. Crane was born on August 25, 1976 in Memphis, Tennessee and soon moved to Little Rock, Arkansas where he was raised. He attended college at the University of Arkansas at Little Rock, as a member of the Donaghey Scholars Program and graduated Summa Cum Laude with a B.S. in physics in 1998. While at the University of Arkansas, Trevis explored the field of cosmic ray detectors and found it to be uninspiring. In the fall of 1998, he began his graduate studies at the University of Illinois and started working for Professor Dale Van Harlingen in the summer of 1999. Trevis worked on two projects prior to settling upon the measurement of $1/f$ noise as a final project.

Upon completion of his doctoral degree, Trevis will continue working for Professors Van Harlingen and Budakian as a postdoctoral researcher for up to two years.